Companion Imaging Probes and Diagnostic Devices for B-Cell Lymphoma

Companion Imaging Probes and Diagnostic Devices for B-Cell Lymphoma

A dissertation presented

by

Anna Turetsky

to

The Committee on Higher Degrees in Biophysics

in partial fulfillment of the requirements

for the degree of

Doctor of Philosophy

in the subject of

Biophysics

Harvard University

Cambridge, Massachusetts

June 2014

Dissertation Advisor:
Professor Ralph Weissleder

Anna Turetsky

Companion Imaging Probes and Diagnostic Devices for B-Cell Lymphoma

Abstract

As new therapeutic targets and drugs are discovered for B-cell lymphoma and other cancers, companion diagnostics are also needed to determine target engagement, therapeutic efficacy, and patient segmentation for clinical trials. We first employed synthetic chemistry to build a platform for modifying small molecule drugs into imaging probes, using the poly(ADP-ribose) polymerase 1 (PARP1) inhibitor AZD2281 (Olaparib) as a model for technology development. Our results show that small-molecule companion imaging drugs can be used for fluorescence imaging in cells, as well as for pharmacokinetic studies and positron emission tomography (PET) imaging *in vivo*, without significantly perturbing their target binding properties or cellular uptake. To apply this approach to B-cell lymphoma drugs currently in clinical trials, we modified an irreversible inhibitor of Bruton's Tyrosine Kinase (BTK), PCI-32765 (Ibrutinib), with the fluorophore Bodipy FL (BFL), and used it for imaging in cells and in a mouse window-chamber xenograft model. The excellent co-localization of our probe (Ibrutinib-BFL) with BTK demonstrated its utility for studying additional BTK inhibitors and as a companion imaging probe. In parallel, we hypothesized that central nervous system (CNS) lymphoma diagnosis from paucicellular cerebrospinal fluid (CSF) samples could be improved with molecular profiling of putative lymphoma cells trapped in a customized microfluidic chip. Following fabrication and characterization of a polydimethylsiloxane (PDMS) diagnostic device containing an array of affinity-free single-cell capture sites, we were able to efficiently recover

>90% of lymphocytes, perform immunostaining on chip, and apply an image-processing algorithm to group cells based on their molecular marker expression, such as kappa/lambda light chain restriction. Additionally, in combination with Ibrutinib-BFL or other imaging drugs, we demonstrated the potential for on-chip drug imaging for use in conjunction with drug development. Finally, we applied bioorthogonal conjugation chemistries on cellulose paper for potential applications in lowering the cost of drug screening. We anticipate that these approaches will enable direct, molecular information for personalized treatment decisions in B-cell lymphomas, as well as provide a roadmap for the development of companion diagnostic probes and devices for additional indications.

Table of Contents

Acknowledgements

Allow me to preface by stating that it will be impossible to provide all the acknowledgement deserved by the great people who have been part of my previous five years. When I was applying to graduate school and traveling to various recruiting weekends, there were rumors at other universities that Harvard was more competitive than nurturing. Fortunately, they were far from correct. Not only do I believe that the Harvard Biophysics program is the *best* biological science graduate program in the country (this is why they let me talk to the recruits), but I have also been profoundly inspired by my lab, student activities, and friendships formed with other Harvard graduate students.

So, I would like to thank…

- My advisor, Ralph Weissleder, for the opportunity to work with vast resources, and for leading by example by showing me how to choose transformative research projects, efficiently run an organization, and hire and manage the best people. In what other lab would students and postdocs be so fortunate as to be worried if their advisor took more than an hour to reply to an e-mail? In what other lab would it be reasonable to anticipate receiving manuscript or figure edits overnight? I am still learning how to consider clinical needs and impact before being excited by new technologies, and Ralph has helped outline how to do this with three simple questions: 1) Who cares? 2) Why is it important? 3) Is it novel? I will certainly continue to think of these lessons and more as I move onward.

- The truly excellent group of scientists who I am proud to call my coworkers and friends, and who have shown me how interdisciplinary research should be done.
    - The chemists, especially Thomas Reiner and Eunha Kim, who taught me how to be a better scientist and harder worker, in addition to synthesizing compounds and discussing ideas for our collaborative projects. Also: Jonathan Carlson for knowing seemingly everything and being a great teacher, Sarit Agasti for his infinite creatively, Bjorn Askevold and Melissa Sprachman for always being there (literally, in lab, all the time), Neal Devaraj for paving the way for lab dinners, and Ghyslain Budin and Ned Keliher for always being willing to share their wealth of chemistry knowledge.
    - The biologists, especially Sarah Earley Coffey, for being a courteous baymate for so long and answering all my questions (from research-related to filling out tax forms). Also: Katy Yang for always being willing to share, Miles Miller for showing me how to organize projects and people, Jimmy Giedt for his MatLab skills and midwestern zen, and Ashley Laughley for setting an example in simultaneous sharpness and poise.
    - The engineers, especially Kyungheon Lee and Jun Song for being wonderful collaborators, David Issadore for perfectly balancing ambition and generosity, Partha Ghosh for being a lovely baymate if for a relatively short time, and of course Hakho Lee for organizing journal club meetings and leading truly innovative projects. And, along with Eunha, Hyun, Kyungheon and Hakho, Yong-Il Park, Changwook Min, Hyungsoon

Im, Sangmoo Jeong, and Jaehoon Chung for the introduction to all things Korean, from materials science, to barbecued meats, to copious amounts of soju at lab gatherings.
- Additional researchers in the lab who are more difficult to categorize, especially Adeeti Ullal, Vanessa Peterson, and Huilin Shao for demonstrating how to be successful graduate students in the lab, and Susan Clardy, who quickly became a sounding board for issues inside and outside of the lab, and a good friend. Also: Hyun Jung Chung for her quick advice at the lab, impossible grace, and for organizing lab girls' nights, Greg Thurber for teaching us to think about pharmacokinetics, Cesar Castro for his deep insight into clinical sample acquisition and IRBs, Kevin King and Aaron Aguirre for introducing us to the cardiovascular diagnostics space, Claudio Vinegoni and Matt Dubach for their cool anisotropy-based imaging, and Monty Liong for letting me crash his trip to that AACR conference in Miami.
- The technicians, especially Joshua Dunham who was so helpful with both imaging and computers (not to mention office pranks) until he was stolen away by Vertex, and Misha Pivovarov for solving all of our computing issues, often before they happen. Also: Yoshiko Iwamoto for being a histology wizard and reliable late lunch companion, Rainer Kohler and Alex Zaltsman for their imaging expertise, and Rostic Gorbatov and Matt Sebas for their good humor while cutting into small animals for our benefit.
- Other members of CSB, including Mikael Pittet, and his lab members Virna Cortez-Retamozo, Andita Newton, Ferdinando Pucci, Chris Garris, Camilla Engblom, Christina Pfirschke, and Martin Etzrodt for their immunology and flow cytometry guidance, and Lorette Noiret, Carlos Tassa, Olivier Kister, Adam Hendricks, and Sofia Santos for sharing in advice and happy hours.

- The CSB staff (dare I admit, its intrastructure?), without whom the lab could not function: Dianne Moschella, Serena Sullivan, Tina Balducci, Missy Greene, Sharon McSorley, Matt Mues, and Peter Waterman, for putting up with us scientists with a sense of humor; making sure we have paychecks, research supplies, and donuts; and taking the weekends off so that I can drink coffee at my lab desk.

- My lab rotation advisors prior to Ralph: William Shih, for letting me play with DNA origami designs and forcing me, albeit briefly, to learn how to code in Python, and Jagesh Shah for more wisdom, moral support, and comic relief than I can convey here, including such rules as the "Shower Test" - you know you're working on the right problem if you think about it in the shower, and "Pi" - everything takes 3.14x longer than you expect. And not only that, but I owe Jagesh my deepest gratitude for his help in writing my successful fellowship application based on my project in his lab.

- Those who make the biophysics program possible and, again, the *best*: Michele Jakoulov, who is amazing beyond words, overqualified for her job (yet stays with us), and somehow does it all without a cell phone, and Jim Hogle, who had the wisdom to run a program without (m)any rules. Also, my fellow students in the program, especially my close friend Brenna Krieger whose lab sadly took her away to California, as well as Alec Chapman, Travis Zack, Alex

Nichols, Julia Liu, Brad Nelms, Risa Kawai, Alison Hill, Dan Chonde, Julia Rogers, Hanlin Tang, and Genya Frenkel for their camaraderie. And finally the affiliated professors who are cool enough to come to our program events, including my fantastic PQE committee member Conor Evans.

- My exam committee for their guidance on my thesis: Jagesh Shah (mentioned above); Brian Bacskai, who is doing great work and whose lab I might have joined had I not been scared of the commute to the Navy Yard, and Ralph Mazitschek for so much chemistry advising over the years.

- The student groups, professors, and mentors who have inspired me to aim to become a leader in the biotech industry: Harvard Graduate Women in Science and Engineering (HGWISE), Harvard GSAS Business Club (HGBC), and Harvard Biotech Club; Andrey Zarur and Jonanthan Fleming who introduced me to venture capital and business development in MIT 15.363; Reid Leonard, Chris Earl, Christine Brennan, Vikas Goyal, Geoff Meyerson, Young Kwon, Ellen Baron, Lauren Celano, and Anupendra Sharma, for making me feel welcome, and introducing me to great people and opportunities.

- My friends and roommates (outside of the lab and program) who made Boston feel like home even during the cold winters: Steve Hershman, Tami Lieberman, Lauren Hartle, Laura Strittmatter, Laura Stone, Boris Zinshteyn, and Phil Enock. My friends living outside Boston, who I could always depend on when I wanted to get away: Rebecca Goodsell, Julia Xu, Kavita Vinekar, Andrea Finch, Tawei Lin, David Freeland, and Anderson Lee. Also: Jason Holt for the occasional complimentary Uber ride and Jared Sadoian for his hospitality at Craigie on Main.

- My parents, for always having high expectations of what I can achieve and supporting me through visits, phone calls (sometimes too many!), and even shampoo deliveries. But most of all, from a young age, they encouraged me to explore the arts alongside math and science, enabling my creativity and independent thinking. Then, they managed to influence me to pursue biomedical research — so why not begin with a PhD?

Financial support was provided by the National Science Foundation's Graduate Research Fellowship Program (NSF GRFP) and the Harvard Biophysics Program's National Institutes of Health (NIH) Molecular Biophysics predoctoral training grant.

List of Figures and Tables

Chapter 1.

Introduction

1.1. Using Diagnostics to Inform Drug Development

How can drug development be improved to notice failures early or to turn those failures into cures?

Pharmaceutical drug development in the United States involves the progression of pre-clinical drug candidates (which have gone through cell and animal testing) through a series of costly human clinical trials: Phase I (safety, dosing, pharmacokinetics), Phase II (efficacy, dosing), and Phase III (safety and efficacy in a larger population; comparison to previously used treatments). Once past phase III, the Food and Drug Administration (FDA) will decide whether to approve a drug to be marketed. For oncology drugs, the success rates at each stage are 55%, 28%, and 45%, respectively, meaning that out of all the drug candidates that enter clinical development, only about 7% will be approved[1].

Reasons for the failures vary. Sometimes there are safety issues in Phase I, for example unanticipated side effects from the drug or its metabolites interacting with the body in a way different from the intended mechanism-of-action. Others fail in Phase II due to the inability of the drug to engage with the target of interest (due to poor delivery or low potency), too low of a therapeutic index, or resistance mechanisms that can quickly reverse the efficacy of a drug. Particularly in Phase III trials, disease heterogeneity can greatly influence the statistical efficacy of a drug in a diverse population of patients, and conventional cancer diagnostics that rely on changes in

cellular morphology (cytopathology, histopathology), tissue density (X-ray, CT, MRI), or tumor metabolism (^{18}FDG positron emission tomography (PET)) do not give enough molecular information to separate patients into subgroups.

Recently, the motivation and ability to differentiate cancers by molecular pathway rather than tissue-of-origin has led to the advent of targeted therapeutics, and the search for biomarkers and molecular response criteria during drug discovery. This in turn has allowed us to improve preclinical studies, diagnostics, and monitoring during clinical trials using new technologies for a) directly establishing target engagement and drug effects *in vivo* and *in vitro*, and b) better diagnostics for each individual patient to predict drug efficacy and to monitor disease progression during treatment. Moreover, key challenges are to accomplish this in the least invasive manner possible, relatively cheaply, and at the point-of-care. Once these approaches are used to identify problems during drug development, solutions can be investigated, including screens for more specific drugs, nanoparticle-mediated drug delivery, combination drugs to combat resistance, and personalized medicine based on molecular-level disease profiling.

1.2. Imaging Drug Pharmacokinetics, Pharmacodynamics, and Target Occupancy

To provide insights into both target and off-target engagement by therapeutics, we can use reporter ligands that directly bind to the therapeutic target[2]. These can be small molecule or antibody-based drugs, chemically modified into radioactive, fluorescent, or affinity probes, that are henceforth used to directly study biodistribution, pharmacokinetics, cellular and sub-cellular targeting specificity (i.e. with which other cell

types or proteins does the drug interact), cell-to-cell heterogeneity, drug occupancy, and pharmacodynamics[3]. Two approaches to making such probes are direct conjugation to a reporter or creating probes with a "clickable" chemical moiety.

In our group, bioorthogonal click chemistry using trans-cyclooctene (TCO) and tetrazine (Tz) groups was previously explored as a way to label antibodies and nanoparticles with fluorophores or ^{18}F for targeted PET[4-6]. The application of TCO/Tz click chemistry had several important advantages: a) two-step delivery of the ligand and reporter could improve the kinetics with which the labeled component reaches the target (e.g. the reporter small-molecules have shorter circulation half-life than nanoparticles or antibodies), b) the very fast click reaction allows for a modular ^{18}F-TCO labeling approach, whereas direct synthetic incorporation of radioactive fluorine may be too slow when considering ^{18}F radiodecay, and c) the same drug conjugate can be easily adapted for either radio or fluorescent labeling. The radiolabeled ligands were used to image drug biodistribution and target occupancy by unlabeled drug using PET whole-animal imaging, while the fluorescently labeled probes were used in high-resolution intravital fluorescence imaging in a mouse tumor window chamber model[7].

Later, we applied this strategy to turning small-molecules into imaging probes. The work in Chapter 2 describes starting with a drug candidate, AZD2281 (Olaparib, a PARP1 inhibitor), chemically modifying it for either fluorescence imaging or PET using click chemistry, and using *in vitro* and cell studies to validate the probe's affinity to the drug target. It was then used as an *in vivo* tool to learn about the original drug, using both fluorescence imaging and PET imaging in mice. Interestingly, Olaparib development was

stopped after failed Phase II clinical trials in 2011, but was recently resurrected and is again in clinical trials for more precise indications – a misstep that perhaps could have been avoided by using imaging to properly characterize target protein expression levels and drug pharmacodynamics.

1.3. Molecular *In Vitro* Diagnostics

Conventional cancer diagnosis from biopsies, cytopathology or histopathology, is based on changes in cellular morphology using non-specific H&E stain to visualize nuclei and cellular substructures. More recently, partial or whole cancer genome sequencing has been added to look for specific tumor mutations or predispositions. While the former approach lacks molecular specificity, the latter only points to an upstream identifier of malignancy or cancer target. For accurate, downstream criteria, it would be helpful to perform measurements at the biochemical, protein level, allowing for direct monitoring of drug binding and efficacy. Although it has been possible to gain some information using flow cytometry systems, improved approaches combine the ability to simultaneously interrogate at the morphological, protein, and genomic levels.

One such integrated method is to use microfluidic chips to capture and profile cancer cell populations. A notable innovation was the CTC Chip, used to capture rare (5-1000 per mL) circulating tumor cells from blood[8]. In that work, anti-EpCAM antibodies were used to capture only those cells expressing that protein on their surface, allowing for the counting of EpCAM-positive circulating cells in patients, and their correlation to treatment response and course of disease[8]. To remove capture bias, our group has focused

on the design of chips with single-cell passive capture sites, followed by on-chip immunostaining and/or removal of the cells for further analysis[9-11].

An additional benefit of using microfluidic chips is that analysis can be done on diverse tissue samples without extensive pre-processing. Searching for tumor cells in blood or discarded tissues such as ascites fluid[10] add to the potential to monitor cancer cells during drug treatments without additional, invasive biopsies. We can then use specific, molecular criteria to track the patient subpopulations in whom a particular treatment is effective, as well as development of drug resistance to inform treatment regime changes.

1.4. B-Cell Lymphoma

Lymphoma and leukemia are proliferative diseases of mature and immature lymphocytes, respectively, but in reality can be split up into many different entities on the cellular and molecular levels. Here, in Chapter 3 and Chapter 4, the work described focuses on taking the principles of imaging drugs and *in vitro* diagnostics and applying them broadly to these B-cell malignancies.

Within the last 15 years, there has been a revolution in the molecular understanding of B-cell cancers at the same time as new drugs – both small molecules and biologics – have been introduced to treat them[12-14]. One surprising finding that led to a paradigm shift was the stratification of Diffuse Large B-Cell Lymphoma (DLBCL), the most common type of lymphoma, into two subtypes, ABC and GCB, segmented based on the RNA expression using microarray data[12,15,16]. This clear heterogeneity beneath a veil of

cytological and morphological similarity revealed the need for approaches based on molecular expression markers for personalized characterization and treatment of disease[13].

One particularly promising drug class in development, covalent inhibitors of Bruton's Tyrosine Kinase (BTK), is thought to be more effective in the ABC subtype of DLBCL[17,18], as well as in chronic lymphocytic leukemia, acute myeloid leukemia, and in mantle cell lymphoma[19-22]. One such drug, the irreversible BTK inhibitor PCI-32765 (Ibrutinib, now marketed as Imbruvica), was already effectively modified with Bodipy FL dye into a drug occupancy assay probe that was used during preclinical and clinical development[19,23]. The method took advantage of the irreversible binding of Ibrutinib to visualize it bound to its target on a denaturing polyacrylamide gel using fluorescent gel scanning, and they determined that occupancy decreases only about 20% over a 24-hour period[19]. Chapter 3 describes work in which we created a similar probe and tested it for utility as an imaging probe, with potential applications in both cancer cell biology and as a targeted PET agent for lymphoma.

We then thought it would be interesting to focus in on a medical need where diagnosis is quite challenging and the disease is aggressive: CNS lymphoma, which can be a primary lymphoma tumor site (with increased risk in immunodeficient patients), or can occur due to a metastasis across the blood-brain barrier. The success of diagnosis at the site of disease – in cerebrospinal fluid (CSF) samples – is limited due to sample paucicellularity, as well as the poor specificity/sensitivity of the conventional approach, cytopathology; sophisticated imaging modalities such as CT/MRI do not perform any

better. For this clinical application, we custom-built a microfluidic chip platform with molecular imaging capability, and demonstrated our ability to process and analyze these types of samples. This work is described in Chapter 4.

1.5. Lowering the Cost of Diagnostics

Many of the tools currently being developed for molecular diagnostics rely on costly equipment, for example fluorescence microscopes or sequencing machines, or at the very least a trip to the hospital. In order to minimize the costs for patients of monitoring drug targets and their occupancy and monitoring disease progression, drastically different approaches may be needed, especially for resource-limited settings.

To bring diagnostics truly to the "point-of-care" - the home or the field - one approach that some researchers and a non-profit (Diagnostics for All) are exploring has been coined "paper-based microfluidics"[24]. For example, a paper-based test was developed and field-tested to address the need to monitor occurrences of drug-related hepatotoxicty, common when combining drugs for multiple indications, such as HIV and tuberculosis[25,26]. In these tests, small-volume blood samples from finger pricks are wicked directly onto a paper device, about the size of a postage stamp, containing various detection points for multiplexed readouts. To provide additional functionality to these types of devices for their use in drug testing, I sought to combine paper-based detection with TCO-Tz click chemistry by synthesizing "clickable" paper. Chapter 5 provides further background on paper microfluidics, as well as the results from this work and some potential applications.

(blank page)

Chapter 2.

The PARP1 Inhibitor Olaparib as a Model System for Small-Molecule Drugs as Imaging Agents

This work was previously published as:

Thomas Reiner, Sarah Earley, Anna Turetsky, and Ralph Weissleder. Bioorthogonal Small-Molecule Ligands for PARP1 Imaging in Living Cells. *ChemBioChem*, 11: 2374–2377 (2010). doi: 10.1002/cbic.201000477

Author Contributions

T.R. and R.W. designed the research, and T.R. and A.T. performed experiments. T.R. performed chemical synthesis and characterization. S.E. prepared transgenic cell lines and provided guidance on immunofluorescence staining. T.R. and A.T. analyzed data and prepared figures. T.R. and R.W. wrote the manuscript. All authors reviewed and edited the manuscript.

Due to recent successes in designing small molecule PARP1 inhibitors, we have synthesized imaging agents for PARP1 based on 1(2H)-phthalazinones. The intracellular distribution of AZD2281-TCO, a transcyclooctene-modified derivative, was visualized by selective reaction with a reactive fluorescent tetrazine. We show that AZD2281-TCO has an IC_{50} of 11.8 nm, assembles with Tz-fluorophores in the nucleus, and colocalizes with PARP1 in live cells.

2.1. Introduction

Poly(ADP-ribose) polymerase 1 (PARP1) is an important cellular protein that senses DNA damage and initiates the base excision repair pathway[27]. DNA damage (strand breaks) occurs during each cell cycle and must be repaired for a cell to survive. In the absence of functional BRCA (another class of complementary DNA repair enzymes), cells depend primarily on the PARP repair mechanism. Thus, PARP inhibitors (PARPi) are emerging as a useful option for cancer therapy, either as single agents or in combination with other DNA-damaging molecules[28-30]. In view of their encouraging results in breast cancer trials, there is now considerable interest in expanding PARPi to other primary tumors. However, despite the increasing body of literature on PARP, many questions remain unanswered, not only regarding its basic biology, regulation, heterogeneity, and role in individual tumor types, but also regarding the efficacy of new PARPi, optimum dosing, timing and combination of treatment, among other factors[28,31]. For example, PARP1 has a number of additional roles, including the restarting of stalled replication forks, the inhibition of nonhomologous end-joining repair, the regulation of transcription, the initiation of a unique cell death pathway, and the modulation of cellular bioenergetics[28]. Thus, to gain more insight into these additional roles and to better understand PARP1 regulation *in vivo*, it would be an enormous advantage to be able to image PARP1 in live cells and ultimately in whole living organisms. Whilst green fluorescent protein (GFP) fusion proteins remain valuable tools for imaging at the cellular level, labeled affinity ligands, which are cell permeable, will ultimately be required for whole-body preclinical and clinical imaging.

To date, a variety of small-molecule PARPi have been developed. These include the lead group 1(2H)-phthalazinones, such as AZD2281 (**2.1**) and its derivatives[28,31,32]. It has been shown that the 4-NH-piperazine of AZD2281 tolerates a diverse range of capping groups without significantly decreasing PARP1 binding affinity[32]. We therefore used this anchor point to attach bioorthogonally reactive groups and/or different fluorophores to the phthalazinone. We hypothesized that these modifications would still result in low nanomolar affinity ligands and that conjugates would retain their cell permeability, particularly with the use of bioorthogonal linkers.

2.2. Results

As a precursor for the synthesized AZD2281 inhibitors (Figure 2.1), 4-[[4-Fluoro-3-(piperazine-1-carbonyl)phenyl]methyl]-2H-phthalazin-1-one (**2.2**) was obtained according to known literature procedures[32]. For the synthesis of the bioorthogonally reactive derivatives AZD2281-NOB (**2.6**) and AZD2281-TCO (**2.7**), compound **2.2** was first reacted with glutaric acid anhydride to produce the glutaric acid-modified 4-(5-oxopentanamide)piperazine (**2.3**) in 72% yield. Subsequently, an ethylene diamine spacer was attached to precursor **2.3**, yielding the amine-functionalized AZD2281 derivative **2.4**. Norbornene-functionalized AZD2281-NOB (**2.6**) was obtained by amide-bond formation with 5-norbornene-2-carboxylic acid in the presence of polymer-supported dicyclohexylcarbodiimide (DCC) beads. In the case of AZD2281-trans-cyclooctene (AZD2281-TCO; **2.7**), precursor **2.3** was reacted with (E)-cyclooct-4-enyl 2,5-dioxopyrrolidin-1-yl carbonate (**2.5**) in the presence of triethylamine[5]. The identities of

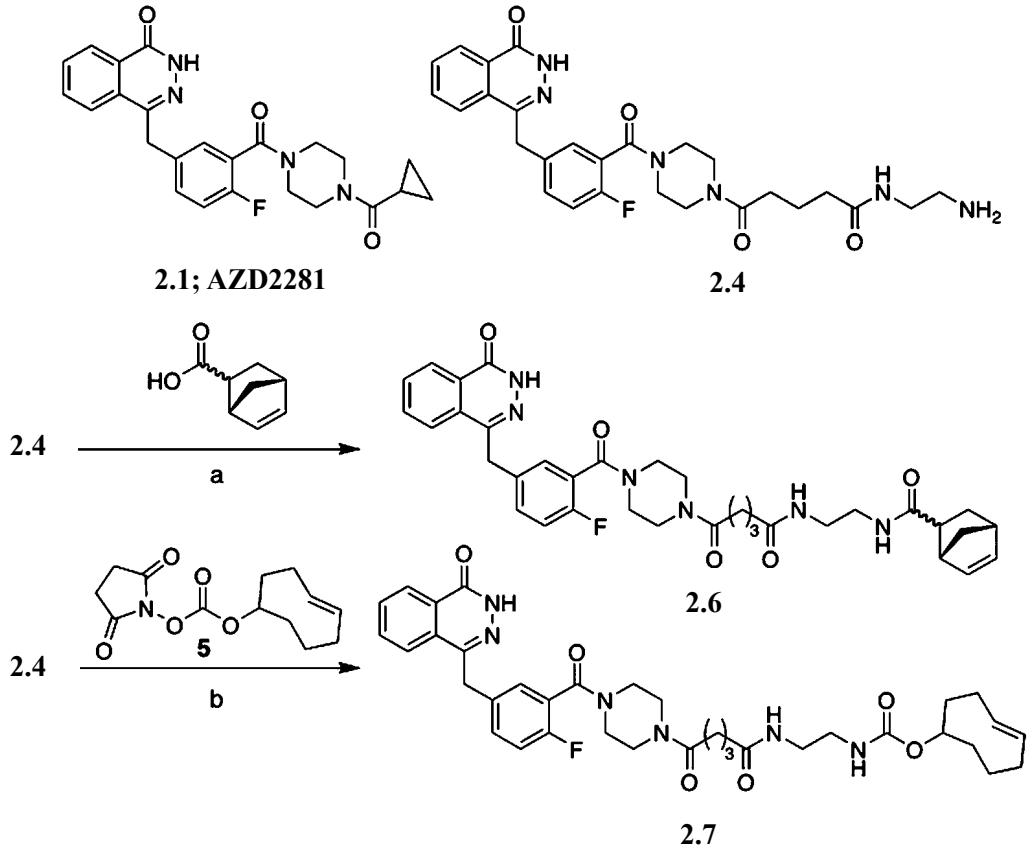

Figure 2.1. Synthesis of bifunctional 1(2H)-phthalazinone-based targeted probes. Reagents and conditions: a) Polystyrene-bound DCC, Et_3N, CH_2Cl_2, RT, overnight; b) Et_3N, CH_2Cl_2, RT, overnight; for detailed synthetic descriptions, see section 2.3.

all 1(2H)-phthalazinone-based bioorthogonal probes and their precursors were confirmed using HPLC-MS, high-resolution MS and NMR spectroscopy.

The fast reaction kinetics of trans-cyclooctenes (TCO) and tetrazines (Tz) make AZD2281-TCO (**2.7**) a potential candidate for live-cell imaging using fluorophore-tetrazine derivatives[5,33,34]. Cycloaddition of both AZD2281-TCO (**2.7**) and Texas Red-Tz (**2.8**) was detected by mixing the two compounds (0.3 mM), agitating for several minutes,

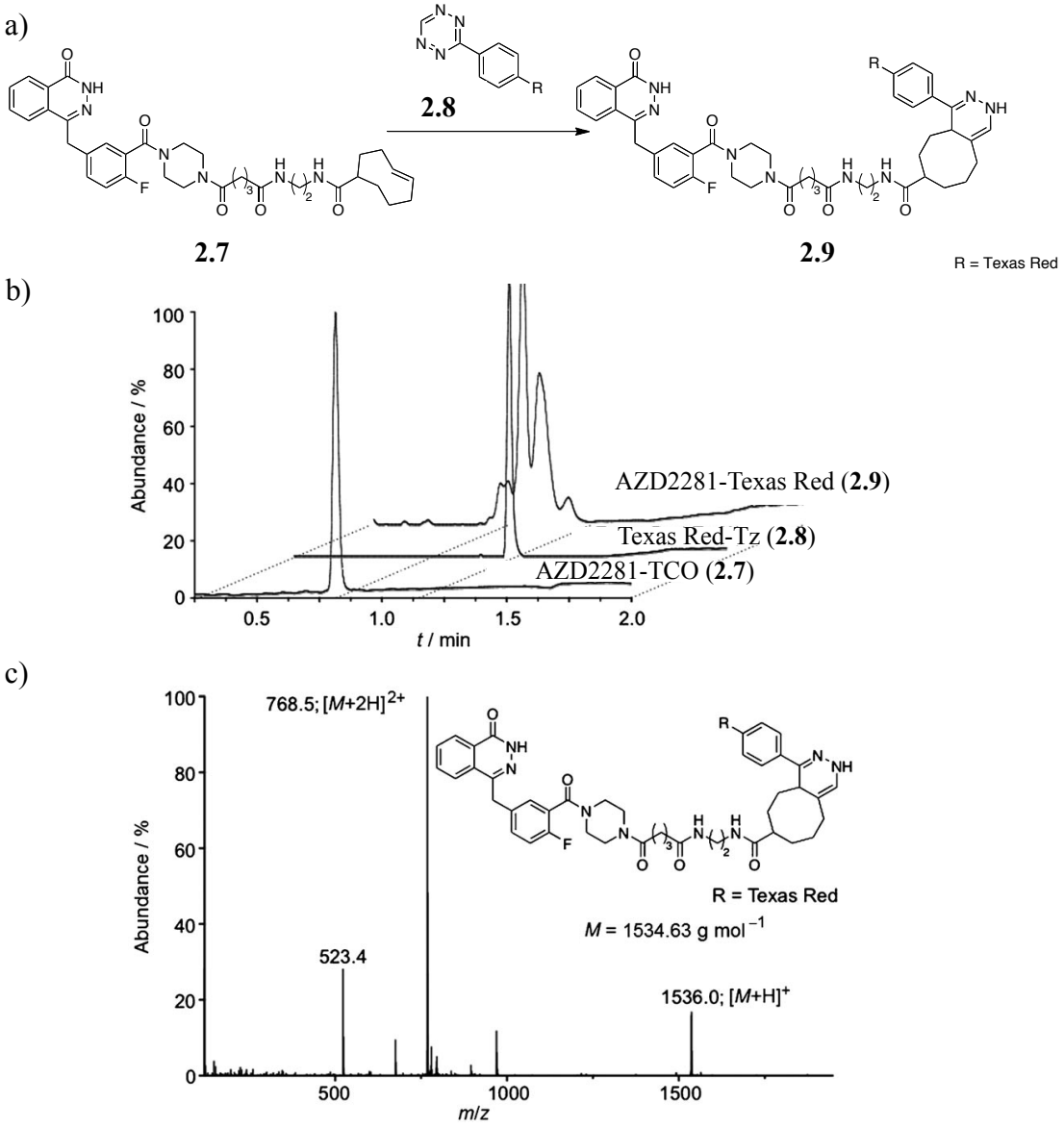

Figure 2.2. Synthesis and characterization of AZD2281-Texas Red. a) Synthesis of AZD2281-Texas Red (**2.9**) from AZD2281-TCO (**2.7**) and Texas Red-tetrazine (**2.8**) using tetrazine/trans-cyclooctene cycloadditions. b) An HPLC trace of AZD2281-TCO (**2.7**); Texas Red-tetrazine (**2.8**; one isolated stereoisomer shown); and AZD2281-Texas Red (**2.9**; crude reaction mixture). c) LC-MS spectrum of AZD2281-Texas Red (**2.9**; LC-MS of major product peak shown).

and analyzing the products by HPLC-MS (Figure 2.2a; Figure 2.2b shows the HPLC trace for the AZD2281-Texas Red (**2.9**) crude reaction mixture). LC-MS spectra confirmed the quantitative conversion of Texas Red-Tz (**2.8**). Multiple peaks were identified with a molecular mass corresponding to AZD2281-Texas Red (**2.9**; Figure 2.2c, m/z 1536.0 $[M+H]^+$). These were the result of different isomers formed in the tetrazine trans-cyclooctene cycloaddition[5,34,35]. The fast and selective conversion of AZD2281-TCO (**2.7**) to AZD2281-Texas Red (**2.9**) in the presence of Texas Red-Tz (**2.8**) indicates that these small molecules also have potential applicability to *in vivo* experiments. The inhibitory potentials of AZD2281 derivatives **2.6** and **2.7**, and of pre-reacted AZD2281-Texas Red (**2.9**), were tested using a PARP1 activity assay (see section 2.3 for details). Analysis of the AZD2281 derivatives **2.6** and **2.7** resulted in IC_{50} values of 10.1 ± 1.3 nM and 11.8 ± 1.4 nM, respectively (Figure 2.3). Thus, modification and conjugation of linkers and fluorophores to the 4-NH-piperazine group of AZD2281 precursor **2.2** appear to be tolerated by the enzyme, and allow the design of bifunctional derivatives. The IC_{50} value of pre-reacted AZD2281-Texas Red (**2.9**; 15.4 ± 1.2 nM) demonstrates that the trans-cyclooctene/tetrazine cycloaddition only minimally reduces binding of the 1(2H)-phthalazinone to PARP1, which confirms its possible application as an imaging probe (Figure 2.3).

Due to their fast reaction kinetics compared to AZD2281-NOB (**2.6**), the trans-cyclooctene conjugated AZD2281 (AZD2281-TCO; **2.7**) and Texas Red-Tz (**2.8**) were tested under *in vivo* conditions in live cells[5]. MDA-MB-436 cells, a well characterized BRCA1-mutant breast cancer cell line, were incubated with Texas Red-Tz (**2.8**; 1 μM in

Table 1. IC_{50} values for the bifunctional 1(2H)-phthalazinone-based targeted probes and for AZD2281-Texas Red.

Compound	Name	#	MW [g mol^{-1}]	IC_{50} [nM]	Reactive with
Reactive inhibitor	AZD2281-NOB	**2.6**	642.7	10.1 ± 1.3	Tz-fluorochromes
	AZD2281-TCO	**2.7**	674.8	11.8 ± 1.4	Tz-fluorochromes
Fluorescent inhibitor	AZD2281-Texas Red	**2.9**	1535.6	15.4 ± 1.2	NA

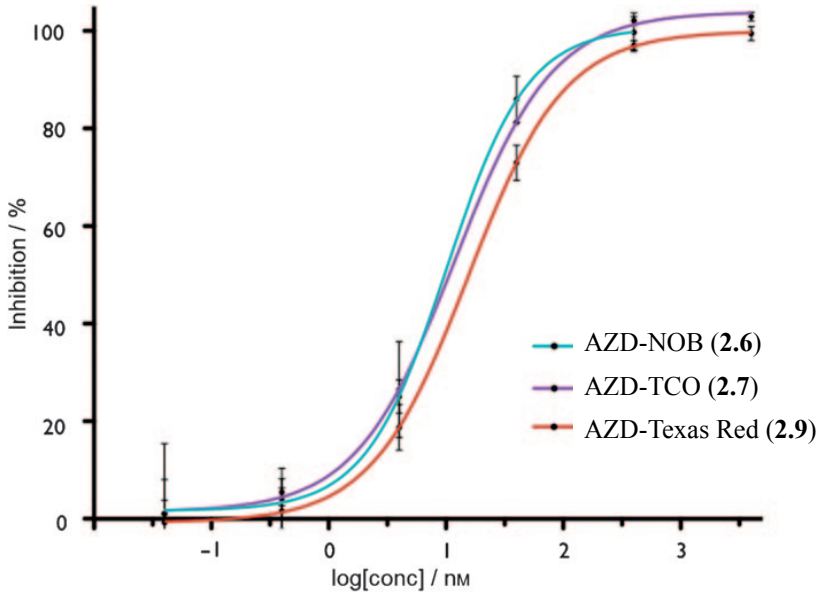

Figure 2.3. Inhibition of PARP1 by AZD2281 derivatives. Top, table of IC_{50} values of PARP1 inhibition; Bottom, IC_{50} curves for the bifunctional 1(2H)-phthalazinone-based targeted probes.

growth medium, 0.1% DMSO) for 20 minutes, before the compound-containing medium was removed. AZD2281-TCO (**2.7**) was then added (3 μM in growth medium, 0.1% DMSO) and the mixture was incubated for another 20 minutes. Texas Red-Tz (**2.8**) cleared out of the cells very quickly, allowing the identification of AZD2281-Texas Red (**2.9**), which stayed with its target for long periods of time. After washing, fixing and

permeabilizing the MDA-MB-436 cells, PARP1 was visualized using monoclonal antibodies (Mabs; Figure 2.4b). Staining patterns for the Texas Red dye (Figure 2.4a) showed that it not only localized in the nucleus, but also accumulated in the nucleolus. Whilst anti-PARP1 Mabs showed similar nuclear localization (Figure 2.4b), there was an absence of Mab signal in the nucleoli. This was presumably due to steric hindrance and not to the absence of PARP in the nucleolus, as earlier reports have indicated[36,37]. The results in Figure 2.4c confirm that there was excellent spatial correlation between the small molecules (AZD2281-TCO (**2.7**)/Texas Red-Tz (**2.8**)). We also constructed a PARP1-GFP fusion protein and expressed it in MDA-MB-436 cells as an independent confirmation of probe localization. In the PARP1-GFP expressing cells, GFP expression was clearly observed, primarily in the nucleoli but also in the nucleus (Figure 2.5). This pattern was identical to that seen with the AZD2281-TCO/Texas Red-Tz pair.

Interestingly, incubation of live cells with Texas Red-Tz (**2.8**) without AZD2281-TCO (**2.7**) did not lead to nuclear localization of the dye. Instead, there was non-preferential distribution of fluorescence in the perinuclear cytoplasmic region, as well as in the nucleus (ratio = 0.95:1). When incubated with different concentrations of the trans-cyclooctene probe (**2.7**; 3–10 nM), the nuclear/cytoplasmic signal ratios gradually increased (Figure 2.4d, not blocked). This concentration-dependent binding of AZD2281-TCO (**2.7**) to PARP1 can be inhibited with 30-fold excess of AZD2281 (**2.1**). This prevents nuclear localization and therefore binding of probe **2.7** to PARP1. With different concentrations of **2.7**, the nuclear/cytoplasmic signal ratio remains unchanged (Figure 2.4d, blocked).

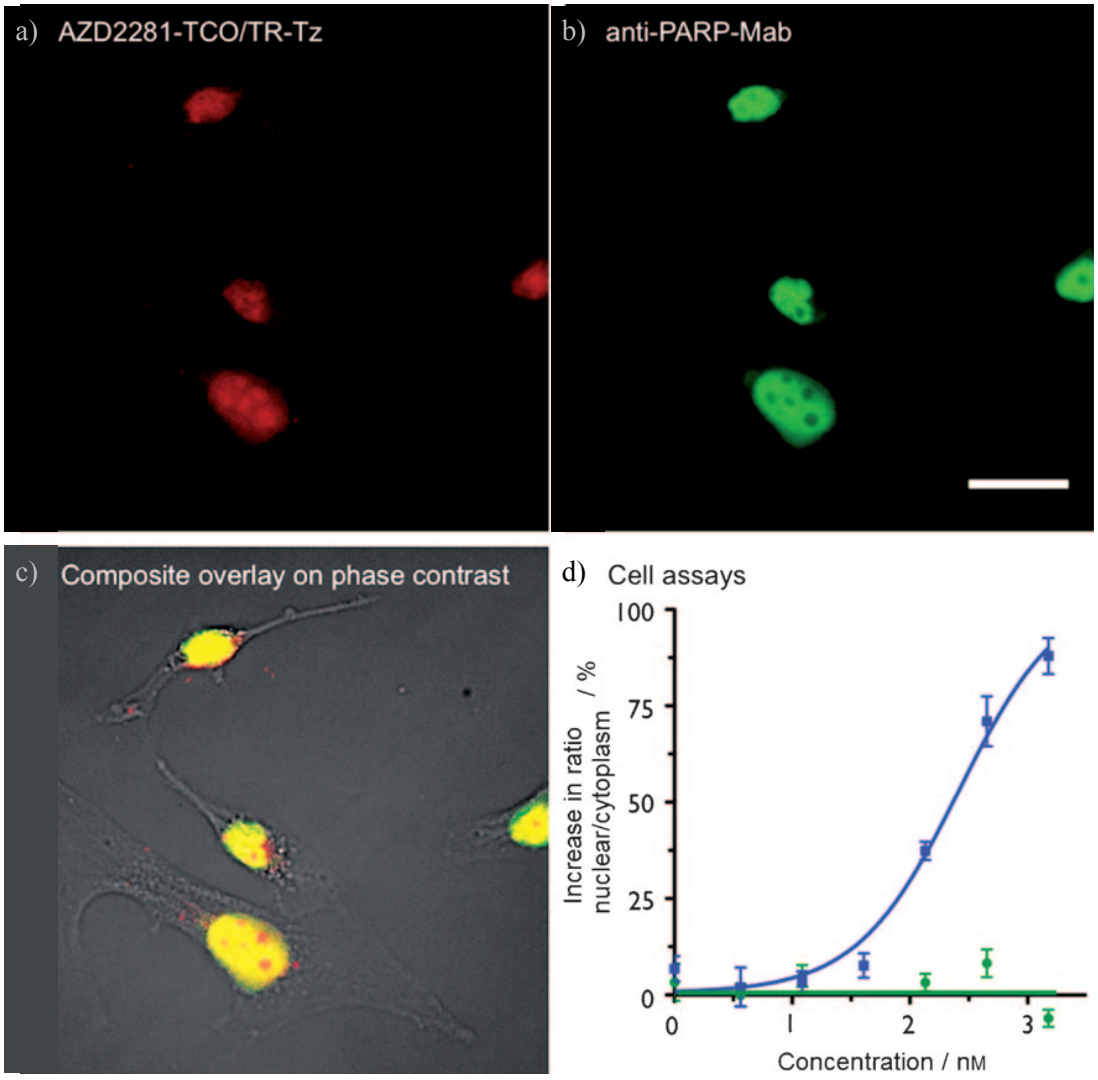

Figure 2.4. Two-step imaging with AZD2281-TCO/TR-Tz in cells. The reaction of AZD2281-TCO (**2.7**) and Texas Red-Tz (**2.8**) in MDA-MB436 cells. a) AZD2281-TCO reacted with Texas Red-Tz; speckles outside the cells, presumably resulting from precipitated Texas Red-Tz (**2.8**), were removed. b) anti-PARP1 monoclonal antibody staining. c) a composite overlay on phase contrast. d) the ratio of nuclear/cytoplasmic signal for AZD2281-TCO/Texas Red-Tz in the absence (not blocked: blue squares) and presence (blocked: green circles) of blocking reagent AZD2281. Scale bar: 20 μm.

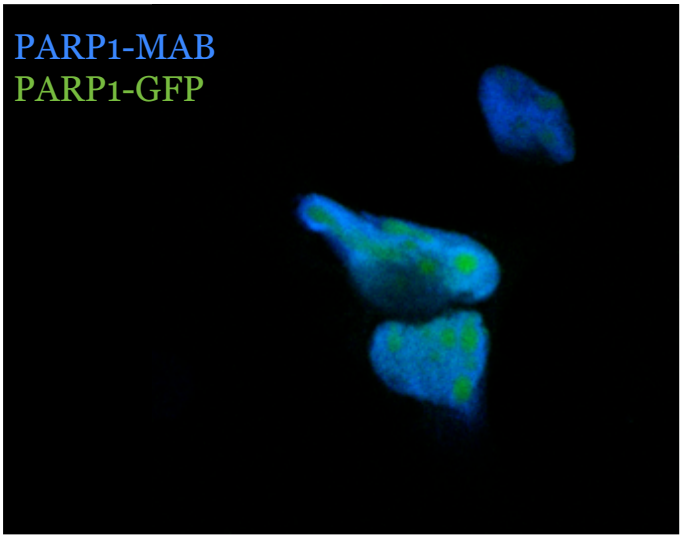

Figure 2.5. PARP1-GFP expression is visible in the nucleoli of MDA-MB-436 cells.

Like its two building blocks **2.7** and **2.8**, pre-reacted AZD2281-Texas Red (**2.9**) is able to penetrate the nuclear membranes in live cells, although incubation of MDA-MB-436 with **2.9** leads to lower nuclear/cytoplasmic localization ratios (modest increase of 38 ± 2%). The superior results of sequential treatment of MDA-MB-436 cells with AZD2281-TCO (**2.7**) and Texas Red-Tz (**2.8**) demonstrates the advantages of a bio-orthogonal *in vivo* reaction, since both partners (the targeting molecule **2.7** as well as the fluorophore **2.8**) are small in size (**2.7**: 674.76 g mol^{-1}; **2.8**: 889.05 g mol^{-1}), and this contributes to easier permeation. Once assembled, however, penetration is less efficient leading to trapping of the conjugate and high target-to-background ratios.

2.3. Materials and Methods

Unless otherwise noted, all reagents were purchased from Sigma-Aldrich (St. Louis, MO, USA) and used without further purification. Texas Red-X, succinimidyl ester was

purchased from Invitrogen (Carlsbad, CA, USA). Cyclohexylcarbodiimide polystyrene resin was purchased from EMD biosciences (Gibbstown, NJ, USA). LC-ESI-MS analysis and HPLC purifications were performed on a Waters (Milford, MA, USA) LC-MS system. For LC-ESI-MS analyses, a Waters XTerra® C18 5 μm column was used. For preparative runs, an Atlantis® Prep T3 OBDTM 5 μM column was used. High-resolution electrospray ionization (ESI) mass spectra were obtained on a Bruker Daltonics APEXIV 4.7 Tesla Fourier Transform mass spectrometer (FT-ICR-MS) in the Department of Chemistry Instrumentation Facility (Massachusetts Institute of Technology, Cambridge, MA, USA). Cellular images were taken on a Nikon (Tokyo, Japan) Eclipse 80i microscope with either a Nikon Plan Apo 40X/0.95 air or a Nikon Plan Apo 60X/1.45 oil immersion objective. IC_{50} assays were analyzed using a Tecan (Männedorf, Switzerland) Safire^2 microplate system. All kinetic data were analyzed using Prism 4 (GraphPad, La Jolla, CA, USA) for Mac.

2.3.1. Synthesis

Texas Red-Tz (**2.8**) was synthesized similar to methods described earlier[5,33,34]. (Cyclopropanecarbonyl)piperazine-1-carbonyl]-4-fluorophenyl]methyl]-2H-phthalazin-1-one (**2.1**)[32], 4-[[4-Fluoro-3-(piperazine-1-carbonyl)phenyl]methyl]-2H-phthalazin-1-one (**2.2**)[32] and (E)-cyclooct-4-enyl 2,5-dioxopyrrolidin-1-yl carbonate (**2.5**)[5] were synthesized as described earlier.

4-[[4-Fluoro-3-(4-(5-oxopentanamide)piperazine-1-carbonyl)phenyl]methyl]-2H-phthalazin-1-one (**2.3**).

Glutaric anhydride (0.50 g, 4.37 mmol) and N,N- diisopropylethylamine (2.28 mL, 13.11 mmol) were added to a solution of 4-[[4-Fluoro-3-(piperazine-1-carbonyl)phenyl] methyl]-2H-phthalazin-1-one (**2.2**) (1.60 g, 4.37 mmol) in dichloromethane (50 mL) and the reaction mixture and stirred for 30 min. Water (50 mL) was then added and the reaction mixture stirred for another 30 min. The reaction mixture was acidified with HCl to pH 2, the organic phase separated and the aqueous phase extracted with dichloromethane (3x 30 mL). The combined organic phases were dried over $MgSO_4$ and volatiles removed *in vacuo*. The resulting crude material was purified using silica chromatography (0%-30% MeOH/DCM), yielding the pure product as an off-white solid (1.52 g, 3.16 mmol, 72%). ^{1}H NMR (400 MHz, CD_3OD, * indicates rotamer peak) δ = 8.35 (d, 1H, $^3J_{HH}$ = 7.7, $C_{arom}H$), 8.25 (s, 1H, $^3J_{HH}$), 7.94 (d, 1H, $^3J_{HH}$ = 7.7, $C_{arom}H$), 7.90-7.78 (m, 2H, $C_{arom}H$), 7.49-7.46 (m, 1H, $C_{arom}H$), 7.39-7.36 (m, 1H, $C_{arom}H$), 7.15 (t, 1H, $^3J_{HH}$ = 9.0, $C_{arom}H$), 4.37 (s, 2H, CH_2), 3.81-3.71 (m, 2H, CH_2), 3.68-3.62 (m, 2H, CH_2), 3.54-3.46 (m, 2H, CH_2), 3.36-3.26 (m, 2H, CH_2), 2.50 (t, 2H, $^3J_{HH}$ = 7.4, CH_2), 2.43 (t, 2H, $^3J_{HH}$ = 7.4, *CH_2), 2.38 (t, 2H, $^3J_{HH}$ = 7.0, CH2), 2.36 (t, 2H, $^3J_{HH}$ = 7.0, *CH_2), 1.92-1.83 (m, 2H, CH_2, *CH_2); ^{19}F NMR (376 MHz, CD_3OD) δ = -121.14; LC-ESI-MS(-) m/z = 479.2 $[M-H^+]^-$, 959.3 $[2M-H^+]^-$; LC-ESI-MS(+) m/z = 481.3 $[M+H^+]^+$, 961.5 $[2M+H^+]^+$. HRMS-ESI $[M+H]^+$ m/z calcd. for $[C_{25}H_{25}FN_4O_5]^+$ 481.1882, found 481.1862.

4-[[4-Fluoro-3-(4-(N-(2-aminoethyl)-5-oxo-pentanamide)piperazine-1-carbonyl)phenyl]methyl]-2H-phthalazin-1-one (**2.4**).

Cyclohexylcarbodiimide polystyrene resin (634 mg, 2.3 mmol/g) was added to a solution of 4-[[4-Fluoro-3-(4-(5-oxopentanamide)piperazine-1-carbonyl)phenyl]methyl]-2H-phthalazin-1-one (**2.3**) (350 mg, 0.73 mmol) in dichloromethane (20 mL) and the resulting mixture stirred gently for 7 h at room temperature. Subsequently, ethylenediamine (976 μL, 14.6 mmol) was added and the reaction mixture stirred for another 60 min, before the reaction mixture was filtered and volatiles removed *in vacuo*. The crude material was purified via HPLC, yielding the title compound as a clear solid (62 mg, 0.12 mmol, 16%). ^{1}H NMR (400 MHz, CD_3OD, * indicates rotamer peak) δ = 8.37 (d, 1H, $^{3}J_{HH}$ = 7.7, $C_{arom}H$), 7.97 (d, 1H, $^{3}J_{HH}$ = 6.6, $C_{arom}H$), 7.91-7.82 (m, 2H, $C_{arom}H$), 7.53-7.48 (m, 1H, $C_{arom}H$), 7.40-7.36 (m, 1H, $C_{arom}H$), 7.17 (t, 1H, $^{3}J_{HH}$ = 8.9, $C_{arom}H$), 4.39 (s, 2H, CH_2), 3.82-3.72 (m, 2H, CH_2), 3.68-3.64 (m, 2H, CH_2), 3.53-3.48 (m, 2H, CH_2), 3.46 (t, 2H, $^{3}J_{HH}$ = 5.7, CH_2), 3.38-3.28 (m, 2H, CH_2), 3.06 (t, 2H, $^{3}J_{HH}$ = 5.7, CH_2), 2.52 (t, 2H, $^{3}J_{HH}$ = 7.2, CH_2), 2.45 (t, 2H, $^{3}J_{HH}$ = 7.1, *CH_2), 2.32 (t, 2H, $^{3}J_{HH}$ = 7.1, CH_2), 2.31 (t, 2H, $^{3}J_{HH}$ = 6.9, *CH_2), 1.96-1.86 (m, 2H, CH_2, *CH_2); ^{19}F NMR (376 MHz, CD_3OD) δ = -121.19; LC-ESI-MS(-) m/z = 521.3 $[M\text{-}H^{+}]^{-}$ (100); LC-ESI-MS(+) m/z = 523.4 $[M+H^{+}]^{+}$. HRMS-ESI $[M+H]^{+}$ m/z calcd. for $[C_{27}H_{31}FN_6O_4]^{+}$ 523.2464, found 523.2464.

AZD2281-NOB (**2.6**).

Cyclohexylcarbodiimide polystyrene resin (33 mg, 2.3 mmol/g) and triethylamine (16 μL, 0.11 mmol) were added to a solution of 4-[[4-Fluoro-3-(4-(N-(2-aminoethyl)-5-oxo-pentanamide)piperazine-1-carbonyl)phenyl] methyl]-2H-phthalazin-1-one (**2.4**) (20 mg, 38 μmol) and 5-norbornene-2-carboxylic acid (11 mg, 77 μmol) in dichloromethane (1 mL) and the resulting mixture stirred gently over night at room temperature. Subsequently, the reaction mixture was filtered and volatiles removed *in vacuo*. The crude material was purified via HPLC, yielding the title compound as a clear solid (5.9 mg, 9 μmol, 24%). ^{1}H NMR (400 MHz, CD_3OD, * indicates rotamer peak, not all peaks integrated due to endo/exo-mixture) δ = 8.37 (d, 1H, $^{3}J_{HH}$ = 7.4, $C_{arom}H$), 7.80-7.82 (m, 3H, $C_{arom}H$), 7.51-7.48 (m, 1H, $C_{arom}H$), 7.40-7.36 (m, 1H, $C_{arom}H$), 7.17 (m, 1H, $C_{arom}H$), 6.18-6.09 (m), 5.92-5.86 (m), 4.39 (s, 2H, CH_2), 3.80-3.21 (m), 3.13 (m), 3.01 (s), 2.87-2.81 (m), 2.47 (t, 2H, $^{3}J_{HH}$ = 7.2, CH_2), 2.40 (t, 2H, $^{3}J_{HH}$ = 7.1, *CH_2), 2.27-1.80 (m), 1.68-1.22 (m); ^{19}F NMR (376 MHz, CD_3OD) δ = -121.20; LC-ESI-MS(-) m/z = 641.3 $[M\text{-}H^{+}]^{-}$; LC-ESI-MS(+) m/z = 643.5 $[M+H^{+}]^{+}$. HRMS-ESI $[M+H]^{+}$ m/z calcd. for $[C_{35}H_{39}FN_6O_5]^{+}$ 643.3039, found 643.3022.

AZD2281-TCO (**2.7**).

Triethylamine (16 μL, 0.11 mmol) was added to a solution of 4-[[4-Fluoro-3-(4-(N-(2-aminoethyl)-5-oxo-pentanamide) piperazine-1-carbonyl)phenyl] methyl]-2H-phthalazin-1-one (**2.4**) (20 mg, 38 μmol) and (E)-cyclooct-4-enyl-2,5-dioxopyrrolidin-1-yl carbonate (**2.5**) (12 mg, 46 μmol) in dichloromethane (1 mL) and the resulting mixture

stirred gently over night at room temperature. Subsequently, the reaction mixture was filtered and volatiles removed *in vacuo*. The crude material was purified via HPLC, yielding the title compound as a clear solid (11.3 mg, 17 μmol, 44%). ^{1}H NMR (400 MHz, CD_3OD, * indicates rotamer peak) δ = 8.39-8.36 (m, 2H, $C_{arom}H$, NH), 8.02-8.00 (m, 1H, NH), 7.98-7.94 (m, 1H, $C_{arom}H$), 7.91-7.82 (m, 2H, $C_{arom}H$), 7.51-7.48 (m, 1H, $C_{arom}H$), 7.40-7.37 (m, 1H, $C_{arom}H$), 7.17 (t, 1H, $^{3}J_{HH}$ = 9.0, CaromH), 6.77-6.76 (m, 1H, NH), 5.65-5.55 (m, 1H, CH), 5.50-5.40 (m, 1H, CH), 4.39 (s, 2H, CH_2), 4.31-4.27 (m, 1H, CH), 3.82-3.13 (m, 8H, CH_2), 2.46 (t, 2H, $^{3}J_{HH}$ = 7.4, CH_2), 2.39 (t, 2H, $^{3}J_{HH}$ = 7.4, *CH_2), 2.33-1.53 (m, 14H, CH_2, *CH_2); ^{19}F NMR (376 MHz, CD_3OD) δ = -121.20; LC-ESI-MS(-) m/z = 673.3 $[M\text{-}H^+]^-$; LC-ESI-MS(+) m/z = 675.4 $[M+H^+]^+$; HRMS-ESI $[M+H]^+$ m/z calcd. for $[C_{36}H_{43}FN_6O_6]^+$ 675.3301, found 675.3301.

2.3.2. HPLC characterization of reaction between Texas Red-tetrazine (**2.8**) and AZD2281-TCO (**2.7**)

AZD2281-TCO (**2.7**) and Texas Red-tetrazine (**2.8**) were combined in 40 μL of DMSO/PBS at a final concentration of 0.3 mM for each reagent. The solution was stirred for several minutes at room temperature, yielding AZD2281-Texas Red (**2.9**).

2.3.3. PARP1 IC_{50} determination

A commercially available colorimetric assay (Trevigen, Gaithersburg, MD, USA) was used to measure PARP activity *in vitro* in the presence of inhibitors. Ten-fold dilutions of AZD2281-derivatives (**2.6**) (final concentration 400 nM to 0.04 nM); and (**2.7**), (**2.9**) (4

μM to 0.04 nM) were incubated with 0.5 units PARP HSA for 10 minutes in histone-coated 96-well plates. All experiments were carried out in triplicate. Control samples did not contain inhibitor and background measurement samples did not contain PARP1. All reaction mixtures were adjusted to a final volume of 50 uL and a maximum final concentration 0.4% DMSO in assay buffer. The remainder of the assay was performed according to the manufacturer's instructions. PARP1 activity was measured by absorbance at 450 nm in each well using a Safire^2 microplate reader (Tecan Group, Mannedorf, Switzerland). IC_{50} values were calculated using Prism software (GraphPad, La Jolla, CA, USA).

2.3.4. Cell Culture

MDA-MB-231 and MDA-MB-436 cells were obtained from the ATCC and cultured in RPMI 1640 supplemented with 10% fetal bovine serum, L-glutamine, and penicillin/streptomycin. MDA-MB-231 and MDA-MD-436 cells stably expressing PARP-GFP were derived by transfection with Lipofectamine 2000 (Invitrogen) and isolation of individual G418-resistant clones. Cells were maintained in growth medium containing 1 mg/mL G418. Expression of PARP-GFP in MDA-MB-436 cells was verified using immunofluorescence microscopy to show nuclear localization of PARP-GFP, and western blotting for PARP-GFP.

2.3.5. *In vitro* cell assays

For AZD2281-TCO IC_{50} assays, MDA-MB-436 cells (500 μL, 80.000 cells/mL) were seeded into glycerine-treated 8-well chamber slides (Lab TekTM, Thermo Scientific,

Rochester, NY, USA), and allowed to attach over night. Cells were then incubated with Texas Red-Tz (**2.8**) (25 µL, 20 µM) for 20 minutes (37°C) before the medium was removed and cells were washed (1x, medium, 500 µL). Subsequently, 500 µL medium, Hoechst 33258 (10 µL , 100x in PBS) and AZD2281-TCO (**2.7**) (25 µL, in PBS, 3% DMSO, 30 µM-100 nM) were added and incubated at 37°C for 20 min. Cells were washed with PBS (3x 500 µL), fixed with paraformaldehyde (4% in PBS) and washed with PBS (3x 500 µL, time between each wash = 5 min). PBS was removed and cells mounted using Prolong Gold (Invitrogen, Carlsbad, CA, USA) before imaging. For AZD2281-TCO blocking experiments, MDA-MB-436 cells (500 µL, 80,000 cells/mL) were seeded into glycerine-treated 8-well chamber slides (Lab TekTM, Thermo Scientific, Rochester, NY, USA), and allowed to attach over night. Cells were then incubated with Texas Red-Tz (**2.8**) (25 µL, 20 µM) for 20 minutes (37°C) before the medium was removed and cells were washed (1x, medium, 500 µL). Subsequently, 500 µL medium, Hoechst 33258 (10 µL , 100x in PBS), AZD2281 (**2.1**) (5 µL in DMSO, 10 mM) and AZD2281-TCO (**2.7**) (25 µL, in PBS, 3% DMSO, 30 µM-100 nM) were added and incubated at 37°C for 20 min. Cells were washed with PBS (3x 500 µL), fixed with paraformaldehyde (4% in PBS) and washed with PBS (3x 500 µL, time between each wash = 5 min). PBS was removed and cells mounted using Prolong Gold (Invitrogen, Carlsbad, CA, USA) before imaging.

2.3.6. Image analysis

Cells were observed on a Nikon 80i (Nikon, Tokyo, Japan) microscope equipped with an ImagEM camera (Hammamatsu Photonics, Tokyo, Japan). Images detailing distinct

and separate cellular regions were obtained with the following filters: (Dapi, excitation 350 ± 50 nm, emission 460 ± 50 nm, dichroic 400LP; IgG Pab, excitation 480 ± 20 nm, emission 535 ± 25 nm, dichroic 505LP; Texas Red-Tz (**2.8**), excitation 560 ± 20 nm, emission 630 ± 30 nm, dichroic 595DCLP; Chroma Technology, Bellows Falls, VT, USA) Images in each channel were captured using identical acquisition parameters. For each image, both cell structures and nuclei structures have been obtained using the appropriate fluorescence filters and appropriate excitation signal levels to avoid collecting auto-fluorescence. The collected data was then pre-processed with Cellprofiler[38] and statistics collected using Matlab (The Mathworks, Waltham, MA, USA). Cell structures were then identified using Otsu's method[39] and binary masks were generated matching the boundary of each cell structure. Within each image and for each cell, the fluorescence signal for the total cell and the signal in the nuclear area was calculated using the corresponding mask as a spatial filter. The two signals were then normalized for their total areas. The ratio of the fluorescent signal in the cytosol region over the signal in the nuclear region was then calculated. Background subtraction was performed on the normalized signal using the cell's negative masks. For all cells we chose an optimal ratio between 0.35 and 0.48 for the cytosol area over the nucleus area.

2.3.7. MDA-MB436 cellular imaging

MDA-MB-436 cells (500 µL, 80.000 cells/mL) were seeded into glycerine-treated 8-well chamber slides (Lab TekTM, Thermo Scientific, Rochester, NY, USA), and allowed to attach over night. They were incubated with Texas Red-Tz (**2.8**) (25 µL, 20 µM) for 20 minutes (37°C) before the medium was removed and cells were washed (1x, medium,

500 μL). Subsequently, 500 μL medium and AZD2281-TCO (**2.7**) (25 μL, in PBS, 3% DMSO, 30 μM) were added and incubated at 37°C for 20 min. Cells were washed with PBS (3x 500 μL), fixed with paraformaldehyde (4% in PBS) and washed with PBS (3x 500 μL, time between each wash = 5 min). Cells were permeabilized using Triton-X-100 (2% in PBS, 10 min) and incubated with anti-PARP-1 Mab (EMD biosciences, Gibbstown, NJ, USA) for 3h, before stained with secondary IgG-GFP Pab (EMD biosciences, Gibbstown, NJ, USA). PBS was removed and cells mounted using Prolong Gold (Invitrogen, Carlsbad, CA, USA) before imaging.

2.3.8. PARP1-GFP reporter construct

PARP-GFP was constructed by PCR of human PARP-1 from Open Biosystems clone 5193735 from the NIH_MGC_114 cDNA library, and cloning into pAcGFP-N1 between XhoI and XmaI restriction sites. The PARP-GFP construct was verified by DNA sequencing.

2.3.9. PARP-1-GFP MDA-MB-436 cellular imaging

PARP-1-GFP expressing MDA-MB-436 cells (500 μL, 80,000 cells/mL) were seeded into glycerine-treated 8-well chamber slides (Lab Tek, Thermo Scientific, Rochester, NY, USA), and allowed to attach over night. They were washed with PBS (3x 500 μL), fixed with paraformaldehyde (4% in PBS) and washed with PBS (3x 500 μL, time between each wash = 5 min). Cells were permeabilized using Triton-X-100 (0.5% in PBS, 10 min) and incubated with anti-PARP1 Mab (EMD biosciences, Gibbstown, NJ, USA) for 3h,

before stained with secondary IgG-GFP Pab (EMD biosciences). PBS was removed and cells mounted using Prolong Gold (Invitrogen) before imaging.

2.4. Discussion

In this report, we present potential small-molecule-based PARP1 imaging agents and confirm their utility for cell imaging. We found that AZD2281-based bifunctional small molecules were most suited to bioorthogonal *in vivo* target assembly. All bioorthogonal and imaging probes had IC_{50} values ranging between 10.1 nM and 15.4 nM. In particular, the TCO-modified derivative was not only successfully reacted using a bioorthogonal cycloaddition in cells, but was found to colocalize with anti-PARP1 Mabs. In turn, this colocalization could be prevented by blocking the targeted fluorescent probe with AZD2281. The design strategy employed here, as well as the specific compounds investigated, should prove useful for the future study of PARP1 biology in live cells. It is also highly likely that similar strategies could be used for the design of positron emission tomography (PET) imaging agents for whole-body imaging of PARP1 and its inhibition by PARPi. Such agents would be particularly useful in drug development and clinical trials.

2.5. Acknowledgements

We thank Drs. Ralph Mazitschek, Neal Devaraj, Scott Hilderbrand and Claudio Vinegoni for many helpful discussions, Dr. Yvonna Fisher-Jeffes for manuscript review, and Joshua Dunham for image processing. This research was supported in part by the

National Cancer Institute (NCI, USA) grants P50 CA86 355 and NIBIB RO1 EB-010 011. A.T. was supported by a National Institutes of Health (NIH, USA) grant NIGMS T32 GM008313. T.R. was supported by a grant from the German National Academy of Sciences Leopoldina (LPDS-2009-24).

2.6. ^{18}F-PARP1 Inhibitors

Two subsequent publications from our group demonstrated chemical synthesis and PET imaging using ^{18}F-PARP1 inhibitors. By using two-step ^{18}F labeling via the [4+2] Diels-Alder cycloaddition described above, any tetrazine-modified small-molecule can be modified into a PET imaging agent for *in vivo* use, with higher yields as compared to direct fluorination.

An ^{18}F-labeled PARP1 imaging agent, based on AZD2281, was prepared via an inverse electron demand Diels–Alder cycloaddition in high radiochemical yield for positron emission tomography (PET) imaging. This strain-promoted 'bioorthogonal' reaction is envisioned to be a widely applicable ^{18}F-labeling strategy for repeat and on-demand synthesis of small molecules for PET imaging.

Adapted from:

Edmund J. Keliher*, Thomas Reiner*, Anna Turetsky, Scott A. Hilderbrand, and Ralph Weissleder. High-Yielding, Two-Step ^{18}F Labeling Strategy for ^{18}F-PARP1 inhibitors. *ChemMedChem*, 6: 424–427 (2011). doi: 10.1002/cmdc.201000426. *Equal contribution

E.J.K. and T.R. designed experiments and performed chemical synthesis and characterization. E.J.K., T.R., and R.W. designed the study, prepared figures and wrote the manuscript. A.T. performed PARP1 inhibition assays and analyzed resulting data. All authors reviewed and edited the manuscript.

See Appendix A for detailed synthetic methods.

Positron emission tomography (PET) of labeled metabolites, drugs, proteins and nanomaterials is rapidly emerging as a powerful imaging tool to detect and monitor the stages of disease, to study human biology, to investigate pharmacokinetics and pharmacodynamics of new drugs, or to measure treatment efficacy in clinical trials[40-46]. ^{18}F is one of the most commonly used isotopes for clinical imaging given its half-life, ease of production, wide availability, and compatibility with microfluidic syntheses[47]. Despite extensive use and well-established procedures of labeling some small molecules, facile ^{18}F platform-type universally adaptable labeling strategies are still largely missing. This is especially true for rapid labeling of small molecules that emerge from high-throughput screens or for optimizing hybrid and modular imaging agents. Bioorthogonal chemistries represent one avenue to develop such generic labeling platforms.

To date, several bioorthogonal reactions have been described[35,48-52] but only a few have been adapted for isotope labeling. The most popular reaction is the 1,3-dipolar cycloaddition, "click" reaction, between azides and alkynes[47,53]. These reactions were found to be particularly useful for *in vitro* ^{18}F-fluorination of biomolecules and are now

commonly used[4,54,55]. Our search for alternative, more rapid, selective, and chemically accessible coupling reactions without need for a catalyst led us to investigate the [4+2] inverse electron demand Diels–Alder cycloaddition using trans-cyclooctenes (TCO) and tetrazines (Tz)[5,33,34]. Advantages of the TCO/Tz labeling strategy include : a) fast reaction times in excess of 6,000 m^{-1} s^{-1}; b) high selectivity ; c) no need for elevated temperatures or catalysts ; d) bio-compatible reaction conditions; and e) activatable tetrazines[34].

Here, we extend our previous work on TCO and Tz chemistry[5,33,34,56] and show that the Diels–Alder cycloaddition can be used for rapid ^{18}F labeling of drugs. This strategy allows one to piggy-back onto the development of the vast number of small-molecule affinity ligands, peptides, and antibodies with various protein targets. Using PARP1 as a model target and AZD2281 as a well-developed nanomolar affinity ligand[28,57], we show that the TCO/Tz strategy can be used to efficiently label the drug scaffold in very short times and at exceptionally high yields. This contrasts to conventional synthesis of directly ^{18}F-fluorinated AZD2281 derivatives where yields are much lower. We show the successful fully automated synthesis of a ^{18}F-labeled TCO, its conjugation with a tetrazine-modified AZD2281, and compare affinities of the parent drugs and intermediates. The described platform-based methodology is modular and could easily be adapted to other molecularly targeted drug scaffolds of interest.

There are three generic ^{18}F labeling strategies for AZD2281: a) de novo synthesis of the native compound substituting ^{18}F for the aryl fluorine atom; b) conventional tosylation and subsequent fluorination of hydroxy-AZD2281 derivatives ; and c) prosthetic group labeling followed by conjugation to the parent compound. The first

choice would result in a chemically identical drug but synthetic steps would be lengthy, requiring purification of intermediates, which may not be feasible given the short half-life of ^{18}F, and it would be impractical for repetition for on-demand synthesis in a clinical setting. We therefore focused on the prosthetic group approach using the TCO/Tz chemistry. While ^{18}F labeling of either TCO or Tz is conceivable, preliminary experiments demonstrated the substituted 1,2,4,5-tetrazine moiety was not stable to commonly used mild nucleophilic fluorination conditions: tetrabutyl ammonium bicarbonate, potassium fluoride, pH 8.5, 40°C. Therefore, focus was turned to the design and synthesis of an ^{18}F-labeled TCO in which labeling would take place away from the cyclooctenyl ring due to susceptibility of that system to isomerization to bicyclo[3.3.0]octenes[58]. (Z)-2-(Cyclooct-4-enyloxy)acetic acid (**2.11**) was prepared in 63% yield over two steps from commercially available (Z)-cyclooct-4-enol (**2.10;** Figure 2.6). Carboxylic acid **2.11** was converted to (E)-2-(cyclooct-4-enyloxy)ethanol (**2.13**) first by lithium aluminum hydride ($LiAlH_4$) reduction to give (Z)-2-(cyclooct-4-enyloxy)ethanol (**2.12**) in 78% yield, followed by photochemical cis/trans isomerization and isolation of the (E)-isomers by the previously described cycle/trap method[35]. The major (E)-cyclooctyl stereoisomer was isolated by column chromatography and converted to the corresponding tosylate **2.14** in 84% yield. (E)-5-(2-Fluoroethoxy)cyclooct-1-ene (**2.15^{19}F**) was prepared in 91% yield by the treatment of **2.14** with tetrabutylammonium fluoride (TBAF) in THF. All previously unknown compounds were fully characterized by ^{1}H, ^{13}C, and ^{19}F NMR.

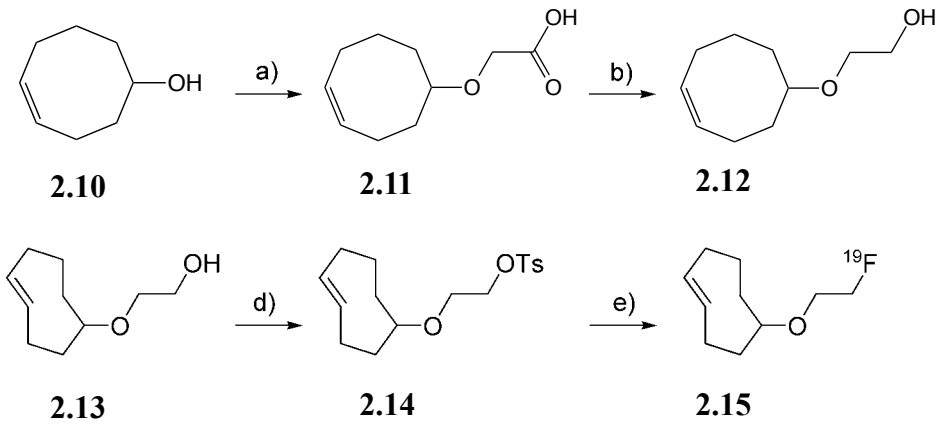

Figure 2.6. Synthetic scheme for the synthesis of radiolabeled ^{18}F-TCO (**2.15^{18}F**). Reagents and conditions: a) NaH, ICH_2CO_2H, THF, reflux, 4 h, 66%; b) $LiAlH_4$, Et_2O, 0°C, RT, 24 h, 78%; c) Et_2O/hexanes (9 :1), hν, RT, 8 h, 37%; d) TsCl, Et_3N, CH_3CN, RT, 2 h, 84 ; e) TBAF, THF, RT, 2 h, 91%.

As a precursor for the chemoselective reactive PARP1 inhibitor AZD2281-Tz (**2.17**), 4-[[4-fluoro-3-(4-(5-oxopentanamide)piperazine-1-carbonyl)phenyl]methyl]-2H-phthalazin-1-one (**2.3**) was generated according to known literature procedures[56]. This precursor was reacted with **2.16**[33] in the presence of polymer-supported N,N'-dicyclohexylcarbodiimide (DCC) beads to yield **2.17** as a pink solid. Cycloadduct **2.18^{19}F** was prepared by the addition of dimethyl sulfoxide (DMSO) solutions of **2.17** and **2.15^{19}F** at room temperature and subsequent high-pressure liquid chromatography (HPLC) purification (Figure 2.7).

Radiofluorination of **2.14** was performed following a modified procedure previously described for the ^{18}F labeling of 1-azido-2-(2-(2-18F-fluoroethoxy)ethoxy)ethane[6]. In brief, no carrier added (n.c.a.) ^{18}F-fluoride ($^{18}F^-$) in ^{18}O-enriched H_2O obtained from

PETNET Solutions and tetrabutylammonium bicarbonate (nBu$_4$NHCO$_3$) were dried by azeotropic distillation of the acetonitrile/water mixture under reduced pressure and a stream of argon. Tosylate **2.14** in DMSO was added to the dried ^{18}F$^-$(n.c.a.)/nBu$_4$NHCO$_3$ and heated to 90°C for 10 min. Filtration of the reaction mixture through alumina-N removed unreacted ^{18}F$^-$ prior to HPLC purification. Having a low UV absorbance, identification of the desired **2.15^{18}F** product was confirmed in a separate experiment by HPLC injection of **2.15^{19}F**, fraction collection at the same elution as observed for radioactive **2.15^{18}F**, and NMR analysis of the non-radioactive concentrate. HPLC purified **2.15^{18}F** was isolated from the collected HPLC solvents by C_{18} solid phase extraction

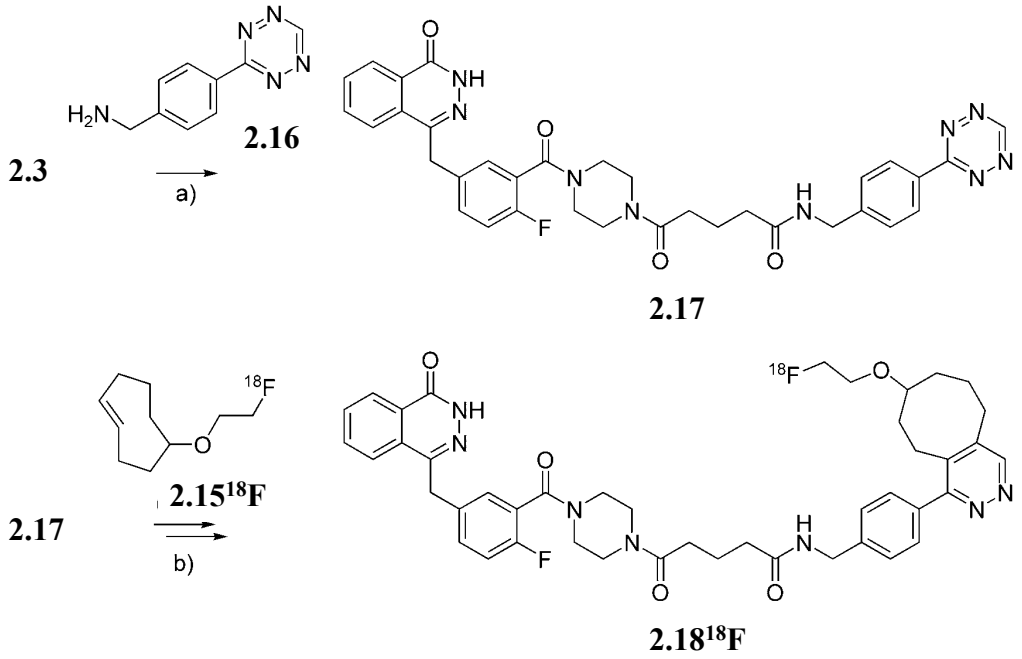

Figure 2.7. Synthetic scheme for the synthesis of radiolabeled AZD2281-^{18}F (**2.18^{18}F**). Reagents and conditions: a) polystyrene-bound DCC, Et_3N, CH_2Cl_2, RT, 7 h, 25%; b) CH_2Cl_2, RT, 3 min, 60%.

(SPE) and eluted with dichloromethane to give 7.7 ± 3.4 mCi (n = 16) **2.15^{18}F** in 44.7 ± 7.8% decay-corrected radiochemical yield (dcRCY) in an average time of 41 min from the start of drying of [^{18}F]-F$^-$ (n.c.a.). Analytical HPLC demonstrated >93% radiochemical purity of **2.15^{18}F**. Tetrazine **2.17** in DMSO was added to the **2.15^{18}F**/ CH_2Cl_2 solution, stirred for 3 min and subjected to HPLC purification (Figure 2.8). C_{18} SPE provided **2.18^{18}F** in 59.6 ± 5.0% isolated dcRCY (n = 3) with >96% radiochemical purity.

Compound **2.17** and AZD2281-Tz/trans-cyclooctene inverse electron demand Diels–Alder products **2.18^{19}F**, **2.18^{16}O**, and **2.18^{18}O** were analyzed using HPLC–mass

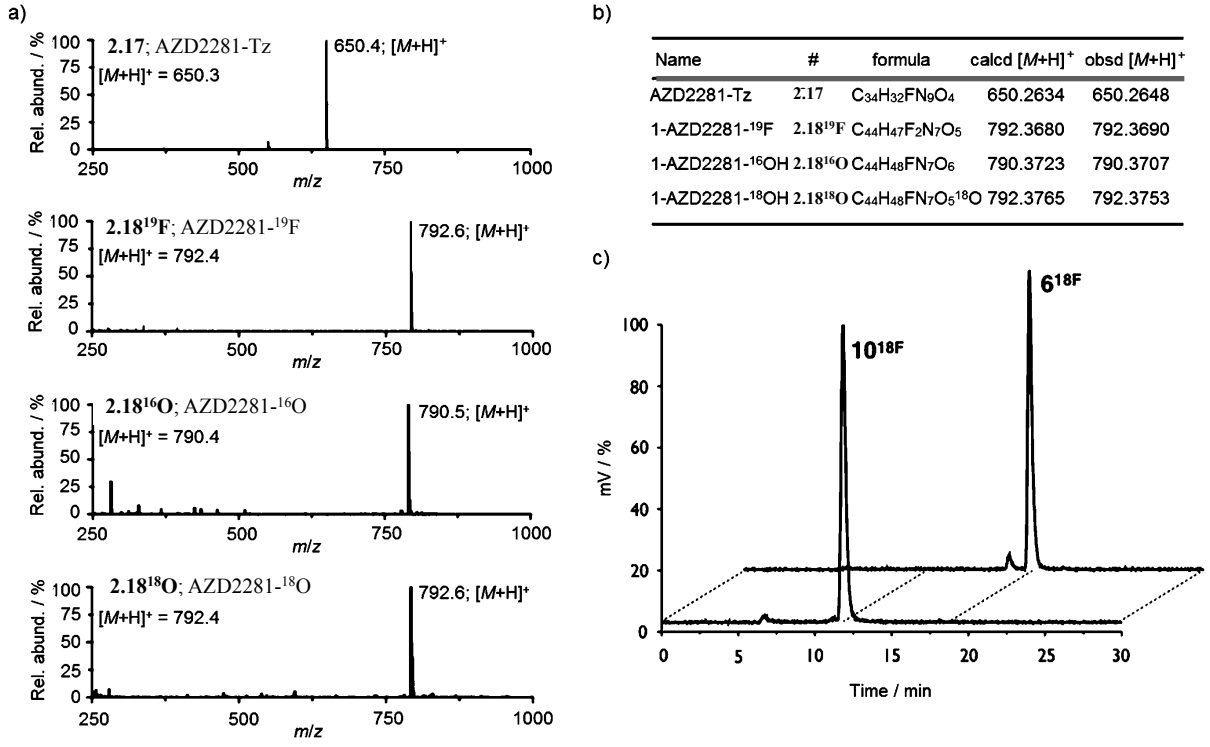

Figure 2.8. Characterization of radiolabeled compounds. a) LC/MS-ESI traces ; b) HRMS spectra of AZD2281-derivatives **2.17**, **2.18^{19}F**, **2.18^{16}O** and **2.18^{18}O** ; c) HPLC radiotraces of ^{18}F-labeled compounds **2.15^{18}F** and **2.18^{18}F**.

spectrometry (MS-ESI) (Figure 2.8). Under the reaction conditions for this cycloaddition, it was found that the initial dihydropyridazine products underwent aromatization to the corresponding pyridazines. LC/MS data confirmed the aromatization of the formed heterocycle, giving m/z values of 792.6, 790.5 and 792.6, respectively (calcd : 792.4, 790.4 and 792.4). To verify their elemental composition, compounds **2.17**, **2.18^{19}F**, **2.18^{16}O** and **2.18^{18}O** were also subjected to high-resolution mass spectrometry (HRMS). All measured values reflected the calculated masses. Furthermore, HRMS allowed the distinction between **2.18^{19}F** and **2.18^{18}O**, whose masses differ by 0.0085 g mol^{-1}, confirming the radioactive decay of **2.18^{18}F** to **2.18^{18}O** (Figure 2.8).

In addition to the above-described cycloadducts, we also prepared fluorinated AZD2281 analogues (Figure 2.9) using nucleophilic substitution. Two candidates were designed and synthesized based on known literature procedures[32]. 4-[[4-Fluoro- 3-(piperazine-1-carbonyl)phenyl]methyl]-2H-phthalazin-1-one was acylated with 6-

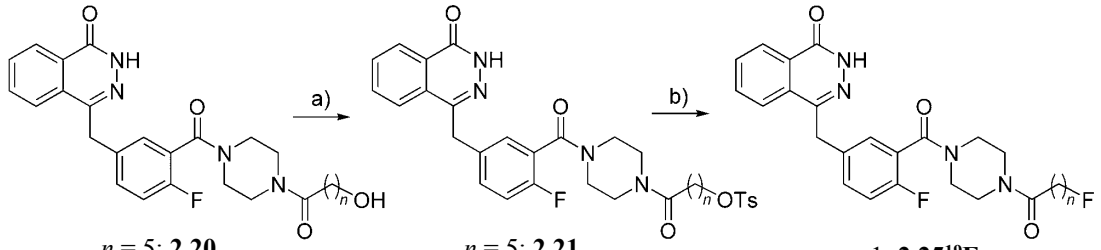

Figure 2.9. Synthetic scheme for the synthesis of conventionally fluorinated AZD2281 derivatives. Reagents and conditions : a) TsCl, Et_3N, CH_2Cl_2, RT, overnight, 24% for 13 and 32% for 16 ; b) NaF, CH_3CN, 40°C, 6 h, 16%.

hydroxyhexanoic acid or hydroxyacetic acid to give derivatives **2.20** and **2.23**. These hydroxy-AZD2281 derivatives were converted to the corresponding tosylates **2.21** and **2.24**. Attempts to fluorinate **2.21** resulted in decomposition of starting material, while the reaction of tosylate **2.24** with sodium fluoride provided **2.25^{19}F** in 14% yield. Standard ^{18}F radiolabeling conditions (Kryptofix-222 (K222), K_2CO_3), even at low temperatures (40°C), resulted in decomposition of the starting sulfonate ester **2.24**. Experiments were

a)

Class	Name	#	IC_{50} [nM]	Time ^{18}F	RCY	Conjugation technique
PARP1i	AZD2281-Tz	**2.17**	8.4 ± 1.3	NA	NA	
	1-AZD2281-^{19}F	**2.18^{19}F**	17.9 ± 1.1	3 min	60^%	DA cycloaddition
	2-AZD2281-^{19}F	**2.19^{19}F**	5.2 ± 1.1	30 min	<1^%	Nucleophilic substitution
TCO	^{19}F-TCO	**2.15^{19}F**	>4000	NA		

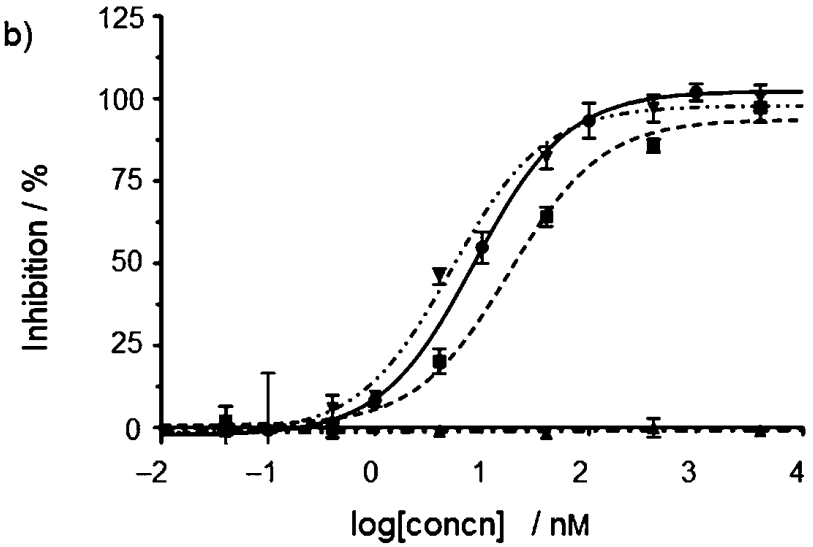

Figure 2.10. Inhibition of PARP1 by fluorinated AZD2281 derivatives. a) IC_{50} values and radiochemical yields (RCY) for derivatives **2.17**, **2.18^{19}F**, **2.19^{19}F** and **2.15^{19}F**; b) IC_{50} curves for PARP1 inhibitors **2.17** (circles), **2.18^{19}F** (squares), **2.19^{19}F** (upside-down pyramids) and trans-cyclooctene **2.15^{19}F** (pyramids).

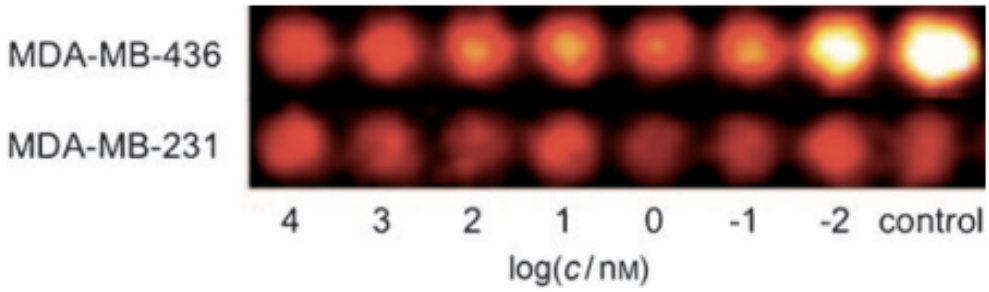

Figure 2.11[59]. Imaging of radioactivity in PARP1-high and PARP1-low cells following incubation with ^{18}F-AZD2281. MDA-MB-436 (PARP1 high) and MDA-MD-321 (PARP1 low) cells in a plate were incubated with various concentration of cold AZD2281 (listed bottom of image) and 5 μCi of ^{18}F-AZD2281. Radioactivity was determined by γ emission.

conducted to test the use of microwave heating at short time intervals with no positive results. Attempts to use the less alkaline tetrabutyl ammonium bicarbonate (nBu$_4$NHCO$_3$) as a phase-transfer catalyst also resulted in decomposition of the starting materials, and <1% radiochemical yields (RCY) of **2.25^{18}F**.

The above results show that the chemoselective approach resulted in significantly higher yields of ^{18}F-labeled AZD2281 analogues and in much shorter time. The next question was therefore how the TCO/Tz ligand would affect target affinity. To assess this, a colorimetric assay (as described in 2.3.3) was employed to measure PARP1 activity (Figure 2.10). The published value for AZD2281 is 5 nm[31,32], identical to what we observed in our assay. Conventionally fluorinated **2.25^{19}F** had an IC$_{50}$ value of 5.2 ± 1.1 nm, consistent with the small side group. Compound 9 showed an IC$_{50}$ value of 8.4 ±

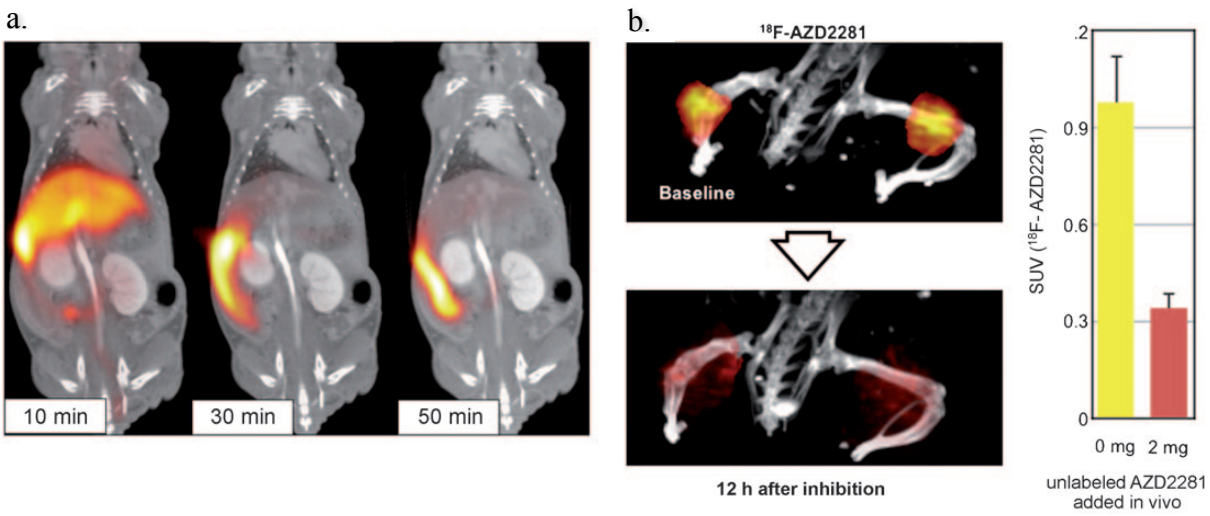

Figure 2.12[59]. PET imaging in a mouse using ^{18}F-AZD2281. a) PET imaging of ^{18}F-AZD2281 pharmacokinetics in a mouse. b) PET imaging and quantification of accumulation of 30 μCi ^{18}F-AZD2281 in MDA-MB-436 mouse flank tumors, and blocking of accumulation with 1 mg cold AZD2281 administered 12 hours prior (with bladder segmented out).

1.3nm, quite remarkable given the bulkier side chain. Cycloaddition fluorinated **2.18**^{19}**F** had an IC_{50} value of 17.9 ± 1.1 nm, still in the low double-digit nanomolar range and sufficient for imaging purposes following removal of excess **2.17** by a scavenger-assisted method (Figures 2.11 and 2.12, see Reiner et al., Angew. Chem. Int. Ed., 2011)[59].

2.7. Reflections and Follow-on Work

There were two important conclusions moving forward that were drawn from this technology development work: a) novel, targeted small molecule ligands can be modified

to be imaging probes without significantly altering their affinity, as long as the design is such that the modification is away from the part of the molecule that interacts with the target binding pocket, and b) in fact, it turned out that the click chemistry strategy is not the best for small-molecule imaging, especially *in vivo*, since the kinetics become complicated. For a time, the two-step click chemistry approach seemed as though it was the most suitable ^{18}F labeling platform, but the development of newer fluorination strategies have allowed for complementary approaches.

Follow-on intravital fluorescence imaging studies were done using AZD2281 directly conjugated to a fluorochrome, Bodipy FL[60,61]. Direct labeling improved the kinetics of PARP1 binding *in vivo*, allowing for experimental modeling of the pharmacokinetics of leakage into the tumor interstitium from the mouse vasculature, uptake into cells, and clearance of non-specific binding. At the same time, we expect the recently advances in efficient and fast synthesis of ^{18}F-Bodipy FL[62,63] to open doors for PET imaging using such small-molecule drug-^{18}F-Bodipy FL conjugates. Thus, as described in Chapter 3, we chose to use Bodipy FL to directly modify the drug Ibrutinib when exploring its use as a potential lymphoma companion imaging agent.

Finally, in ongoing work, the pharmacodynamic effects of AZD2281 are being studied by introducing a DNA damage reporter to ovarian and breast cancer cells, among others. The efficacy of the drug in causing cell death is being correlated against DNA damage, as well as PARP1 expression (via imaging drug uptake), and BRCA status. This may help discern how to best predict PARP1 inhibitor efficacy in patients.

Chapter 3.

Single-Cell Imaging of Bruton's Tyrosine Kinase Using an Irreversible Inhibitor

This work was previously published as:

Anna Turetsky*, Eunha Kim*, Rainer H. Kohler, Miles A. Miller, and Ralph Weissleder. Single cell imaging of Bruton's Tyrosine Kinase using an irreversible inhibitor. *Scientific Reports* 4, Article number: 4782 (2014). doi:10.1038/srep04782

*Equal contribution

Author Contributions

A.T., E.K. and R.W. designed the research, and A.T. and E.K. performed experiments. E.K. performed chemical synthesis and characterization. M.A.M. prepared transgenic cell lines and provided guidance with animal models. R.H.K. performed intravital imaging. A.T., E.K., R.H.K. and R.W. prepared figures. A.T., E.K. and R.W. wrote the manuscript. All authors reviewed and edited the manuscript.

A number of Bruton's tyrosine kinase (BTK) inhibitors are currently in development, yet it has been difficult to visualize BTK expression and pharmacological inhibition *in vivo* in real time. We synthesized a fluorescent, irreversible BTK binder based on the drug Ibrutinib and characterized its behavior in cells and *in vivo*. We show a 200 nM affinity of the imaging agent, high selectivity, and irreversible binding to its target following initial washout, resulting in

surprisingly high target-to-background ratios. In vivo, the imaging agent rapidly distributed to BTK expressing tumor cells, but also to BTK-positive tumor-associated host cells.

3.1. Introduction

Bruton's tyrosine kinase (BTK) is a non-receptor tyrosine kinase with restricted cellular expression largely limited to B lymphocytes, macrophages/monocytes, and certain cancer cells[64-67]. As a critical component of the B cell receptor (BCR) signaling network, BTK is crucial for B cell development[68,69] and acts in multiple anti-apoptotic signaling pathways, including the PI3K-AKT[70], STAT5[71] and NF-κB[72,73] pathways. BTK is thus intimately involved in regulating cell survival, proliferation, and differentiation. In human haematological malignancies, BTK is abundantly expressed and activated in malignant cells from patients with B-cell multiple myeloma[74], acute myeloid leukemia (AML)[20], chronic lymphocytic leukemia (CLL)[75], and non-Hodgkin's lymphoma (NHL)[17,76]. It is thus estimated that there are about 80,000 new BTK-positive haematologic malignancies in the US per year.

Several BTK inhibitors are under development and have shown remarkable efficacy in early clinical trials[19,21,22,77,78]. Ibrutinib (PCI-32765) is one example of a selective, irreversible BTK inhibitor, whose covalent binding results in long-lasting target occupancy, retaining inhibitory effect until new protein is synthesized[23,79]. The irreversible inhibitory effect of Ibrutinib is attributed to an electrophilic group on the molecule binding covalently to Cys 481 in the active site of BTK[80]. Most clinical trials to

date have relied on insensitive standardized Response Evaluation Criteria approaches, such as computed tomography (CT), to image drug effects, while a denaturing gel electrophoresis assay has been used when tissue is available in Ibrutinib trials[13,23]. In the latter assay, a fluorescent probe binds any unoccupied BTK in tissue biopsy or blood to produce a fluorescent band; the lighter the band, the more BTK is occupied by drug. Even in co-clinical trials using mouse models, drug efficacy is largely tested by volumetrics or cell counts, while little is known about the kinetics of drug distribution *in vivo*, accumulation across cell types, and their respective heterogeneities or drug effects. There is therefore a need for imaging tools to study BTK inhibitor distribution at the single cell level *in vivo*. Such tools could be valuable to better understand kinetics, selectivity, drug action, inform on dose ranging studies, and allow *in vitro* testing of harvested cells from patients. Furthermore, imaging would be especially useful in the development of next generation BTK inhibitors[78,81,82].

We hypothesized that an Ibrutinib-like scaffold could be converted into a companion diagnostic imaging agent by modification with a fluorescent tag while preserving irreversible target binding. The goal of the current study was to explore whether terminal modification of Ibrutinib could generate a BTK-selective imaging agent for *in vivo* use. Given the irreversible nature of target binding, one would expect improved target-to-background ratios following the clearance of unbound fractions. We indeed show remarkable target localization, specificity, and the ability to measure drug distribution and target inhibition *in vivo*. As more attention is paid to cell-to-cell heterogeneity in drug

response and its importance on efficacy, we believe this will be a useful tool to study BTK expression and inhibition[83].

3.2. Results

We sought to design a bright, fluorescent derivative of an irreversible BTK inhibitor that would preserve the selectivity of the parent drug. As such a model agent, Ibrutinib fits tightly into the ATP binding pocket of BTK, forms an irreversible bond with Cys481, and has a suitable modification point for fluorochrome attachment (PDB: 3GEN, Figure 3.1a). A Bodipy-FL modified Ibrutinib (Ibrutinib-BFL) was designed and synthesized de novo in seven steps (Figure 3.1b). Briefly, iodination of commercially available pyrazolopyrimidine compound with N-Iodosuccinimide, followed by Suzuki coupling of the product with 4-phenyloxybenzene boronic acid, resulted in compound **3.2**. Mitsunobu reaction of compound **3.2** with N-Boc-3-hydroxypiperidine resulted in compound **3.3**. After deprotection of the Boc protecting group in acidic conditions, the crude product was coupled with the linker (compound **3.5**) to introduce a Michael acceptor for the irreversible binding affinity. Coupling of the crude Boc-deprotected compound **3.6** with Bodipy-FL-NHS finalized the synthetic steps to produce Ibrutinib-BFL (**3.7**) at an overall yield of ~11%.

To confirm the effect of BFL modification on the inhibition efficacy of the drug, half-maximal inhibitory concentration (IC_{50}) of Ibrutinib and Ibrutinib-BFL were determined against purified BTK enzyme. Ibrutinib-BFL had an IC_{50} of ~200 nM, which is less potent than the parent drug (~2 nM IC_{50}; Figure 3.2). Although it may be possible to

a.

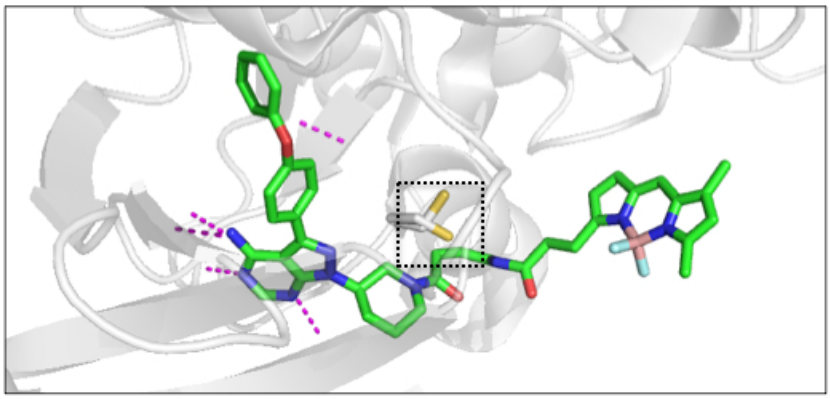

b.

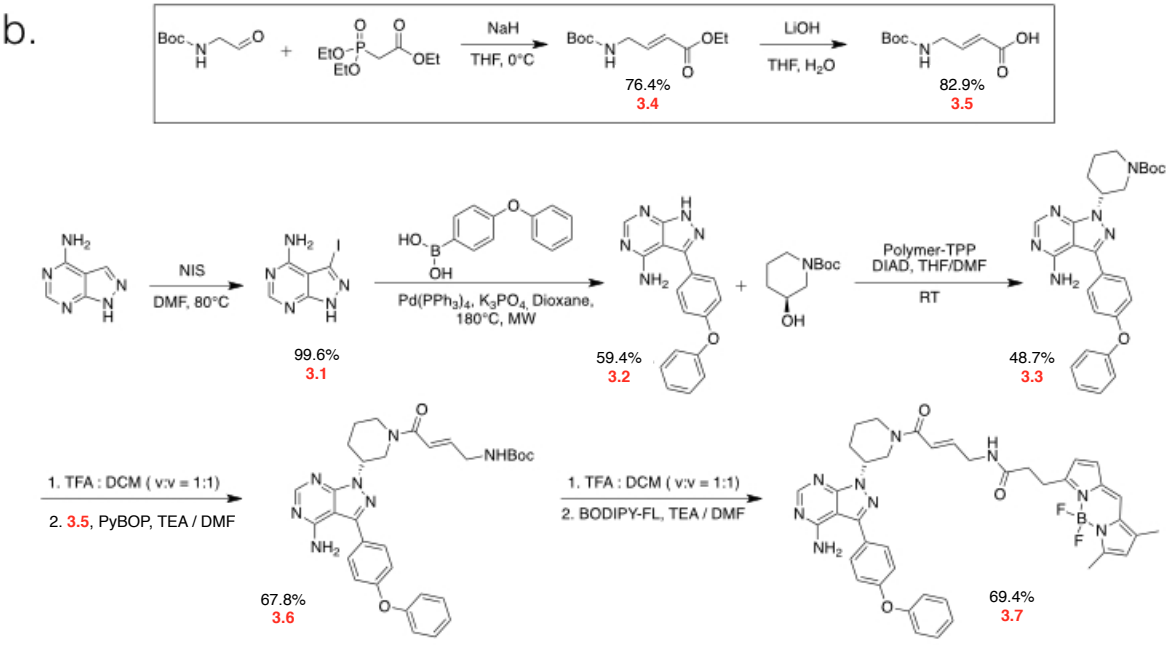

Figure 3.1. Structure and Synthetic Scheme of Ibrutinib-BFL (**3.7**). a. Crystal structure prediction of Ibrutinib-BFL (**3.7**) in its binding pocket of BTK. The reactive cysteine is highlighted in yellow inside the box. Hydrogen bonds are shown as purple dotted lines. 3D models were rendered using PyMol. b. Synthetic scheme of Ibrutinib-BFL (**3.7**).

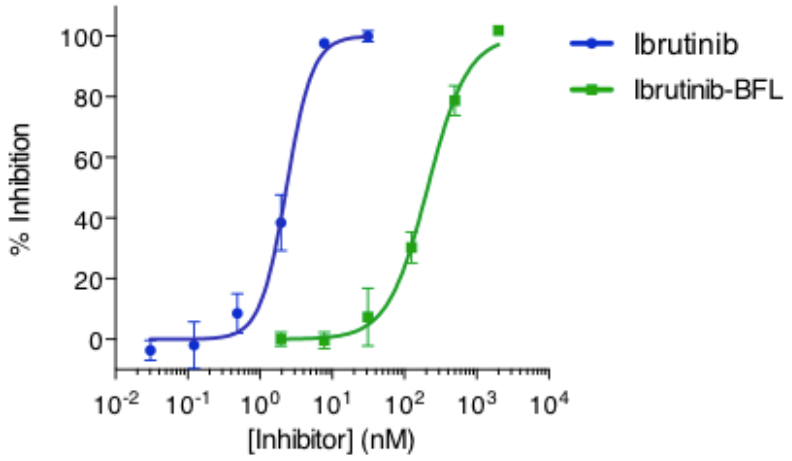

Compound	IC_{50}	R^2
Ibrutinib	2.3 nM*	0.98
Ibrutinib-BFL	210 nM	0.98

*Reported IC_{50} value : <0.5nM (ChemMedChem 2007, 2, 58-61)

Figure 3.2. Inhibition of BTK by Ibrutinib-BFL.

further optimize the affinity of Ibrutinib-BFL by testing various linkers, we found the current generation probe to be quite acceptable for imaging, as shown in subsequent experiments. We next determined whether Ibrutinib-BFL would bind to purified BTK *in vitro*, endogenous BTK in live cells, and ultimately *in vivo*. Purified BTK was incubated with varying concentrations of the imaging probe for one hour at room temperature, denatured at 70°C for 10 minutes and then processed for SDS-PAGE gel analysis. There was a clear dose-response increase of the fluorescent signal around 80 kDa (BTK molecular weight is 76 kDa), as well as at the bottom of the gel (unbound fraction of Ibrutinib-BFL) (Figure 3.3a). Additionally, binding could be blocked by pre-incubation with the parent compound and silver staining of the gel showed equal loading of BTK

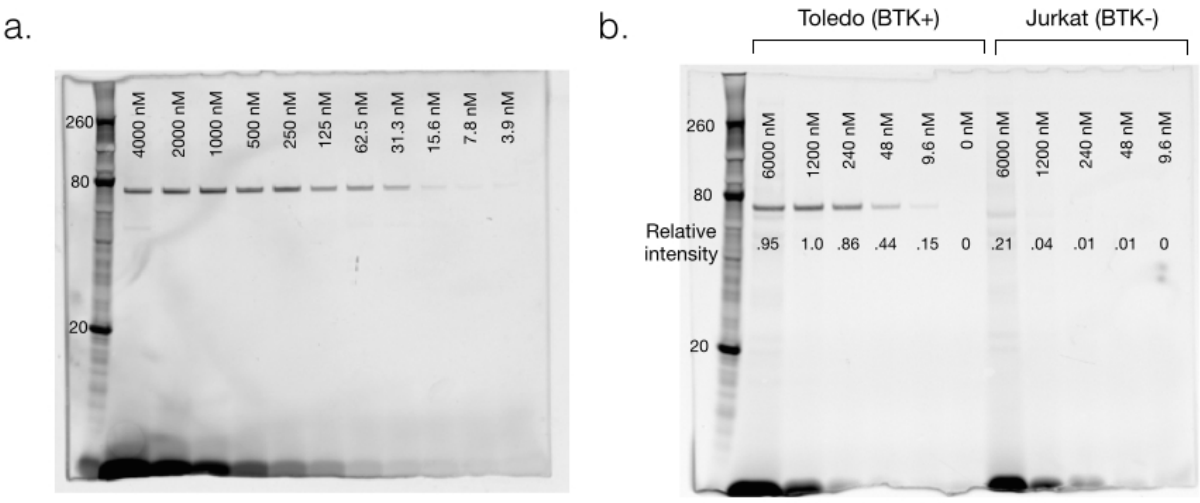

Figure 3.3. Characterization of Ibrutinib-BFL. a. Target binding. Denaturing gel electrophoresis of decreasing concentrations of Ibrutinib-BFL incubated with 0.1 µg purified BTK for one hour, imaged with 488 nm excitation / 520 nm emission. Note the dose dependent binding of Ibrutinib-BFL. Size marker on the far left. b. Denaturing gel electrophoresis of cell lysates following incubation of decreasing concentrations of Ibrutinib-BFL with Toledo (BTK+, left half of gel) or Jurkat (BTK-, right half of gel) cells at 37°C for two hours. Note the superb specificity of the probe.

protein (Figure 3.4a,c). These results clearly confirmed the covalent binding property of Ibrutinib-BFL toward purified BTK.

We next performed a similar experiment in lymphoma cells. We first determined BTK expression in several lymphoma cell lines (Daudi Burkitt's Lymphoma line, and DB, Toledo, and RC-K8 Diffuse Large B-Cell Lymphoma (DLBCL) lines) and one T-cell

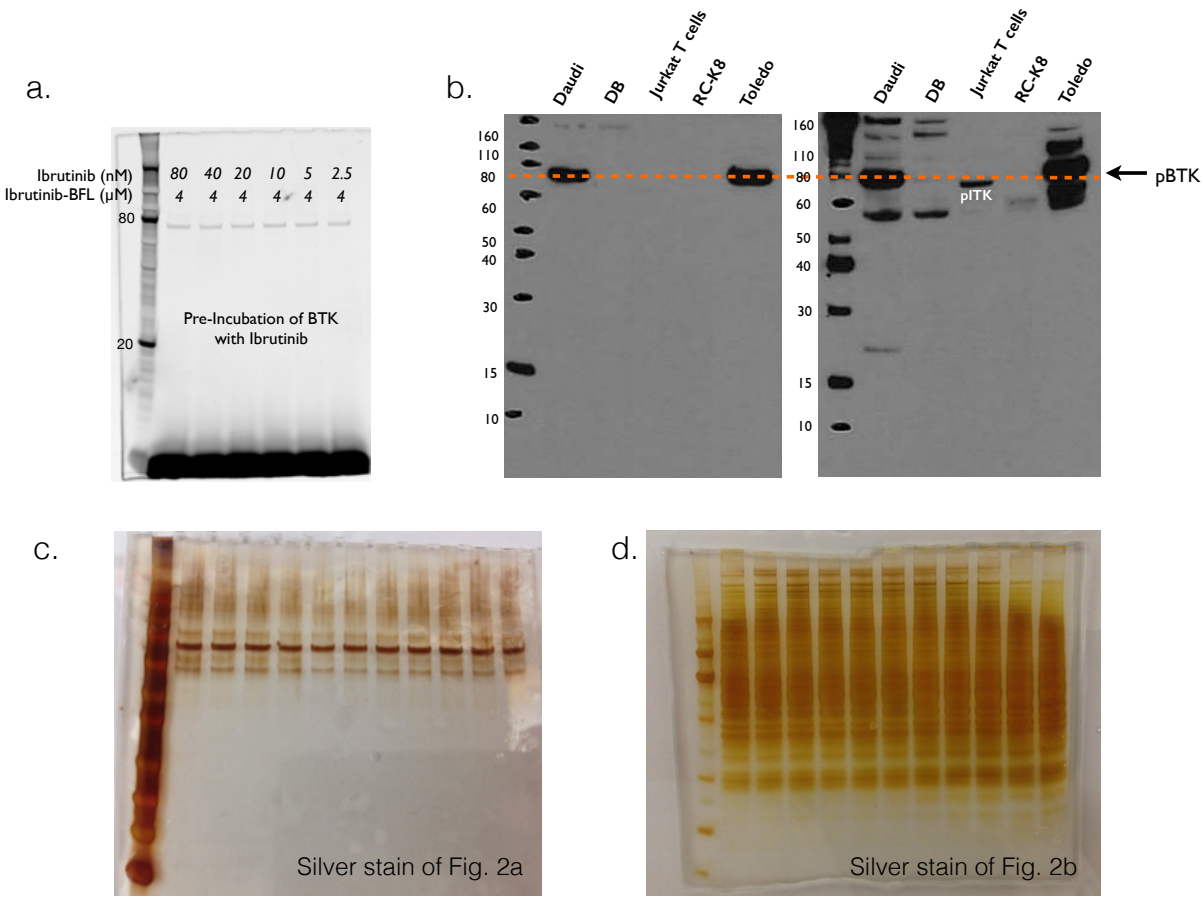

Figure 3.4. Additional gel electrophoresis experiments. a. Competition. After pre-incubation of BTK with concentrations of Ibrutinib ranging from 80 to 2.5 nM for one hour, Ibrutinib-BFL is blocked from binding to the BTK. Loading of Ibrutinib-BFL can be seen at the bottom of the gel. Extent of blocking seems to depend more on time than on concentration of Ibrutinib. b. Western blot of lymphoma cell lines, blotted with anti-BTK antibody (left) or stimulated and blotted with an antibody with cross-reactivity for pBTK and pITK, expressed in T cells. Orange dotted line indicates 80 kDa size marker; BTK is reported as having molecular weight of 76 kDa. c. Silver stain of purified BTK loading in Figure 3.3a. d. Silver stain of cell lysate loading in Figure 3.3b.

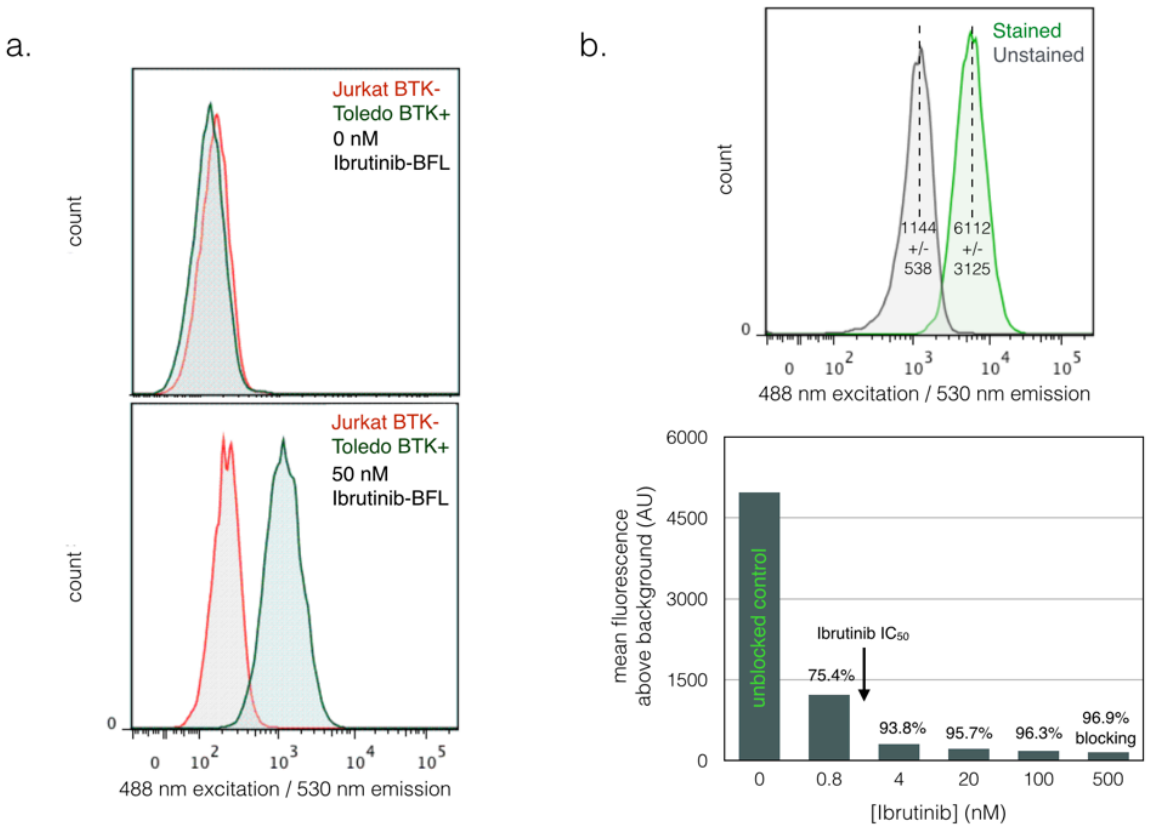

Figure 3.5. Optimization of BTK imaging and blocking experiment. a. Staining cells with Ibrutinib-BFL. Toledo and Jurkat cells were incubated with 0 nM (top) or 50 nM (bottom) Ibrutinib-BFL for two hours, followed by a 24-hour washout period in probe-free media. Ibrutinib-BFL only remains bound to Toledo cells, as shown by clear separation of cell populations by flow cytometry. b. Blocking with Ibrutinib. (Top) Difference in fluorescence between Toledo cells stained with 100 nM Ibrutinib-BFL and unstained Toledo cells. Unstained cells provide a benchmark for 100% blocking. (Bottom) Blocking of BTK staining by pre-incubation of Toledo cells with varying concentrations of unmodified Ibrutinib for 1.5 hours, followed by staining with Ibrutinib-BFL. Greater than 90% blocking at all concentrations above the Ibrutinib IC_{50} (~1 nM) confirms that Ibrutinib-BFL binds the same target as Ibrutinib.

leukemia line (Jurkat) by Western blot (Figure 3.4b). As expected, T cells did not express BTK. We found high BTK expression in Daudi and Toledo cell lines, and henceforth used Toledo as model BTK-positive cells and Jurkat as negative control cells. Toledo and Jurkat cells were incubated with different doses of Ibrutinib-BFL, and cell lysates were processed for SDS-PAGE and analyzed by fluorescent gel scanning. The imaging probe showed remarkable specificity, with binding observed only at a single band (Figure 3.3b). The specificity was further confirmed by the absence of a band in BTK-negative Jurkat cells, even at the highest concentration of probe (Figure 3.3b), as well as by silver staining of the gel (Figure 3.4d).

We next performed live cell imaging experiments using an imaging flow cytometry system. To prepare Toledo and Jurkat cells, we incubated them with 100 nM Ibrutinib-BFL for two hours, followed by washing. Figure 3.5 and Figure 3.6 summarize some of the results confirming target binding, specificity via blocking, and the ability to perform live cell imaging. To quantify co-localization between the imaging probe and BTK at the subcellular level, we created a stable transgenic cell line expressing a BTK-mCherry fusion protein in HT1080 human fibrosarcoma cells. *In vitro* cell experiments showed excellent co-localization and blocking ($r2 = 0.9851$; Figure 3.7).

We next performed *in vivo* experiments using three-color (blue: vasculature, green: Ibrutinib-BFL, red: BTK-mCherry-HT1080 cells) time-lapse intravital imaging. The intravascular half-life of Ibrutinib-BFL was ~10 minutes (Figure 3.8). Within an hour after systemic administration, there was extensive leakage of the compound into the

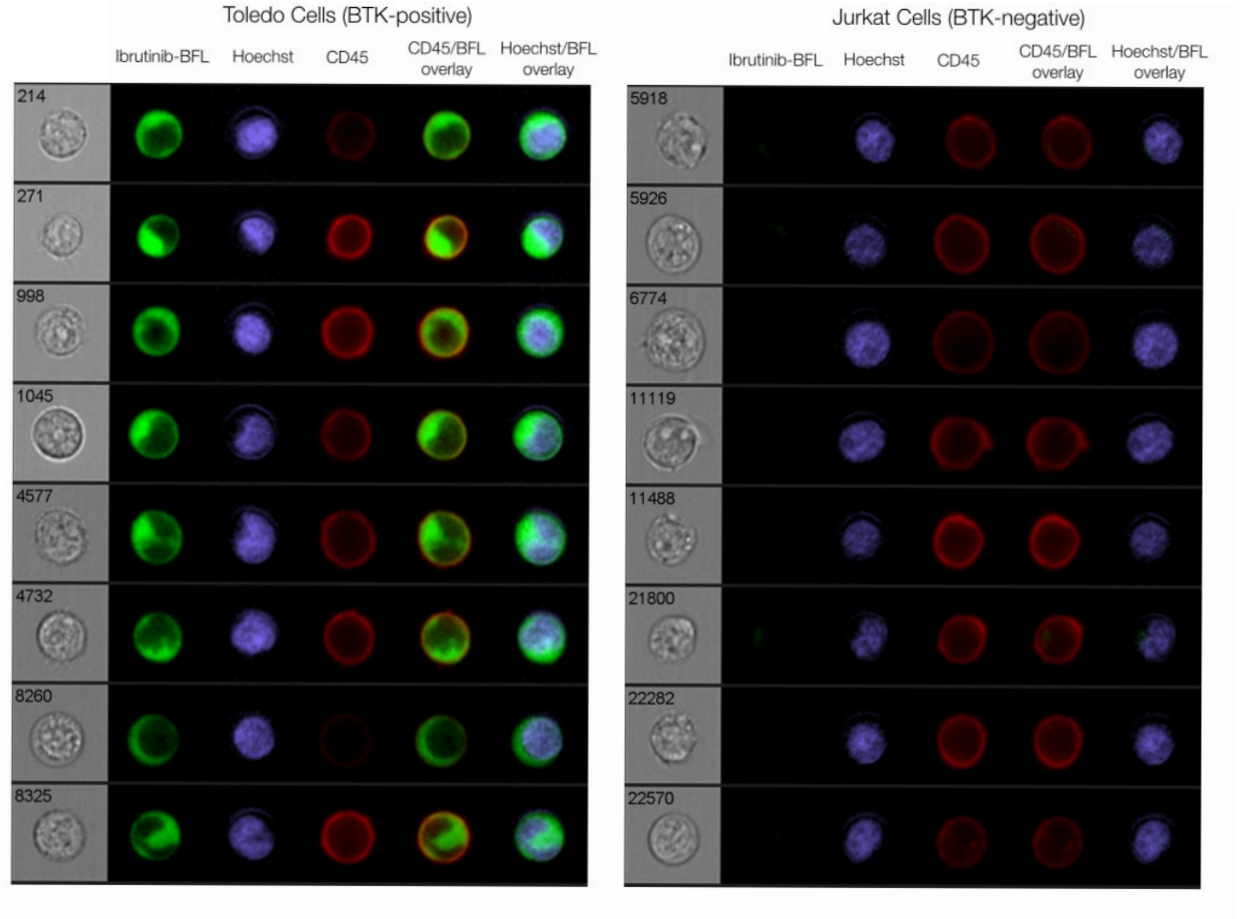

Figure 3.6. Cellular imaging of lymphoma cells. Representative images of Toledo (BTK-positive; left) and Jurkat (BTK-negative; right) cells incubated with 100 nM Ibrutinib-BFL at 37°C for 2 hours, then in probe-free media at 37°C for 24 hours. Cells were co-stained with Hoechst (nucleus) and CD45 (cell membrane) to show Ibrutinib-BFL localization in the cytoplasm of BTK-positive cells. Note the specificity. Images were obtained with an Amnis ImageStream flow cytometry system.

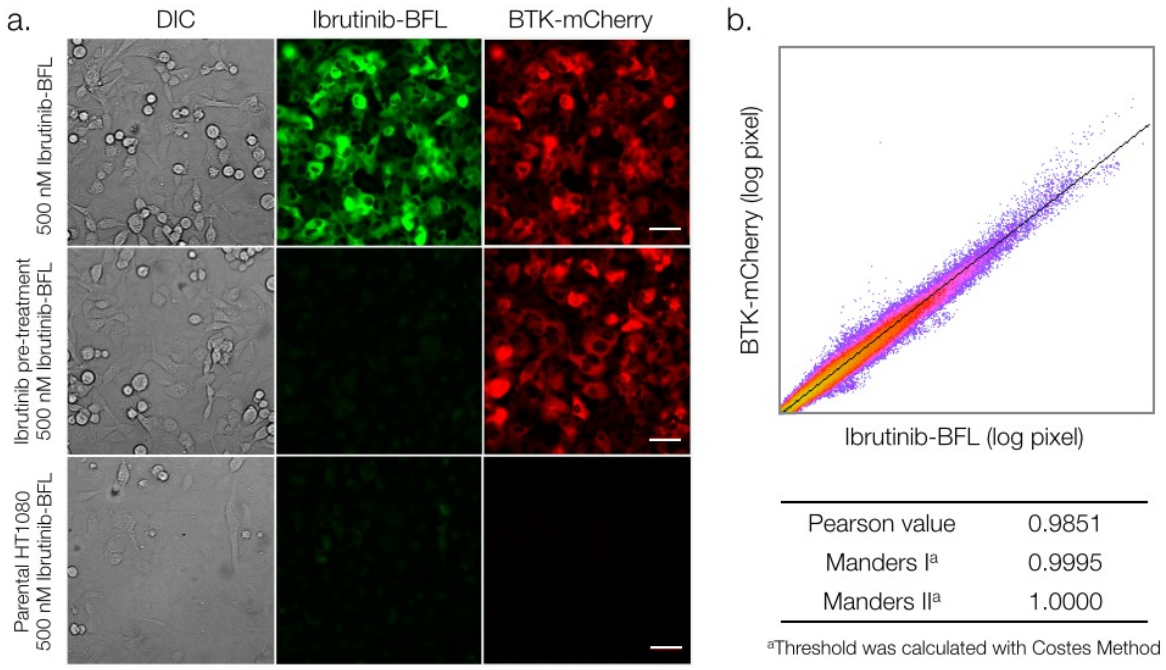

Figure 3.7. Imaging of adherent BTK-mCherry cells to determine co-localization with Ibrutinib-BFL. a. Imaging co-localization between 500 nM Ibrutinib-BFL (green) and HT1080 cells stably transfected with BTK-mCherry (red), following a 2-hour incubation with Ibrutinib-BFL and then a 24-hour incubation in probe-free media (top). Center: competitive inhibition with 1 μM Ibrutinib prior to Ibrutinib-BFL addition. Bottom: Ibrutinib-BFL incubated with non-BTK expressing parent HT1080 cells. b. Note the exquisite co-localization. Scale bar: 50 μm

tumor interstitium and other organs as shown by intravital imaging and in a biodistribution experiment (Figures 3.9, 3.10). At later time points, cellular uptake became apparent, presumably due to interstitial washout and/or intracellular accumulation. The ability to image in multiple channels allowed us to ask whether

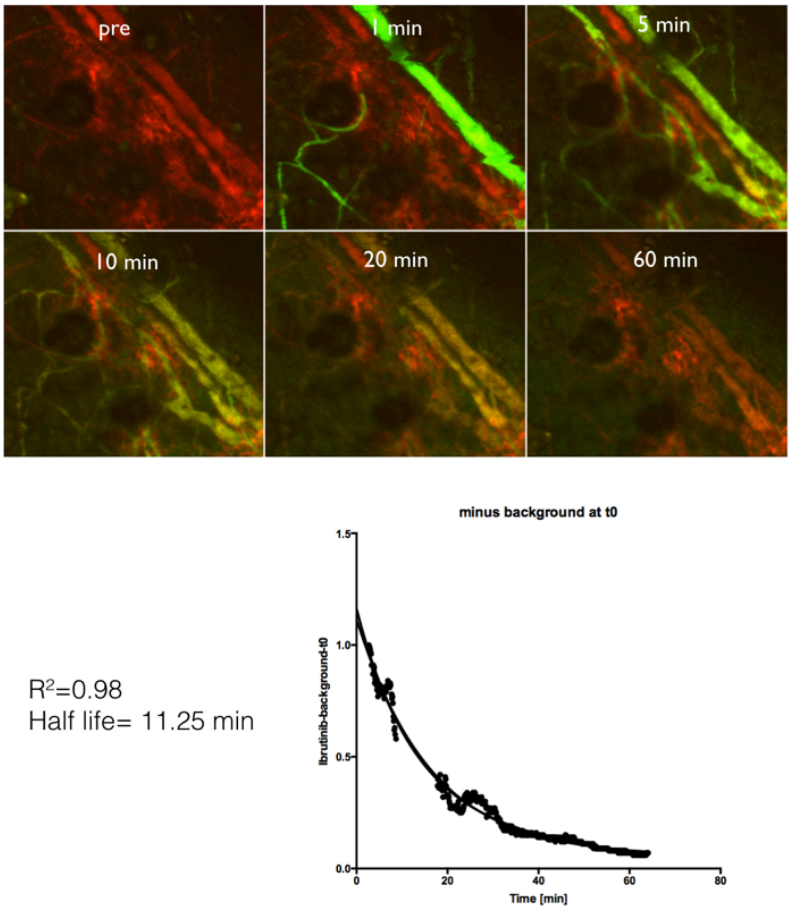

Figure 3.8. Vascular half-life. 75 nmol Ibrutinib-BFL was injected into the tail vein of C57BL/6 mice and serial imaging was performed in the mouse ear to determine vascular half- life of the IV injected probe. Imaging was performed using a customized Olympus IV110 laser- scanning microscope equipped with a 10x objective. a. Images of vasculature (red) and Ibrutinib-BFL (green) over 60 minutes post injection. b. Fluorescence in the mouse ear vasculature was used to calculate an initial blood half-life of ~11.25 minutes by fitting a one- phase exponential decay.

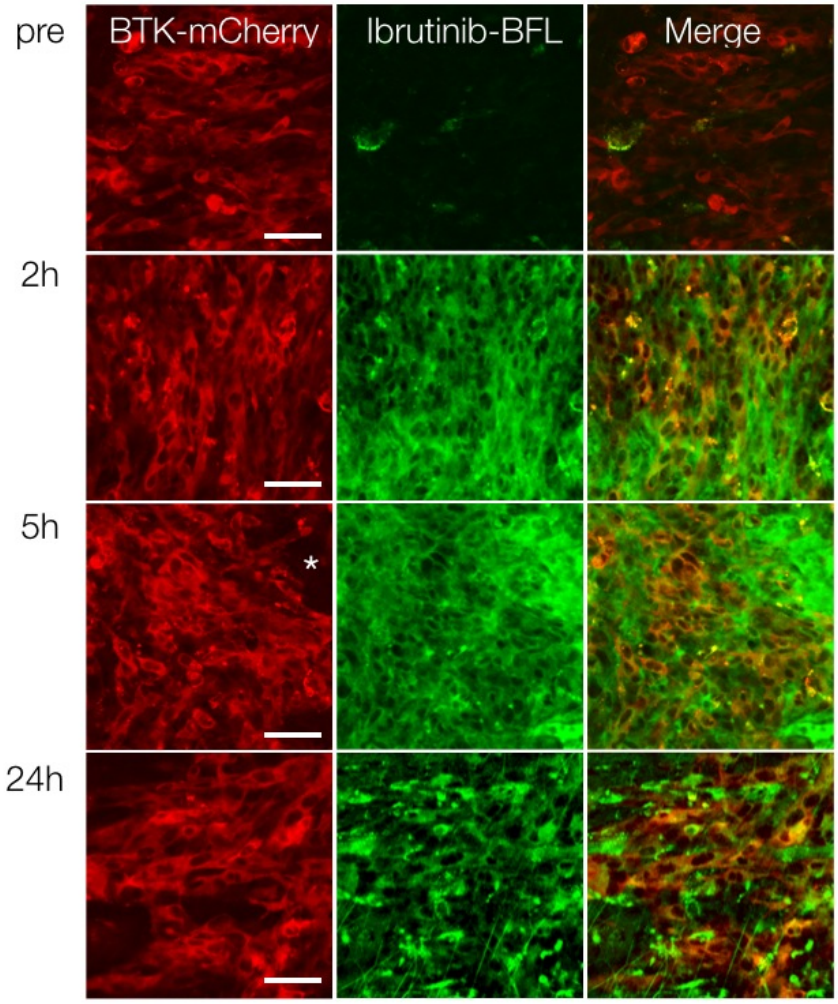

Figure 3.9. *In vivo* tumor imaging. Serial imaging before, and at 2, 5, and 24 hours after intravenous administration of Ibrutinib-BFL to a representative mouse harboring a BTK-positive HT1080 tumor (red; first column). Note extensive drug accumulation in all cells, persisting even at the 24-hour time point. * Indicates accumulation in non-tumor cells (see Figure 3.11). Scale bar: 50 μm

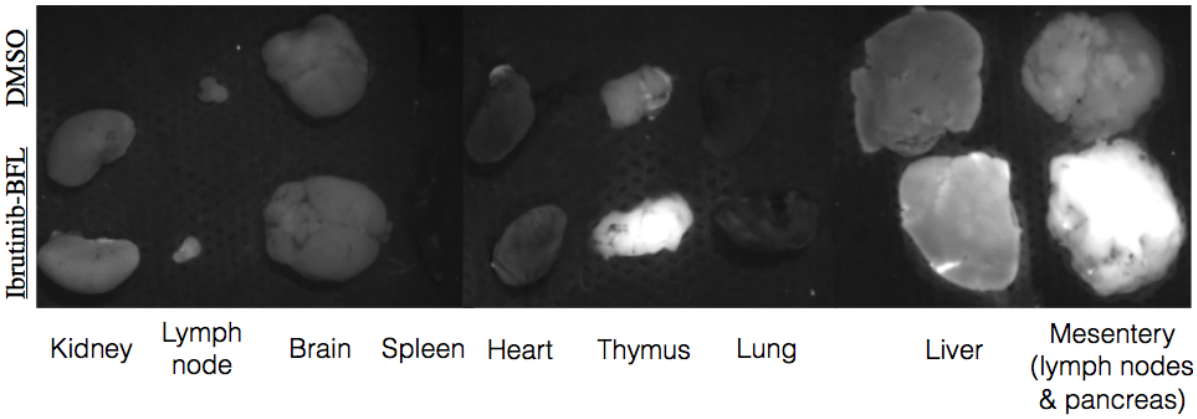

Figure 3.10. Ex vivo fluorescence imaging with DMSO control or Ibrutinib-BFL. (top and bottom, respectively, of individual organ figures).

Ibrutinib specifically localized in tumor cells. We show that greater than 99% of all BTK-mCherry-HT1080 cells had achieved therapeutic drug concentrations within one hour. This effective intracellular dose persisted for prolonged periods of time and the compound was still detectable inside cancer cells 24 hours after administration (Figure 3.9). Interestingly, there was also accumulation of Ibrutinib-BFL in non-tumor cells even at late time points. Given the exquisite specificity of the drug (see Figure 3.3), we hypothesized that these non-target cells also contain BTK. We thus performed correlative immunohistochemistry using anti-BTK antibody. Our data indicates that Ibrutinib-BTK also accumulates in tumor-associated macrophages and lymphocytes (Figure 3.11).

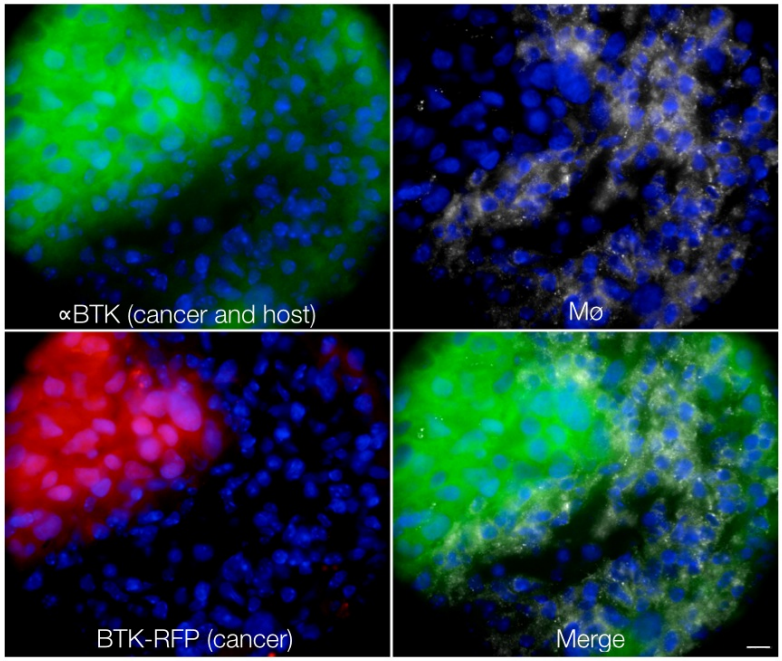

Figure 3.11. Histology. To corroborate intravital serial imaging, tumors were examined histologically. Anti-BTK staining showed BTK signal in HT-1080-BTK-mCherry cells as expected, but also in tumor-associated macrophages (white). These regions of drug accumulation correspond to those seen by intravital imaging (* in Figure 3.9). Scale bar: 10 μm

3.3. Materials and Methods

3.3.1. Synthesis and characterization of the probe

All reagents were obtained from commercial sources and used without further purification. Dry THF, MeOH, DCM, and DMF were obtained from Sigma-Aldrich (St.

Louis, MO). ^{1}H and ^{13}C NMR spectra were recorded at 23°C on a Bruker 400 MHz spectrometer. Recorded shifts are reported in parts per million (δ) and calibrated using residual undeuterated solvent. Data are represented as follows: chemical shift, multiplicity (s = singlet, d = doublet, t = triplet, q = quartet, p = pentet, m = multiplet, br = broad), coupling constant (J, Hz), and integration. NMR spectra are shown in Appendix B. LC-ESI-MS analysis and HPLC-purifications were performed on a Waters (Milford, MA) LC-MS system. For LC-ESI-MS analyses, a Waters XTerra® C_{18} 5 μm column was used. For preparative runs, an Atlantis® Prep T3 OBDTM 5 μm column was used [eluents 0.1% TFA (v/v) in water (solution A) and MeCN (solution B); gradient: 0-1.5 min, 5-100% B; 1.5-2.0 min, 100% B for analysis and 0-0.75 min, 5% B; 0.75-9.0 min, 5-100% B; 9.0-10.0 min, 100% B for prep.].

3-iodo-1H-pyrazolo[3,4-d]pyrimidin-4-amine (**3.1**).

A solution of 4-amino-1H-pyrazolo[3,4-d]pyrimidine (780 mg, 5.77 mmol) and N-Iodo-succinimide (2.02 g, 8.98 mmol) in DMF (6 mL) was stirred at 80°C overnight. Resulting brown solution was filtered and sticky solid was washed with water and cold ethanol. Resulting light yellow solid was dried *in vacuo* to give compound **3.1** (1.50 g, 99.6% yield). Crude product was used for the next reaction without further characterization.

3-(4-phenoxyphenyl)-1H-pyrazolo[3,4-d]pyrimidin-4-amine (**3.2**).

A solution of compound 1 (200 mg, 0.77 mmol), tetrakis-(triphenylphosphine) palladium (124 mg, 0.11 mmol), potassium phosphate tribasic (488 mg, 2.3 mmol), and

4-phenoxyphenylboronic acid (492 mg, 2.3 mmol) in 1,4-dioxane (2.5 mL) in a microwave vial was heated to 180°C for 10 minutes under microwave irradiation. Resulting reaction mixture was diluted with water and organic material was extracted with EA three times. Combined organic material was dried over Na_2SO_4 and concentrated *in vacuo*. Resulting yellow solution was dissolved with DCM and resulting turbid solution was filtered to give compound **3.2** as a white solid (138 mg, 59.4% yield). ^{1}H NMR (400 MHz, DMSO) δ 13.55 (s, 1H), 8.24 (s, 1H), 7.67 (d, J = 8.2 Hz, 2H), 7.44 (t, J = 7.8 Hz, 2H), 7.17 (m, 5H); ^{13}C NMR (101 MHz, DMSO) δ 158.0, 157.0, 156.3, 156.0, 155.7, 143.9, 130.1, 130.0, 128.4, 123.7, 119.0, 118.9, 96.9; LRMS (ESI) m/z calcd for $C_{17}H_{13}N_5O$ $[M+H]^+$ 304.12, found 304.14.

(R)-tert-butyl 3-(4-amino-3-(4-phenoxyphenyl)-1H-pyrazolo[3,4-d]pyrimidin-1-yl)piperidine-1-carboxylate (**3.3**).

A solution of compound **3.2** (57 mg, 0.19 mmol), (S)-3-hydroxy-N-Boc-piperidine (80 mg, 0.40 mmol), DIAD (150 µL, 0.764 mmol), and polymer-TPP (0.5 g, 1.6 mmol) in THF (4 mL) was stirred at ambient temperature overnight. After reaction completion, polymer-TPP was removed by filtration, filtrate was concentrated *in vacuo* and purified with silica gel column chromatography (EA : Hex = 0 : 100 to EA only) to give compound **3.3** (45 mg, 48.7% yield) as a clear oil. ^{1}H NMR (400 MHz, $CDCl_3$) δ 8.37 (s, 1H), 7.65 (d, J = 7.5 Hz, 2H), 7.38 (m, 2H), 7.19 – 7.12 (m, 3H), 7.08 (d, J = 8.6 Hz, 2H), 5.49 (s, 2H), 4.84 (dq, J = 10.4, 5.1, 4.3 Hz, 1H), 4.35 – 4.23 (m, 1H), 4.16 – 4.06 (m, 1H), 3.46 (t, J = 11.5 Hz, 1H), 2.88 (td, J = 12.3, 2.8 Hz, 1H), 2.34 – 2.14 (m, 2H), 1.96 –

1.85 (m, 1H), 1.78 – 1.65 (m, 1H), 1.45 (s, 9H). ^{13}C NMR (101 MHz, $CDCl_3$) δ 158.5, 157.8, 156.4, 155.7, 154.6, 154.2, 143.6, 130.0, 129.9, 127.9, 124.0, 119.5, 119.1, 98.6, 79.8, 52.9, 48.2, 44.0, 30.2, 28.4, 24.5.; LRMS (ESI) m/z calcd for $C_{27}H_{30}N_6O_3$ $[M+H]^+$ 487.24, found 487.25.

(E)-ethyl 4-((tert-butoxycarbonyl)amino)but-2-enoate (**3.4**).

To a solution of NaH (50 mg, 1.26 mmol) in THF (4 mL), stirred at 0°C, triethylphosphonoacetate (374 μL) was added dropwise. After warming up to ambient temperature, solution of N-Boc-2-aminoacetaldehyde (100 mg, 0.63 mmol) in THF (1 mL) was added. Reaction mixture was stirred at ambient temperature. After reaction completion, reaction mixture was diluted with water and organic material was extracted with EA three times. Combined organic material was dried over Na_2SO_4 and concentrated *in vacuo*. Reaction mixture was purified with silica gel column chromatography (EA : Hex = 0 : 100 to EA only) to give compound **3.4** (110 mg, 76.4% yield) as a clear oil. ^{1}H NMR (400 MHz, $CDCl_3$) δ 6.88 (dt, J = 15.7, 4.9 Hz, 1H), 5.91 (dt, J = 15.6, 1.8 Hz, 1H), 4.81 (s, 1H), 4.16 (q, J = 7.2 Hz, 2H), 3.89 (s, 2H), 1.42 (s, 9H), 1.26 (t, J = 7.1 Hz, 3H); ^{13}C NMR (101 MHz, $CDCl_3$) δ 166.2, 155.7, 144.9, 121.4, 79.9, 60.5, 41.4, 28.4, 14.3; LRMS (ESI) m/z calcd for $C_{11}H_{19}NO_4$ $[M+H]^+$ 230.13, found 230.15.

(E)-4-((tert-butoxycarbonyl)amino)but-2-enoic acid (**3.5**).

A solution of compound **3.4** (110 mg, 0.48 mmol) and LiOH (168 mg, 2.4 mmol) in THF (3 mL) and water (2 mL) was stirred at ambient temperature overnight. THF was

evaporated and resulting yellow aqueous solution was acidified with 1N HCl to pH 3. Organic material was extracted with DCM three times. Combined organic material was dried over Na_2SO_4 and concentrated *in vacuo*. Reaction mixture was purified with silica gel column chromatography (MeOH : DCM = 0 : 100 to 1 : 10) to give compound **3.5** (80 mg, 82.9% yield) as a white solid. ^{1}H NMR (400 MHz, $CDCl_3$) δ 6.93 (dt, J = 15.9, 4.7 Hz, 1H), 5.87 (dt, J = 15.7, 1.9 Hz, 1H), 4.73 (s, 1H), 3.88 (s, 2H), 1.39 (s, 9H); ^{13}C NMR (101 MHz, $CDCl_3$) δ 170.9, 155.8, 147.4, 120.8, 80.2, 41.5, 28.5; LRMS (ESI) m/z calcd for $C_9H_{15}NO_4$ $[M+H]^+$ 202.10, found 202.10.

(R,E)-tert-butyl (4-(3-(4-amino-3-(4-phenoxyphenyl)-1H-pyrazolo[3,4-d]pyrimidin-1-yl)piperidin-1-yl)-4-oxobut-2-en-1-yl)carbamate (**3.6**).

A solution of compound **3.3** (100 mg, 0.21 mmol) in 2 mL of TFA and DCM mixture (1 : 3 = v : v) was stirred at ambient temperature. After 30 minutes stirring, reaction mixture was concentrated *in vacuo*. After azeotropic distillation with DCM and ACN three times, crude product was concentrated *in vacuo*. Then crude product was diluted with DMF (2.1 mL) to make 0.1 M solution. 650 µL of crude product solution in DMF was mixed with compound **3.5** (16 mg, 0.078 mmol), HBTU (37 mg, 0.097 mmol), and TEA (45 µL) in DMF (200 µL) and reaction mixture was stirred at ambient temperature. After one hour, reaction mixture was directly loaded onto a C18 reverse phase column for purification (Water : ACN w/ 0.1% Formic acid = 95 : 5 to 0 : 100) to give compound **3.6** (25 mg, 67.8% yield) as a sticky solid. ^{1}H NMR (400 MHz, $CDCl_3$) δ 8.36 (d, 1H), 7.72 – 7.57 (m, 3H), 7.38 (t, J = 7.8 Hz, 2H), 7.21 – 7.02 (m, 5H), 6.65 (t, J = 9.8 Hz, 1H), 5.75

(br s, 2H), 4.94 – 4.74 (m, 1H), 4.74 – 4.60 (m, 1H), 4.52 (d, J = 13.0 Hz, 0.5H), 4.10 – 3.97 (m, 0.5H), 3.86 (d, J = 13.2 Hz, 0.5H), 3.66 (dd, J = 13.2, 10.4 Hz, 0.5H), 3.33 (t, J = 12.0 Hz, 0.5H), 3.26 – 2.95 (m, 2H), 2.85 – 2.66 (m, 0.5H), 2.50 – 2.15 (m, 2H), 2.06 – 1.86 (m, 1H), 1.80 – 1.58 (m, 1H), 1.46 (s, 9H); LRMS (ESI) m/z calcd for $C_{31}H_{35}N_7O_4$ $[M+H]^+$ 570.28, found 570.20.

(R,E)-3-(3-((4-(3-(4-amino-3-(4-phenoxyphenyl)-1H-pyrazolo[3,4-d]pyrimidin-1-yl)piperidin-1-yl)-4-oxobut-2-en-1-yl)amino)-3-oxopropyl)-5,5-difluoro-7,9-dimethyl-5H-dipyrrolo[1,2-c:2',1'-f][1,3,2]diazaborinin-4-ium-5-uide (**3.7**). A solution of compound **3.6** (5 mg, 0.009 mmol) in 2 mL of TFA and DCM mixture (1 : 3 = v : v) was stirred at ambient temperature. After 30 minutes stirring, reaction mixture was concentrated *in vacuo*. After azeotropic distillation with DCM and ACN for three times, crude product was concentrated *in vacuo*. Then crude product was diluted with DMF (880 µL) to make 0.1 M solution. 390 µL of crude product solution in DMF was mixed with BODIPY-FL-NHS (1 mg, 0.0026 mmol) and TEA (2 µL, 0.013 mmol) in DMSO (1 mL) and the resulting reaction mixture was stirred at ambient temperature for one hour and was then purified using standard HPLC techniques to give compound **3.7** (1.1 mg, 57.6% yield) as a greenish solid. ^{1}H NMR (400 MHz, $CDCl_3$) δ 8.45 (br s, 1H), 8.23 (d, J = 9.9 Hz, 1H), 7.63 (dd, J = 32.3, 8.2 Hz, 2H), 7.48 - 7.21 (m, 3H), 7.21 - 7.06 (m, 2H), 7.04 - 6.86 (m, 2H), 6.66 (dt, J = 4.9, 4.9, 15.3 Hz, 1H), 6.52 - 6.28 (m, 2H), 6.18 (d, J = 22.1 Hz, 1H), 4.56 (d, J = 12.3 Hz, 1H), 4.24 (dd, J = 13.3, 39.5 Hz, 2H), 4.03 - 3.78 (m, 3H), 3.54 - 3.44 (m, 1H), 3.27 - 3.07 (m, 3H), 2.74 - 2.62 (m, 1H), 2.60 - 2.30 (m, 5H),

2.29 - 2.17 (m, 3H), 2.09 - 1.99 (m, 1H), 1.74 - 1.60 (m, 1H); LRMS (ESI) m/z calcd for $C_{40}H_{40}BF_2N_9O_3$ $[M+H]^+$ 744.34, found 744.30.

3.3.2. Kinase inhibition assay

The Z'-LYTE Kinase Assay Kit - Tyrosine 1 Peptide (Invitrogen, Grand Island, NY, USA) was used according to the manufacturer's instructions and tested against purified BTK enzyme (Promega, Madison, WI, USA) and ATP. The assay was then performed in the presence of inhibitors Ibrutinib and Ibrutinib-BFL using 1 μg/mL BTK and 50 μM ATP, without pre-incubation of inhibitors with the enzyme. Concentrations of Ibrutinib were 4-fold serial dilutions ranging from 33 nM to 0.01 nM, while concentrations of Ibrutinib-BFL were 4-fold serial dilutions ranging from 8000 nM to 1.95 nM. Negative control samples did not contain ATP, and positive controls contained the pre-phosphorylated peptide included in the assay kit. Kinase reaction buffer contained 0.67% DMSO. Experiments were performed in quadruplicate in 384-well plates. Fluorescence resulting from peptide phosphorylation was measured on a TECAN plate reader system (Zurich, Switzerland). Background fluorescence from the fluorescent probe was subtracted from the final measurements. Prism (GraphPad Software, La Jolla, CA, USA) was used to plot dose-response curves and to calculate IC_{50} values.

3.3.3. Cell lines

The diffuse large B-cell lymphoma (DLBCL) cell lines DB and Toledo were generously provided by Dr. Anthony Letai (Dana Farber Cancer Institute, Boston, MA,

USA). The RC-K8 DLBCL cell line was a generous gift from Dr. Thomas Gilmore (Boston University, Boston, MA, USA). Daudi Burkitt's lymphoma cell line and Jurkat T-cell leukemia line were from ATCC (Manassas, VA, USA). Lymphoma cell lines were cultured in RPMI 1640 media supplemented with 10% fetal bovine serum at 37°C and 5% CO_2. To test the BTK inhibitor in adherent cells, we used HT1080 human fibrosarcoma cells, which have previously been shown to be ideal for intravital imaging studies[84]. HT1080 cells were from ATCC, grown in DMEM supplemented with 10% fetal bovine serum and 2% glutamine-penicillin-streptomycin at 37°C and 5% CO_2. HT1080-BTK-mCherry cells were prepared by viral infection of HT1080 cells. Virus generated from pMSCVpuro-mCherry-BTK retroviral vector[85] was a generous gift from Dr. Hidde Ploegh (Massachusetts Institute of Technology, Cambridge, MA, USA). Viral supernatant was added directly to HT1080 cells for 48 hours, and BTK-mCherry-expressing cells were then selected with RPMI media containing 2 μg/mL puromycin for 96 hours. Following selection, HT1080-BTK-mCherry cells were cultured under the same conditions as the original HT1080 cells.

3.3.4. Western blot

Cell lysates were prepared from B-cell lymphoma (Daudi, DB, Toledo, RC-K8) and control T cell (Jurkat) lines by lysis in RIPA buffer, and total protein concentrations were measured using the TECAN plate reader after performing the Pierce BCA protein assay (Thermo Fisher Scientific) according to the manufacturer's instructions in a 96-well plate format. 17.5 μg of each cell line was diluted with H2O to 20 μL, and samples were then

combined with NuPAGE LDS sample buffer and NuPAGE reducing agent (Invitrogen) for final 25% and 10% concentrations, respectively, and samples were heated to 70°C for 10 minutes. Samples were loaded onto a 12-well NuPAGE Novex 4-12% Bis-Tris Gel (Invitrogen). Using Novex Sharp Pre-stained Protein Standard (Invitrogen) as a size marker, the gel was run in MES buffer at 200 V for 35 minutes. An iBlot blotting system (Invitrogen) was used for transfer to a PVDF membrane. Membranes were blocked in Pierce SuperBlock blocking buffer (Thermo Fisher Scientific) for one hour, then stained overnight at 4°C in 1:500 mouse anti-human-BTK antibody (Clone 53/BTK, BD, Franklin Lakes, NJ, USA) in TBST buffer containing 10% SuperBlock. Blots were then washed in TBST three times for 20 minutes and incubated in 1:1000 Peroxidase Affinipure goat anti-mouse IgG (Jackson ImmunoResearch Laboratories, West Grove, PA, USA) in TBST buffer containing 10% SuperBlock for one hour at room temperature. After washing three times for 20 minutes each, blots were incubated with SuperSignal West Pico Chemiluminescent Substrate (Thermo Fisher Scientific), exposed on film, and developed with a Kodak X-OMAT 2000A processor (Rochester, NY, USA).

3.3.5. Gel electrophoresis

To test the covalent binding of Ibrutinib-BFL to BTK, 0.1 µg (1 µL) purified BTK was combined with 0.4 µL Ibrutinib-BFL (prepared in advance in 2-fold dilutions ranging from 200 µM to 0.19 µM, 33% DMSO in PBS) and 18.6 µL PBS, and incubated in the dark at room temperature for one hour. In the second experiment, Toledo and Jurkat cells (2.2×10^6 per well in culture media) were incubated in growth media containing 5-fold

serial dilutions of Ibrutinib-BFL ranging from 6 μM to 9.6 nM in final 2% DMSO at 37°C for two hours. Control samples were incubated in growth media containing 2% DMSO. Cells were washed once with ice cold PBS, then lysed in 150 μL 1X RIPA buffer (Cell Signaling Technology, Beverly, MA, USA) containing protease inhibitors. To the purified enzyme samples or cell lysates, NuPAGE LDS sample buffer and NuPAGE reducing agent (Invitrogen) were added for final 25% and 10% concentrations, respectively, and samples were heated to 70°C for 10-12 minutes in a Mastercycler thermal cycler (Eppendorf, Hamburg, Germany). 25 μL per lane was loaded into 12-well NuPAGE Novex 4-12% Bis-Tris gels (Invitrogen). Using 10 μL of Novex Sharp Pre-stained Protein Standard (Invitrogen) as a size marker, the gels were run in NuPAGE MES SDS running buffer (Invitrogen) at 200 V for 35 minutes in the XCell SureLock Mini-Electrophoresis system (Invitrogen). The gels were removed from the cassette and imaged using a Typhoon 9410 fluorescence scanner (GE Healthcare, Pittsburgh, PA, USA) using 488 nm excitation and a 520 nm emission filter. To show total protein loading, gels were silver-stained using the Pierce Silver Stain for Mass Spectrometry kit (Thermo Fisher Scientific, Rockford, IL, USA).

3.3.6. Flow cytometry

Jurkat and Toledo cells were incubated in growth media containing 5-fold serial dilutions of Ibrutinib-BFL, ranging from 8 μM to 12.8 nM in final 2% DMSO at 37°C for two hours. Control samples contained cells in media containing 2% DMSO. Cells were centrifuged and resuspended in growth media at time-points of 1, 14, 24, and 72 hours. At

each time-point, $5x10^5$ cells were harvested for analysis by flow cytometry, and the remaining cells were cultured at 37°C. 24 hours was found to be the optimal washout time-point and used in subsequent experiments. A separate, blocking experiment was performed in which Toledo cells were first incubated in growth media containing 5-fold serial dilutions of unmodified Ibrutinib (Cellagen Technology, San Diego, CA, USA) ranging from 500 nM to 0.8 nM in final 2% DMSO at 37°C for 1.5 hours. Without washout, Ibrutinib-BFL was then added to each well for 50 nM final concentration and 4% final DMSO, and incubated at 37°C for two hours. A positive control sample contained no Ibrutinib, while a negative control for autofluorescence contained no Ibrutinib-BFL. After two hours, Ibrutinib-BFL-containing media was removed by centrifugation, and cells were incubated in fresh media at 37°C for 24 hours prior to analysis by flow cytometry. Cells collected for flow cytometry were centrifuged and resuspended in 200 μL PBS containing 0.5% BSA, and filtered through 35 μM Cell Strainer tubes (BD). Flow cytometry in the FITC channel was performed on an LSRII flow cytometer (BD) and subsequent data analysis was done using FlowJo software (TreeStar, Ashland, OR, USA).

3.3.7. Imaging of non-adherent lymphoma cells by flow cytometry

Jurkat and Toledo cells were single- or triple-stained with the following, followed by washing: Ibrutinib-BFL (2 hours in growth media, 37°C), Hoechst 33342 nuclear dye (Invitrogen), or APC-conjugated anti-human-CD45 antibody (Clone HI30, BioLegend, San Diego, CA, USA)(both 30 minutes in PBS containing 2% BSA, 4°C). Stained cells

were transferred to Clear-view Snap-Cap microtubes (Sigma-Aldich) for Amnis ImageStreamX Mark II imaging flow cytometry (Amnis Corporation, Seattle, WA, USA). Single-stained samples were used to create a compensation table, then 30,000 images from each triple-stained sample were collected using excitation lasers 405-nm, 488-nm, 592-nm, and bright-field excitation, and 430-550-nm (Ch7), 480-560-nm (Ch2), 640-745-nm (Ch11), and 430-480 (Ch1) emission filters. Representative images were manually selected from this data set.

3.3.8. Imaging of adherent cells by microscopy

HT1080-BTK-mCherry cells were seeded into a 96-well plate at 20,000 cells per well and allowed to grow to confluence overnight. Cells were incubated in growth media containing 1 μM Ibrutinib in final 0.1% DMSO, or control 0.1% DMSO, at 37°C for 1.5 hours. Without washout, a 50X stock of Ibrutinib-BFL in 5% DMSO was added for a final concentration of 500 nM. Control wells contained equivalent DMSO without Ibrutinib-BFL. Cells were incubated for one hour at 37°C and then washed once with media for five minutes. The media was then replaced and cells were incubated overnight at 37°C. The live cells were subsequently imaged on the DeltaVision imaging system (Applied Precision, a GE Healthcare Company). Images were processed with Fiji software, an open-source version of ImageJ.

3.3.9. *In vivo* tumor imaging

Nu/nu mice were implanted with $2x10^6$ HT1080-BTK-mCherry cells into a dorsal skinfold window chamber (APJ Trading Company, Ventura, CA, USA) according to established protocols[7] and according with guidelines from the Institutional Subcommittee on Research Animal Care. Tumors were allowed to grow and vascularize for two weeks. 75 nmol Ibrutinib-BFL in 150 μL solution containing DMAc and solutol was injected via tail vein as reported previously[61]. Mice were anesthetized with 2% isoflurane in 2 L/min oxygen. Time-lapse microscopy was performed for two hours using a customized Olympus FV1000 confocal/multiphoton microscope equipped with a 20X objective (both Olympus America, Chelmsford, MA, USA). In addition, tumors were imaged before injection, and at 2, 5, and 24 hours post-injection. Images were processed with Fiji software.

3.3.10. Histology

HT1080-BTK-mCherry tumors were harvested from nu/nu mice and embedded in O.C.T. compound (Sakura Finetek, Torrance, CA, USA). Serial 6 μm-thick frozen sections were prepared for histological analysis. Fluorescence immunohistochemistry staining was performed using Mac-3 (clone: M3/84, BD Biosciences, San Jose, CA, USA) and BTK (clone: D3H5, Cell Signaling Technology), followed by Alexa Fluor 647 goat anti-rat IgG and Alexa Fluor 488 goat anti-rabbit IgG (both Invitrogen) secondary antibodies, respectively. Images were captured using a BX63 fluorescence microscope

(Olympus America) equipped with a Neo sCMOS camera (Andor Technology, Belfast, UK) and processed with Fiji software.

3.3.11. *Ex vivo* fluorescence imaging

C57BL/6 mice were IV injected with 150 μL of Ibrutinib-BFL solution [7.5 μL of 10 mM Ibrutinib-BFL solution in DMSO was diluted with 142.5 μL of DMAc:solutol:PBS (v:v:v = 1:1:7.5) mixture (final concentration = 50 μM)] or DMSO control. One hour after injection, animals are euthanized and the organs were collected. *Ex vivo* fluorescence images of organs were obtained using an OV110 system (Olympus America) with 488 nm excitation.

3.4. Discussion

Inhibition of BTK is emerging as a promising target for B-cell malignancies, other cancers with BTK over-expression, and certain autoimmune diseases where BTK is involved. Ibrutinib, an irreversible inhibitor, is approved for treatment of mantle cell lymphoma and chronic lymphocytic leukemia, and is currently undergoing late-stage efficacy studies in patients with various B-cell malignancies. Based on its covalent target binding, we hypothesized that the molecule could serve as a companion imaging agent. Here we show that this is indeed the case. Ibrutinib-BFL co-localized with BTK in BTK-positive malignant cells and had low background accumulation in non-BTK cells, including those expressing structurally related interleukin-2-inducible T-cell kinase (ITK), which is expressed in T cells and Jurkat cells (see Figure 3.4). The companion

imaging drug, Ibrutinib-BFL, also showed a predictable dose response curve, could be competitively inhibited, allowed drug concentrations to be quantitated *in vivo*, and enabled mapping of drug distributions at the single cell level. As such, we believe that Ibrutinib-BFL could have several applications, including use as a companion diagnostic for flow cytometry in haematologic malignancies, as an imaging agent to localize and map BTK-positive tumors, as a method to track subcellular localization of endogenous BTK, and as a tool to measure pharmacokinetics and pharmacodynamics in experimental settings during development of novel BTK-pathway inhibitors.

BTK is a cytoplasmic tyrosine kinase belonging to the Tec family. It is expressed in the B-cell lineage, plays a pivotal role in signaling and development, and is highly active in several haematological malignancies[18,86]. Some previous BTK imaging has been done with fluorescent protein tags (BTK-GFP and BTK-mCherry) to understand its activation and nucleocytoplasmic shuttling[87-89], and its roles in myeloid cell chemotaxis[90] and infection[85,91]. Alternative research methods have primarily involved fluorescently labeled antibodies for immunohistochemistry and flow cytometry applications. The former is limited to experimental models and requires protein over-expression, and the latter requires cell permeabilization and fixation. The approach developed here, utilizing a small molecule affinity ligand, is compatible with live cells, can be used *in vivo*, and has potential clinical applicability. Not only does Ibrutinib-BFL specifically bind to BTK, but also it remains bound until protein turnover due to the virtually nonexistent off-rate of covalent inhibitors. This feature will allow for long-term study of endogenous BTK in

live cells, providing a window into drug pharmacodynamics, as well as innate heterogeneity in responses to drugs targeting the BCR signaling pathway[13,83].

Beyond utilizing Ibrutinib-BFL in pharmacologic studies of next generation inhibitors, there are future diagnostic opportunities in which BTK-expressing lymphomas could be imaged in the clinic. While the current work focused on single cell imaging *in vivo*, we also anticipate whole body imaging applications. For example, the fluorine in BODIPY-FL could be exchanged for ^{18}F for positron emission tomography (PET) imaging, or entirely replaced via bioorthogonal ligands or direct ^{18}F attachment[60,92-94]. Alternatively, longer-lived isotopes such as Zirconium-89 could also be utilized in order to take full advantage of the probe's irreversible binding kinetics[95-99]. Such molecules may be useful in clinical imaging-based tests for whole body distribution and inhibition of BTK. Other areas of interest are to use these molecules for imaging BTK in macrophages during infection, or to use them as a readout during gene therapy for the immunodeficiency disorder X-linked agammaglobulinemia, which results from loss of functional BTK[100]. Irrespective of the contemplated use, we believe that the developed agent should be useful in a number of different applications. As covalent inhibitors have gained interest, we anticipate covalent imaging agents to follow, and Ibrutinib-BFL can provide a roadmap for such development.

3.5. Acknowledgements

We thank Yoshiko Iwamoto for histology, Dr. Jonathan Carlson for helpful discussions, Matthew Sebas for mouse surgery, Dr. Claudio Vinegoni for *ex vivo*

biodistribution imaging, Dr. Hidde Ploegh and Dr. Karin Strijbis for providing BTK-mCherry construct, Scott Mordecai for help with imaging flow cytometry, and the Szostak lab for help with fluorescent gel scanning. A.T. was supported by the Harvard Biophysics Graduate Program under NIH training grant T32008313 and by an NSF Graduate Research Fellowship under grant numbers DGE0946799 and DGE1144152. M.A.M. was supported by NIH training grant T32 CA079443.

3.6. Reflections and Future Work

The decision to design an imaging agent with an irreversible inhibitor scaffold provided a window into how the roadmap for the development of companion imaging drugs might differ for covalent drugs, which is important as more are developed due to their specificity to their target and extremely slow off-rate[79]. However the kinetics and binding constants also become complicated, as IC_{50}'s are time-dependent and covalent binding is relatively slower than reversible interactions. We found that relatively long washout times are required for high signal-to-noise *in vitro*, meaning that these probes are spectacular for labeling and tracking over time, but perhaps less useful for quick feedback.

To explore these issues further, follow-on experiments are being conducted in which binding is measured by anisotropy rather than by fluorescence signal. Bound and unbound Ibrutinib-BFL can therefore be differentiated based on the rotational freedom of the Bodipy FL fluorophore, which slows down when bound to protein[101]. This approach is being utilized to build binding curves of Ibrutinib according to both concentration and

time, and for measuring competitive binding of Ibrutinib-BFL with several other BTK inhibitors in development, including AVL-292[78,102]. Thus it will be possible to compare the binding kinetics and specificities of the various therapeutics, which are in parallel clinical trials. Additional follow-on work involves the synthesis of an AVL-292-BFL.

Another promising irreversible inhibitor in development is CO-1686 (Clovis Oncology), which specifically targets activating EGFR mutations and the T790M EGFR resistance mutation in non-small cell lung cancers, while sparing normal EGFR in healthy cells[103]. An imaging probe version of this drug could be useful in differentiating cancer cells from healthy cells in both targeted PET and in *in vitro* diagnostic tests, and is also being developed as a follow-on to this work.

Chapter 4.

On Chip Characterization of CNS Lymphoma in Cerebrospinal Fluid

Manuscript to be submitted has the following contributors:

Anna Turetsky*, KyungHeon Lee*, Jun Song*, Randy J. Giedt, Eunha Kim, Alexandra E. Kovach, Ephraim P. Hochberg, Cesar M. Castro, Hakho Lee, Ralph Weissleder

*Equal contribution

Author Contributions

A.T., C.M.C., and R.W. designed the research, and A.T., K.H.L., J.S., and E.K. performed experiments. A.T., K.H.L, J.S., and R.J.G. analyzed data. A.E.K. and E.P.H. provided clinical guidance. A.T., K.H.L., J.S., R.J.G., H.L., and R.W. prepared figures. A.T., K.H.L., J.S., and R.W. wrote the manuscript. All authors reviewed and edited the manuscript.

Molecular profiling of central nervous system lymphomas in cerebrospinal fluid (CSF) samples can be challenging due to the paucicellular nature of the limited samples. We designed a microfluidic chip able to process the entire CSF sample volume, capture single lymphoid cells in sub-nanoliter traps, and then profile the cells on-chip by fluorescence image analysis or by response to chemotherapeutic agents, all in less than one hour. We show that the system can detect scant lymphoma cells and quantitate their kappa/lambda immunoglobulin light chain

restriction patterns. The approach can be further customized for measurement of additional biomarkers, such as those for differential diagnosis of lymphoma subtypes or for prognosis, as well as for imaging exposure to experimental drugs.

4.1. Introduction

Central nervous system (CNS) lymphoma is diagnosed in about 10,000 new patients per year in the US and is either primary (de novo lymphoma) or secondary (metastases from systemic disease). Primary CNS lymphoma (PCNSL) accounts for ~1,500-3,000 patients in the US, but affects an estimated 2-6% of all AIDS patients and is thus more prevalent in low/middle income countries with high AIDS frequency[104,105]. With respect to secondary lymphoma, 25% of Diffuse Large B-Cell Lymphoma (DLBCL) and mantle cell lymphoma patients, and up to 50% of Burkitt Lymphoma patients will ultimately exhibit CNS involvement[106-109]. Importantly, secondary CNS lymphoma is often the cause of death in high-grade lymphomas unresponsive to treatment[110]. Clinical diagnosis of CNS lymphoma typically relies on conventional cytopathology of CSF or radiographic means (MRI). Recent molecular distinctions have been made between germinal (GCB) type DLBCL, activated (ABC) type DLBCL, and Burkitt's lymphoma, and prognosis and treatment choices have been shown to depend on these cell-of-origin distinctions, highlighting the need for a diagnostic platform that can support molecular phenotyping[12,15,111-113].

Lumbar puncture is used to collect small volumes of cerebrospinal fluid (CSF). CSF has a viscosity similar to water and contains distinct electrolytes, but also contains scant

cells[114]. In normal individuals, 1 mL of CSF contains 150-2,000 T lymphocytes, 80-1,100 monocytes, and 0-30 B lymphocytes, as well as other less common cell populations [115,116]. Table 4.1 summarizes the cell counts for the major cell populations. In patients with CNS lymphoma, lymphocyte populations increase in number and are often monoclonal. Conventional cytology (smear test) is only useful when lymphoma cells make up more than 5% of cells in a sample of CSF, and can be difficult to interpret due to similar morphology between benign and malignant lymphocytes[117]. Newer approaches such as flow cytometry have shown impressive sensitivity, but require sufficient numbers of cells for analysis [116,118]. Thus, estimates of secondary CNS lymphoma prevalence have differed in the literature.

To address these unmet needs, we sought to design a microfluidic chip that allows analysis of all harvested cells (i.e. without the need of sample preparation which often loses cells and/or alters them) and which could potentially be used in resource limited settings where HIV is more prevalent[119]. Based on previous designs of chips

Table 4.1. Cell populations in CSF

	Normal	CNS lymphoma	Inflammation
B cells (per mL)	0-30	10-500,000	200-43,000
T cells (per mL)	150-2,000	250-180,000+ (max 97.2%)	9,000-460,000
Monocytes (per mL)	80-1,100	—	—
Granulocytes (per mL)	20-430	—	—
NK cells (per mL)	0-50	max 7.4%	1,500-50,000

incorporating individual cell capture/analysis[120], we designed and developed an integrated device that allows comprehensive staining, phenotyping, and drug response measurements. We expect that this approach will provide a flexible platform to profile lymphoma cells from paucicellular samples, thus enhancing the accuracy and ease of CNS lymphoma diagnosis, the potential for biomarker-based treatments, and the ability to track the efficacy of those treatments over time.

4.2. Results

We designed a microfluidic chip which meets several criteria for processing CSF samples, including a) sites to capture a large number of lymphoid cells, such that if lymphoma cells make up 0.1% of the population, we could capture sufficient numbers of cells to identify a monoclonal population, b) antibody-free capture, c) capture sites for cells in the 8-10 μm size range, d) gaps so that erythrocytes would not be captured, and e) suitable build and materials for cellular analysis.

Figure 4.1 summarizes the procedure for lymphocyte detection and profiling. First, samples are harvested, typically in the range of 1-3 mL. The entire sample is then loaded onto the chip, cells are captured in sub-nanoliter traps, and can then be stained. Finally, images are analyzed using automatic algorithm to generate cell characterization data. The 0.75” x 1.5” chip contains a staggered “plinko”-like board with 24,000 staggered, butterfly-shaped traps arranged in four bands of 20 x 300 (Figure 4.1b). The capture site size was optimized for the size of a single lymphocyte, while a 4-μm gap between the butterfly “wings” was incorporated to allow smaller cells, such as erythrocytes, to pass

through without being captured. The chip were made using standard soft lithography techniques at a cost of <$1 per chip. With tens of thousands capturing sites, the chip enables high-throughput analysis. We calculated that even with gentle flow rates, cells

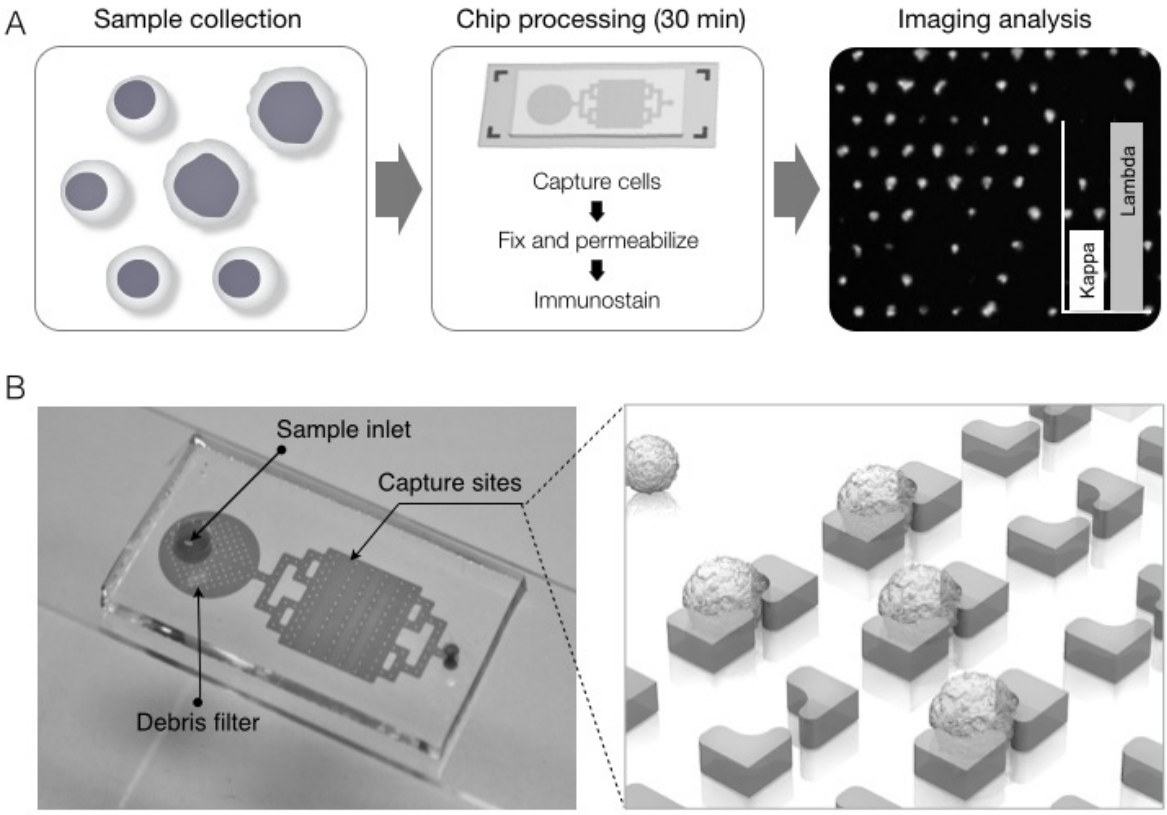

Figure 4.1. Process design. a. Summary of overall scheme: paucicellular samples are harvested and captured on the chip without preprocessing. Following on-chip fixation, permeabilization, and immunostaining, the chip is imaged and cytometry is carried out with an in-house image process algorithm. b. Photograph of lymphocyte capture chip attached to a microslide, showing inlet, debris filter, and capture area, which contains four arrays of 20 x 300 single-cell capture sites.

could be captured and stained in well under an hour, important for processing clinical samples (Figure 4.1).

We performed validation studies and capturing efficiency tests using fixed cells and beads. Using 10-μm beads, we found the optimal flow rate for maximum capture efficiency to be ~5 mL/hr (Figure 4.2). Interestingly, slower flow rates decreased capture efficiency, presumably due to inertial effects. We next tested the capture efficiency of cells. DB GCB-type DLBCL and the Daudi Burkitt's lymphoma cell lines were stained with CD45-APC (an extracellular pan-lymphocyte marker) and Hoechst nuclear dye, and imaged on the chip (Figure 4.2a). We were able to efficiently capture 10, 100, or 1000 of the pre-stained DB and Daudi cells using a 2 mL/hr flow rate to adjust for cellular flexibility (Figure 4.2d). The average capture efficiency of >90% is considerably better than the 17-30% cell loss attributable to each centrifugation step in traditional sample processing for flow cytometry analysis[121,122].

Once captured, cells were analyzed by multi-color immuno-imaging. As outlined in Figure 4.2, the imaging involves three broad approaches: i) the use of CD19 and/or CD20 to determine B cells; ii) the use of kappa or lambda light chains to identify clonal populations and iii) additional phenotypic markers for subtyping and prognostic tasks. We validated these markers using a panel of cell lines representing a variety of B-cell lymphomas (Figure 4.3). In addition to Daudi and DB, we also profiled SuDHL4, DOHH2, and Toledo GCB-type DLBCL lines, the RC-K8 ABC-type DLBCL line, and the Rec-1 mantle cell lymphoma line. Hut-78, a T-cell line, was used as a negative control, and CD45 indicates the presence of Hut-78 cells in the experiment (Figure 4.3,

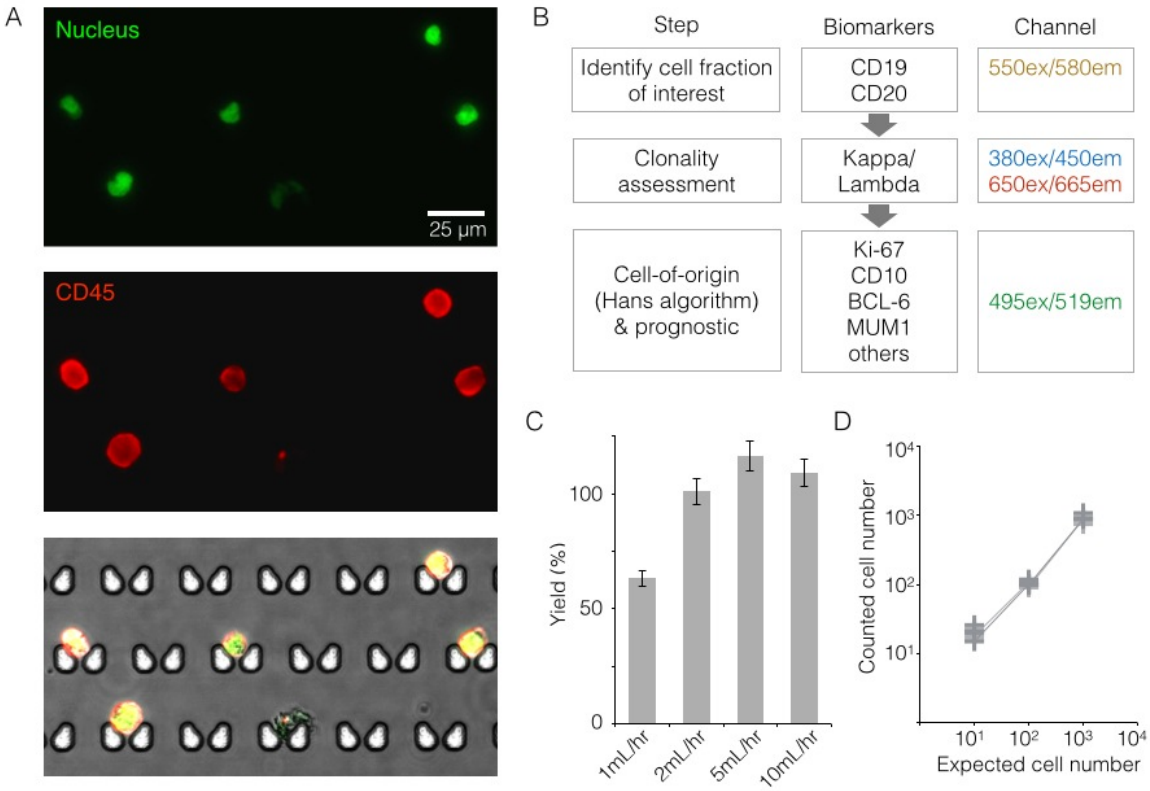

Figure 4.2. Validation of on-chip capture and imaging. a. DB cells dual-labeled with Hoechst and anti-CD45-APC, and captured and imaged on-chip. Capture sites are butterfly-shaped, staggered, and customized for lymphocyte size-based capture. Scale bar: 25 µm. b. Proposed workflow for clinical diagnosis using image analysis. c. Left, optimization of flow rate based on capture efficiency of 10 µm beads; right, capture efficiency of DB and Daudi cells is greater than 90% when 10, 100, or 1,000 lymphoma cells were introduced to the chip.

bottom row). These experiments showed, for example, that it is important to include both CD19 and CD20 in identifying B cells. This is also supported by published literature, as CD20 has been sometimes found to be decreased either due to cell-of-origin or anti-CD20 immunotherapy[123-125]. We also found that some lymphoma cell lines, such as Toledo cells, do not express immunoglobulins, which informed choices of cell lines for the validation studies of our chip and algorithm.

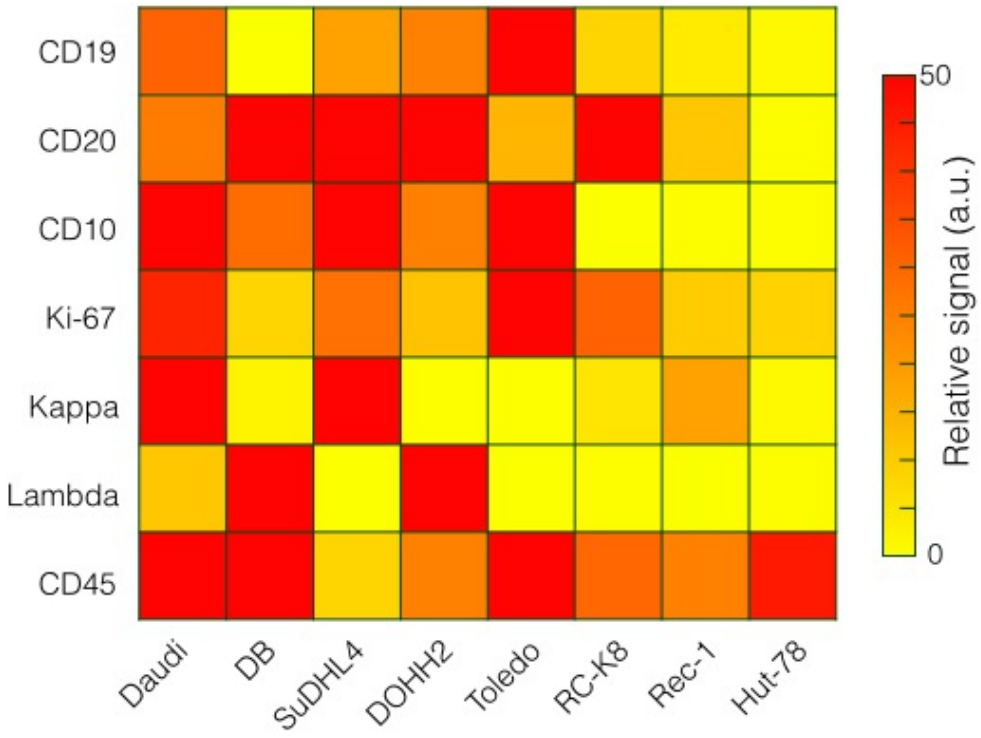

Figure 4.3. Antibody validation and cell line profiling by flow cytometry. Relative expression levels of B-cell antigens relevant to diagnosis and prognosis (rows) on several lymphoma cell lines (columns). Daudi is a Burkitt's lymphoma line; DB, SuDHL4, DOHH2, and Toledo are GCB-type DLBCL lines, RC-K8 is an ABC-type DLBCL line, Rec-1 is a mantle cell lymphoma line, and Hut-78 is a T-cell lymphoma control.

Several different lymphomas arise from germinal center B cells, such as Burkitt's and some DLBCLs (GCB-type), but most primary CNS lymphomas are ABC-type DLBCLs[126]. As expected, we found the GCB marker CD10 expressed in all the GCB cell lines tested, but not in ABC-type or mantle cell lymphoma. Since ABC-DLBCLs tend to be more aggressive, higher-grade lymphomas, we chose Ki-67 as an important marker for characterization and prognosis[127]. Our data suggests that low Ki-67 in a monoclonal population would indicate the need for testing additional lymphoma markers, such as for GCB-type DLBCL or mantle cell lymphoma. MUM1 may also be important, as it was shown to be expressed in over 90% of PCNSLs[126].

We chose to use Daudi and DB cells as a model system for on-chip analysis, since they respectively highly express kappa and lambda light chain. To demonstrate both extracellular and intracellular antigen analysis, we performed on-chip staining using CD19 and CD20, kappa and lambda, and Ki-67. We prepared cells for on-chip testing by diluting DB and Daudi lymphoma cells into artificial CSF. The cells were then fixed and stained on the chip, and imaged in four channels in under an hour (Figure 4.4; see Table 2 for antibody clones and fluorochromes). Figure 4.4a shows the overlay of the four imaging channels after a 1:1 mixture of DB and Daudi cells was captured and stained on-chip, while Figure 4.4b demonstrates our ability to also perform high-resolution imaging of individual cells and markers. Although the cell populations appear to be quite heterogenous, their restricted kappa/lambda expression can be seen at higher magnification (Figure 4.4b).

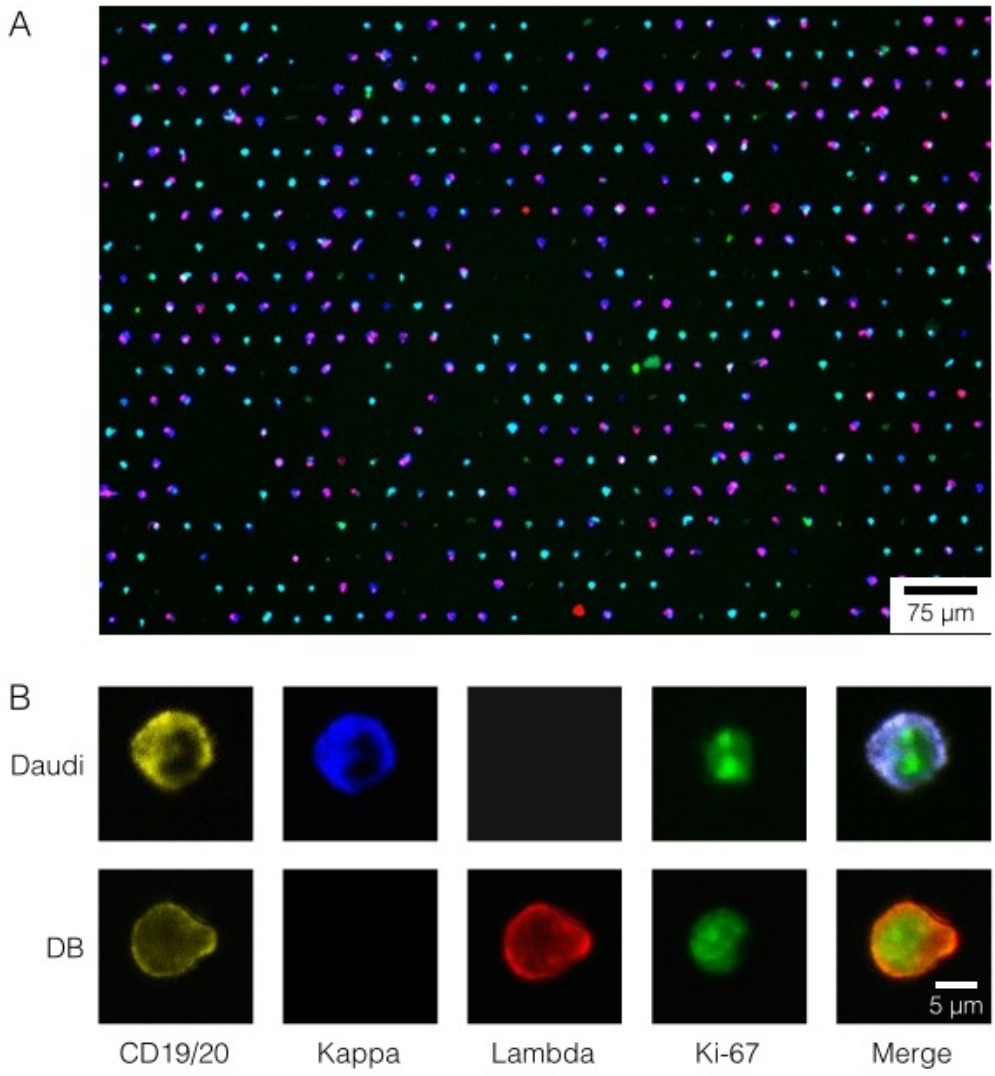

Figure 4.4. On-chip imaging. A 1:1 mixture of DB and Daudi cells were captured and stained on-chip using a cocktail of antibodies: anti-CD19-PE, anti-CD20-PE, anti-Kappa-Brilliant Violet 421, anti-Lambda-Alexa Fluor 647, and anti-Ki-67-Alexa Fluor 488. a. Low-magnification image shows overall capture site layout and cell heterogeneity. Scale bar: 75 µm. b. High-resolution images of differential expression of individual markers on the two cell lines. Scale bar: 5 µm.

Table 4.2. Antibodies

Antigen	Clone	Provider	Fluorochrome (on chip)
CD10	HI10a	BioLegend	—
CD19	HIB19	BioLegend	R-PE
CD20	2H7	BioLegend	R-PE
CD45	HI30	BioLegend	—
Ki-67	B56	BD Biosciences	Alexa Fluor 488
κ light chain	MHK-49	BioLegend	Brilliant Violet 421
λ light chain	JDC-12	BD Biosciences	Alexa Fluor 647

As a proof-of-concept for future analysis of lymphocytes from clinical samples, we developed an image processing algorithm for clonality assessment using the spiked CSF samples. Following the workflow described in Figure 4.2, we first made a mask around cells expressing CD19 and/or CD20 (PE channel), and then quantified the mean fluorescence intensity from our target channels in each individual cell (Figure 4.5a). A size filter was also included to exclude non-cell debris from analysis (Figure 4.5a, grey arrow). After quantification, we were able to clearly distinguish DB (lambda-expressing) and Daudi (kappa-expressing) cell populations from samples containing about 1,000 cells (Figure 4.5b).

Finally, drug sensitivity testing would be clinically useful to guide intrathecal and/or systemic chemo and targeted therapies. We hypothesized that primary captured cells could be exposed to companion imaging drugs directly on chip. Some of these agents have recently been reported, such as Ibrutinib-BFL, an inhibitor of Bruton's Tyrosine Kinase (BTK)[128]; others include fluorescent rituximab or caged methotrexate. Ibrutinib is

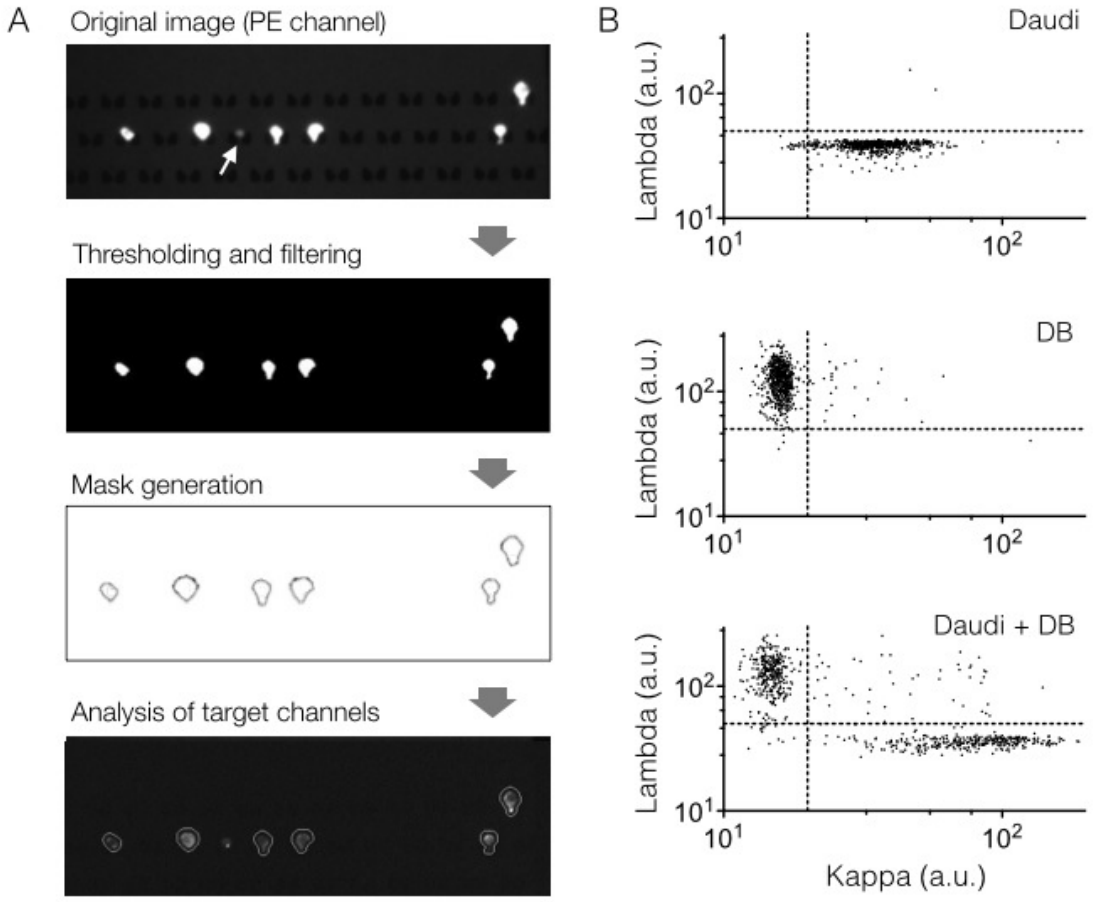

Figure 4.5. Cell profiling for kappa/lambda monoclonality by image analysis. a. Sample image analysis using an in-house image processing algorithm. Thresholding in the PE channel (CD19, CD20) is used to select B cells, and size-based filtering removes non-cell debris (grey arrow). Target channels are analyzed within masks created from PE channel gating. b. Scatterplots of mean pixel intensities from target imaging channels show clear separation of populations based on kappa and lambda light chain expression; top, DB cells; middle, Daudi cells; bottom, 1:1 mixture of DB and Daudi cells.

approved for several B-cell malignancies, including mantle cell lymphoma, and the Rec-1 cell line has been shown to be sensitive to the drug[129,130]. Imaging the Rec-1 cells with Ibrutinib-BFL on the chip shows not only the binding of Ibrutinib, but also their cell-to-cell heterogeneity due to differences in BTK inhibitor sensitivity and BTK protein turnover (Figure 4.6).

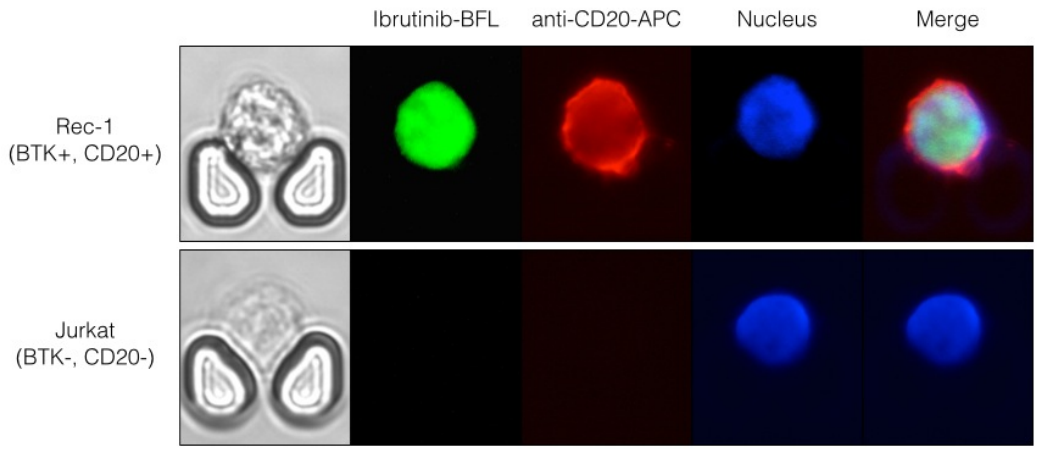

Figure 4.6. Drug testing. On chip imaging of BTK-positive Rec-1 cells or BTK-negative Jurkat cells using fluorescent BTK inhibitor (Ibrutinib-BFL), anti-CD20-APC, and Hoechst stain.

4.3. Materials and Methods

4.3.1. Fabrication of single cell capturing chip

SU-8 based soft-lithography techniques were used for patterning the single cell capturing structure. First, photoresist SU-8 2025 (MicroChem Corp, Newton, MA, USA) were spin coated on silicon wafer (University Wafer Inc, Boston, MA, USA). The wafer

was baked at 65°C and 95°C, and then exposed to UV light through a pattern mask. After exposure, the pattern was baked and then developed using SU-8 developer (MicroChem Corp, Newton, MA, USA).

PDMS channels were made using the SU-8 wafer mold. After patterning, the wafer surface was treated by trichlorosilane (Sigma Aldrich, St Louis, MO, USA) under vacuum. PDMS (Dow Corning, Midland, MI, USA) was mixed with curing agent at a ratio of 10:1. The mixtures was poured over the treated wafer mold and baked at 60°C for one hour to cure. After curing, the PDMS layer was lifted from the wafer and bonded to a glass slides using surface plasma treatment.

4.3.2. Flow rate optimization

Fluorescent 10 μm micro-beads (Bangs Laboratory, Fishers, IN, USA) were used to test capture efficiency and to identify the optimal flow rate. First, PDMS channels were preconditioned using pluoronic copolymer solution with 0.1% F127 in DI water (Sigma Aldrich). The inlet of the channel was connected to a reservoir of beads in solution and the outlet to a syringe pump. The syringe pump was programed to control the flow rate of the fluid. Bead solutions were diluted to 300 beads per 100 μL and the total bead counts were about 300. After capturing, we use fluorescent microscope to image and count the total number of beads captured in the chip.

4.3.3. Cell lines

The GCB-type diffuse large B-cell lymphoma (DLBCL) cell lines DB and Toledo were generously provided by Dr. Anthony Letai (Dana Farber Cancer Institute, Boston, MA, USA). The RC-K8 ABC-type DLBCL cell line was a generous gift from Dr. Thomas Gilmore (Boston University, Boston, MA, USA). The GCB-type DLBCL cell lines SuDHL4 and DOHH-2 and the mantle cell lymphoma cell line Rec-1 were provided by Dr. Russell Ryan (Massachusetts General Hospital, Boston, MA, USA). Daudi Burkitt's lymphoma cell line and Hut-78 T-cell lymphoma lines were from ATCC (Manassas, VA, USA). B-cell lymphoma lines were cultured in RPMI 1640 media and Hut-78 cells were cultured in Iscove's Modified Dulbecco's Medium (both Invitrogen, Grand Island, NY, USA), both supplemented with 10% fetal bovine serum at 37°C and 5% CO_2.

4.3.4. Titration of cells

Approximately $1.5x10^6$ cells from culture flasks were washed with PBS and stained for 30 minutes at room temperature in 1.5 μg/mL Hoechst 33342 (Invitrogen) and APC anti-human-CD45 antibody according to manufacturer instructions (Clone HI30, BioLegend, San Diego, CA) in PBS containing 2% albumin from bovine serum (BSA) (Sigma Aldrich). Following a quick wash with PBS, cells were fixed in 2.6% paraformaldehyde (PFA) in PBS (initial 4% PFA in PBS, Affymetrix, Santa Clara, CA, USA) at room temperature for 20 minutes. Cells were then washed 3x with PBS and counted using a Bright-line hemocytometer (Hausser Scientific, Horsham, PA, USA). The

samples were then aliquoted and diluted for preparing sample of 10, 100, and 1,000 cells in 1 mL PBS in siliconized microtubes (Clear-view Snap-Cap, Sigma-Aldich). Each batch of samples was then introduced to a preconditioned device at a flow rate of 2 mL/ hr. After 30 minutes, the cells were trapped at the capture sites. The cells were then counted by eye and showed good agreement with expected cell counts by hemocytometer, with an average recovery rate >90%.

4.3.5. Flow cytometry for cell line profiling

To measure expression of extracellular markers, cells were washed with PBS, fixed in 2.6% PFA in PBS (initial 4% PFA in PBS, Affymetrix) for 15 minutes at 37°C, then washed 2x with PBS and 1x with PBS containing 2% BSA (staining buffer, SB), and allowed to block for ~30 min. Approximately $5x10^5$ cells in were incubated with 4.4 µg antibody or mouse IgG control in 42.5 µL (CD10, CD19, CD20, CD45) or with 2.5 µg antibody in 50 µL (κ light chain, λ light chain) for 30 minutes at 4°C. For intracellular Ki-67 detection, cells were fixed and permeabilized using the eBioscience Foxp3/ Transcription Factor Staining Buffer Set according to manufacturer instructions (San Diego, CA, USA) and allowed to block in perm/wash buffer containing 2% BSA (permSB) for ~30 min following washout of fix/perm buffer. ~$5x10^5$ cells in were incubated with 5 µg antibody or mouse IgG control in 50 µL for 30 minutes at 4°C. Cells were then washed 1x with SB or permSB and incubated in 20 µL 1:100 R-phycoerythrin (PE) goat anti-mouse-IgG (H+L) (1 mg/mL, Invitrogen) secondary antibody reagent for 30 minutes at 4°C in SB or permSB. Unstained controls were incubated in just SB or

permSB at each step. Staining was done in 96-well V-bottom plates (Corning, Corning, NY, USA). Following 1x wash with SB or permSB, cells were resuspended into 200 μL PBS containing 0.5% BSA and transferred into Falcon tubes with cell strainer caps (BD Biosciences, San Jose, CA, USA) for flow cytometry. Stained and unstained control samples were measured on a BD LSRII Flow Cytometer equipped with an Argon 488-nm laser using a PE filter set (all BD Biosciences), and analysis was done using FlowJo software (Tree Star, Ashland, OR, USA). Mean PE values were found for each cell line / antibody combination and normalized to (signal - background)/(IgG - background) for CD10, CD19, CD20, CD45, and Ki-67 or (signal - background)/(secondary - background) for κ light chain and λ light chain. A heat map was generated using MATLAB (MathWorks, Natick, MA, USA) and scaled according to the normalization above, with max 50x signal/control for optimum coloration.

4.3.6. Antibodies

Several antibodies for each biomarker were tested using combinations of cell lines to allow for positive and negative controls, including various clones and manufacturers. Purified antibodies for cell profiling were chosen based on a combination of high signal, low background in negative control cells, mouse host (for standardized secondary reagent), and cost, and are summarized in Table 4.2 (all chosen were obtained from BD Biosciences or BioLegend). Fluorescent antibodies from the same clone and manufacturer were chosen for on-chip staining.

4.3.7. On-chip cell staining and imaging

DB and Daudi cells were prepared by eliminating dead cells (common in suspension culture) using Ficoll-Paque PLUS (GE Healthcare, Little Chalfont, UK). 4 mL cells in culture media were carefully pipetted onto 4 mL Ficoll, and centrifuged at 400 g, 19°C for 30 minutes. The live cells settled at the interface and were collected, diluted 1:1 with PBS, and centrifuged at 150 g, 19°C for 10 minutes. The cell pellet was resuspended at a concentration of 10^6/mL in PBS. About 1000 DB, Daudi, or a 1:1 mixture of cells were then diluted into 1 mL of artificial cerebrospinal perfusion fluid (aCSF; Harvard Apparatus, Holliston, MA, USA). Cells were captured onto the chip at the optimized flow velocity for cells of 2 mL/hr. Next, we used the fixation/permeabilization buffer (fix/perm) and permeabilization/wash buffer (perm/wash) from the eBioscience Foxp3/Transcription Factor Staining Buffer Set to fix and permeabilize cells on the chip. Fix/perm was perfused over the cells for 10 minutes, followed by perm/wash containing 2% BSA for 5 minutes, and PBS containing 2% FBS (Invitrogen) / 1% BSA for 5 min, all at a flow rate of 1 mL/hr. A cocktail of antibodies containing 1 μL of anti-Ki-67, anti-CD19, and anti-CD20, and 2 μL of anti-κ light chain and anti-λ light chain (see Table S1 for clone, manufacturer, and fluorochrome information; all were obtained and used without prior dilution) was perfused over the cells at 1 mL/hr for 5 minutes. Lastly, to reduce background signal from antibodies binding to the PDMS surface, washing buffer (PBS with 2% FBS / 1% BSA) was perfused at 1 mL/hr for 5 minutes. Alternatively, cells were exposed to Ibrutinib-BFL using conditions recently described prior to imaging[128]. Images were captured on a Nikon Eclipse TE2000S inverted microscope (Nikon, Tokyo, Japan)

equipped with four Chroma Technology (Bellows Falls, VT, USA) filter sets (31000v2 - DAPI/Hoechst/AMCA; 41001 - FITC/ EGFP/ Bodipy Fl/ Fluo3/DiO; 41002b - TRITC (Rhodamine)/DiI/Cy3™/AF546 with narrow-band excitation filter; and 41024 - Cy5™ Longpass Emission). A CMOS camera (Andor Technology, Belfast, UK) was used to capture 10X images in four fluorescent channels corresponding to the antibody-conjugated fluorochromes listed in Table 4.2.

4.3.8. Image Analysis

Images were analyzed using an in-house Matlab (Mathworks, Natick, MA) script. Briefly, images from the CD19/20 (PE) channel were thresholded and binarized using Otsu's method with an additional uniform offset to compensate for the specific properties of the images. Following thresholding, image regions were analyzed and filtered by eliminating any regions greater or less then preset total pixel areas based on the magnification of the images. Additional noise was filtered by using "open-close" morphological filtering. Boundaries of the remaining regions were then recorded and overlaid on target channels where values for the pixels in each mask area for both lambda (Alexa Fluor 647) and kappa (Brilliant Violet 421) channels were generated. Final values for both lambda and kappa channels for each cell were calculated by averaging the most intense 25% of pixels in each region.

4.4. Discussion

CNS lymphoma is difficult to diagnose and characterize at the site of disease, often requiring multiple invasive lumbar punctures to retrieve sufficient numbers of cells to allow cytopathologic analysis. Due to the paucicellularity and heterogeneity of CSF samples, we hypothesized that a PDMS-based capture device would allow characterization of populations of lymphoma cells in the CSF on a single-cell level. Here, we show that we can indeed image both intracellular and extracellular diagnostic markers from lymphoma cells spiked into artificial CSF in under an hour, and further use an image processing algorithm to quantitate their expression level. By adding additional criteria, differential diagnosis using the Hans algorithm can identify the cell-of-origin of a PCNSL, perhaps pointing to an undiagnosed systemic lymphoma if germinal origin is found[126,131].

For secondary CNS lymphoma, it is important to know the extent of metastasis, its aggression, and its response to treatment. Methotraxate is currently used intrathecally or at very high systemic doses to treat CNS disease, but it has thus far not been possible to track response to treatment other than by low resolution MRI or insensitive cytology, neither of which would catch minimal disease[132-134]. By profiling lymphoid cells in CSF based on kappa/lambda restriction or proliferative grade, or by customizing antibody staining for intracellular or extracellular markers based on particular characteristics of the primary tumor (e.g. c-myc rearrangement, CD10, CD5, etc.), CNS lymphoma cell counts can be tracked over time and prognostic assessments can be made[135,136]. Additionally, there are several new lymphoma drugs in clinical trials, yet few are tested for CNS

efficacy. This approach could provide a companion diagnostic that can directly test for brain-blood-barrier drug permeability or look for specific marker inhibition following intrathecal administration, such as BTK inhibitors or anti-CD20[137-140]. To test for such drug accumulation (single cell pharmacokinetics) in primary lymphoma cells, we tested Ibrutinib-BFL directly on chip. Finally, another approach includes removing CSF after intrathecal injection of chemotherapy drugs to track treatment response over time.

Additional technologies can be added to front- or back-processing on the chip for further improvements and applications. For example, it will be possible to further purify B cells by negative selection of other cell types, such as T cells and monocytes. Since the capture is passive (i.e. no antibodies on the chip), we can also use optical approaches to remove single cells of interest off the chip for further characterization, such as by quantitative PCR and sequencing — now possible on a single-cell level [141]. Another possibility will be to add a CCD or iPhone camera readout to enable the chip to be used for lymphoma diagnosis in resource-poor settings. We estimate that in this application a 1:5 cutoff ratio of kappa-to-lambda fluorescence signal would be enough to establish clonality with high specificity. Overall, we believe this new application of single-cell molecular profiling on a microfluidic chip for lymphoma will address questions regarding the diagnosis and treatment response of the disease not only in CSF, but also in other paucicellular samples such as fine needle aspirates, peritoneal fluid samples, pediatric applications or vitreous fluid analysis.

4.5. Future work

The next step in this project is to utilize our microfluidic technology to profile clinical samples from lumbar punctures from patients with suspected and/or confirmed CNS lymphoma. We plan to start our study with discarded tissue samples, for which half of the sample will be sent for pathology, either cytopathology or flow cytometry. It will be interesting to compare the performance of the microfluidic chip (i.e. sensitivity and specificity) to these more conventional methods. We may also be able to acquire serial samples from patients known to be positive for CNS lymphoma who are receiving a course of intrathecal treatment, in which we could map whether lymphoma cell count decreases or increases over time, as well as any change in molecular markers over the course of treatment. This may allow us to hone in on effective treatments for CNS lymphoma, whether CSF lymphoma cell counts over time correlate with outcome, whether patients are being given drugs via painful lumbar punctures without a need for them, and the patient profiles for which the administered treatments are most effective[134].

In terms of further technology development, we also plan to explore expanding our ability to multiplex (beyond 4-5 fluorescent channels) by performing multiple rounds of staining using stripping buffers. Finally, we will optimize an optical tweezers method to remove single cells from the chip for genomic analysis. Since relatively little is known about the incidence and treatment response of CNS lymphomas due to the limited-information tests currently available, it will be particularly interesting to use these microfluidics approaches to investigate the differential biology of lymphoma cells in the CSF.

(blank page)

Chapter 5.

Paper-based TCO/Tz Click Chemistry in Low-Cost, Point-of-Care Diagnostics

Thomas Reiner, Eunha Kim, and I designed the research, performed chemical synthesis and other experiments, and prepared figures. Joshua Dunham assisted with fluorescence imaging and David Issadore contributed an introduction to the field and helpful discussions.

In the quest for lower cost diagnostics, paper-based tests are a promising solution. However, the design of semi-quantitative assays has been largely limited to the detection of analytes by color or conductance changes, and it may be helpful to introduce other types of chemistries to enable a broader array of tests. Here we show that we can perform cellulose chemistry on solid papers, including a synthetic route to "clickable" trans-cyclooctene(TCO)-paper for bioorthogonal click chemistry reactions. We can then detect the binding of tetrazine(Tz)-modified dyes to the paper through the TCO/Tz click reaction using either a spot-based or lateral-flow approach. Paper-based chemistries can also enable a variety of potential applications in drug screening or substrate patterning.

5.1. Introduction

Newly realized paper-based microfluidics has recently emerged as a platform and opportunity to translate a variety of diagnostics into new formats[24,142,143]. This method

has several key advantages over traditional diagnostics, particularly in resource-poor settings in the developing world, including a) ultra-low-cost materials, b) no need for external pumps, c) small sample sizes, d) inherent filtration of cells, such as from blood, and e) disposable[24,143-147]. It is interesting to note that paper diagnostics have existed for decades in the form of pregnancy and other dipstick tests, but only recently has the approach been applied to new problems, and only recently has microfluidics engineering been used to move tests into two- and three-dimensional formats[148,149].

Microfluidics relies on low Reynolds number, laminar flow, typically realized by patterning micro-scale channels in silicon wafer molds and casting these molds in polymers such as polydimethylsiloxane (PDMS)[150]. The pores in cellulose are on the same scale as these channels, providing a method to achieve laminar flow without the need for clean-room micropatterning techniques. Laminar flow is non-turbulent, so the flow of liquids can be directed based on pressure from different non-mixing streams; thus features from PDMS-based microfluidics such as programmable valves, hydrodynamic focusing, and multistep assays can be translated to the paper-based format[151-158]. Macro-scale patterning (to create ~1-5 mm in diameter channels or "wells" for ELISA-type assays) on paper-based devices has been achieved using wax-printing, laser-cutting, origami, photolithography, or "sizing" agents, while materials include chromatography paper, filter paper, or glass fiber membrane[159-167]. Additional patterning can be done with nano particles or inkjet printing[168,169]. These fabrication and patterning techniques, combined with microfluidic and other 3-D design principles, have allowed for the development of various, multiplexed devices utilizing lateral or vertical flow, for

applications including infectious disease, organ function/injury, drug quality screening, and environmental safety[25,26,170-178].

Current assays performed on paper devices include ELISAs and other immunoassays, nucleic acid hybridization, and color- and electrochemistry-based analyte detection [177,179-191]. However, additional tools are needed to widen the array of possible tests that can be developed. By applying traditional chemistry approaches to paper patterning and reactions on paper, it will be possible to create new tests involving small-molecule detection and patterning. We sought to leverage the [4+2] Diels-Alder cycloaddition using TCO/Tz (described in depth in Chapter 2) to create new capabilities on paper-based devices. Some chemistries have been recently used to functionalize solid paper substrates[192-194], but this is the first demonstration of click chemistry for detection during paper-based assays. We first confirmed that we could perform standard chemical reactions on chromatography and filter papers, and then went on to make "clickable" TCO-paper with small-molecule paper sites. The functionality of the TCO-paper was then demonstrated in several formats. Although we have not yet applied these methods to a diagnostic assay, we believe it could have applications in the detection of a variety of drugs and drug-targets.

5.2. Results

To test whether we could translate published synthetic chemistry approaches for the modification of cellulose in solution to solid-substrate commercial paper fibers (e.g. chromatography and filter papers), we first performed an acetylation reaction to make

hydrophobic paper (Figure 5.1a). As the material of choice for much of the early paper microfluidics work[24,142,159], Whatman 1 Chr paper was used for the starting material. Cut pieces (about 20 cm^2 in size) were submerged in acetic anhydride with 10% pyridine and heated to 60°C for 24 hours. After washing the product, it was confirmed that the paper was hydrophobic, not allowing water droplets to soak into the fiber (Figure 5.1b).

Having confirmed that it was possible to sufficiently modify the hydroxyl groups of commercial solid paper fibers to see a change in macro-scale properties, we went on to make Amine-Paper, and finally clickable TCO-Paper. We first chose the material for reaction, as various manufactured cellulose papers have varying properties[195]. Whatman 1

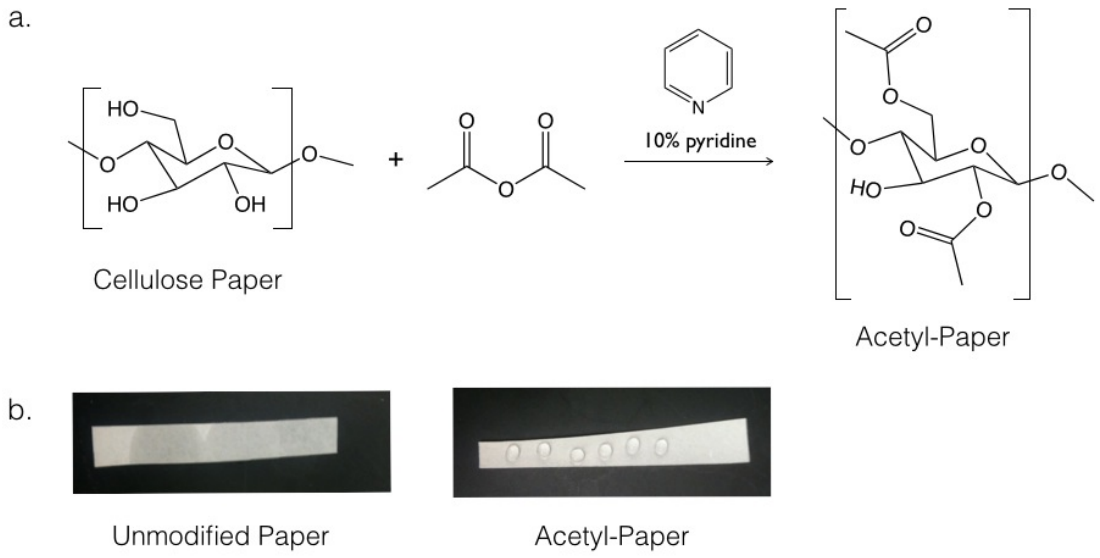

Figure 5.1. Acetyl-Paper. a. Reaction scheme for acetylation of cellulose to make hydrophobic paper. b. When droplets of water are introduced to unmodified paper, they soak into the hydrophobic paper. In contrast, droplets sit on top of the more hydrophobic acetylated paper.

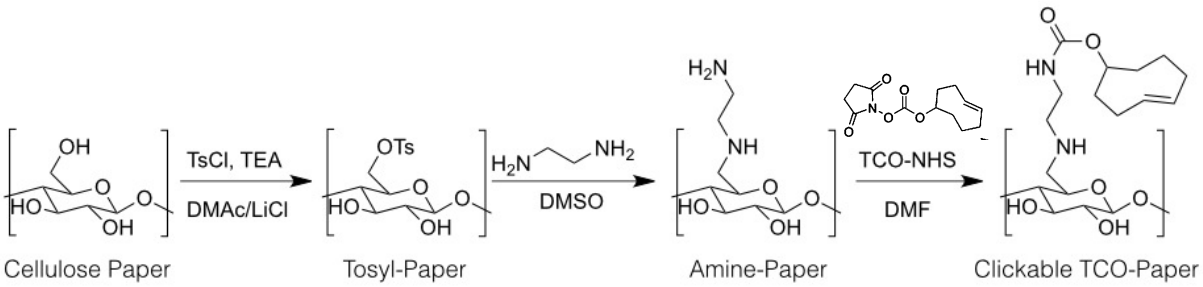

Figure 5.2. TCO-Paper synthetic scheme. Clickable TCO-Paper is synthesized in three steps from cellulose filter paper. In the case of TCO-PEG-Paper, a PEG4 linker separates the TCO from the sugar.

Chr chromatography paper is 180 µm thick with 11 µm average pore size, while Whatman #4 filter paper is 205 µm thick with 20-25 µm average pore size. In testing the two papers, better reaction efficiency was found for the #4 filter paper, perhaps due to the larger pore size, which allows for greater interaction between molecules in solution and on the fiber. The reaction scheme to make TCO-Paper is shown in Figure 5.2. In brief, cellulose paper was first reacted with 4-Toluenesulfonyl chloride (TsCl) to yield Tosyl-Paper. After a washing and an *in vacuo* drying step, Tosyl-Paper was reacted with diaminoethylene in DMSO to make the amine functionalized Amine-Paper. Finally, the Amine-Paper was reacted with TCO-NHS or TCO-PEG4-NHS to yield TCO-Paper or TCO-PEG-Paper, respectively. TCO-PEG4-NHS was tested since we thought the longer linker may lead to different positioning of the functional group within the paper fibers.

The paper products were characterized at two stages of synthesis: Amine-Paper and TCO-Paper / TCO-PEG-Paper. To test for primary amine functional groups, a ninhydrin

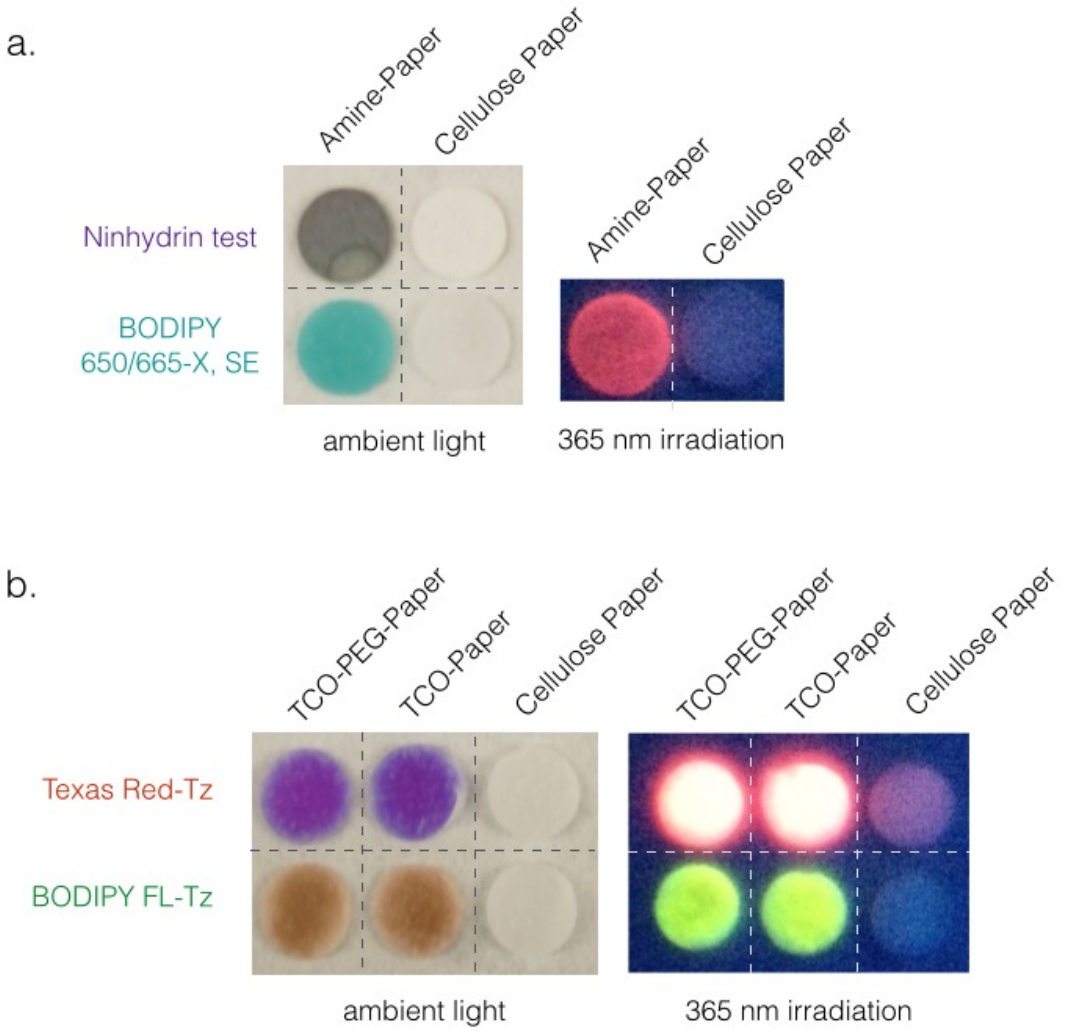

Figure 5.3. Characterization. a. Amine-Paper testing. Ninhydrin solution changes color in the presence of primary amines when heated; Bodipy 650/665-X, SE binds to Amine-Paper, but not to unmodified cellulose. b. TCO-Paper testing. Texas Red-Tz and Bodipy FL-Tz dyes bind to TCO-Papers, but not to unmodified cellulose. Dye was pipetted into the center of each circle, and the reaction is so quick that white edges are visible where dye did not wick any further. Dyes are shown under white light and UV light; paper circles are 4 mm in diameter.

test was performed on Amine-Paper and starting material (unmodified Whatman #4 filter paper) (Figure 5.3a, top). In addition, we tested the reaction of the primary amine groups with a Bodipy 650//665-X succinimidyl ester (SE) dye under the same conditions as the Amine-Paper-to-TCO-Paper synthetic step. After washing with DMSO, the dye remained covalently bound to Amine-Paper, yielding a colored, fluorescent paper, while the dye was cleanly washed away from unmodified paper (Figure 5.3a, bottom). The TCO-Papers' clickability was characterized using two tetrazine-conjugated dyes, Texas Red-Tz (**2.8**) and Bodipy FL-Tz. Notably, when the dyes were pipetted into the center of 4 mm-circular cutouts of TCO-Paper or TCO-PEG-Paper, the click reaction occurred so quickly that the dye could not wick to the perimeter of the circle. After washing, Tz-dyes were washed away from unmodified paper, but remained covalently bound to TCO-functionalized papers, visible under white or UV light (Figure 5.3b). No difference was noticeable between the reactivities of TCO-Paper and TCO-PEG-Paper.

To begin to build paper-based microfluidic devices for small molecule assays, we wax-printed test devices using a wax printer and a hot plate to melt the wax into hydrophobic barriers permeating the paper. Several organic solvents were tested against the wax barriers for their potential to transport organic small molecules in a lateral flow assay. We found that the wax channels withstand DMSO better than DMF, ethanol, or methanol (Figure 5.4a). Since 100% DMSO was nevertheless able to dissolve the wax, we next tested the ability of 50% and 75% DMSO in water to transport a model small molecule drug, AZD2281-Tz (**2.17**). 75% DMSO was found to be the optimal solvent for balancing the needs to solubilize and transport organic small molecules, yet not bleed into

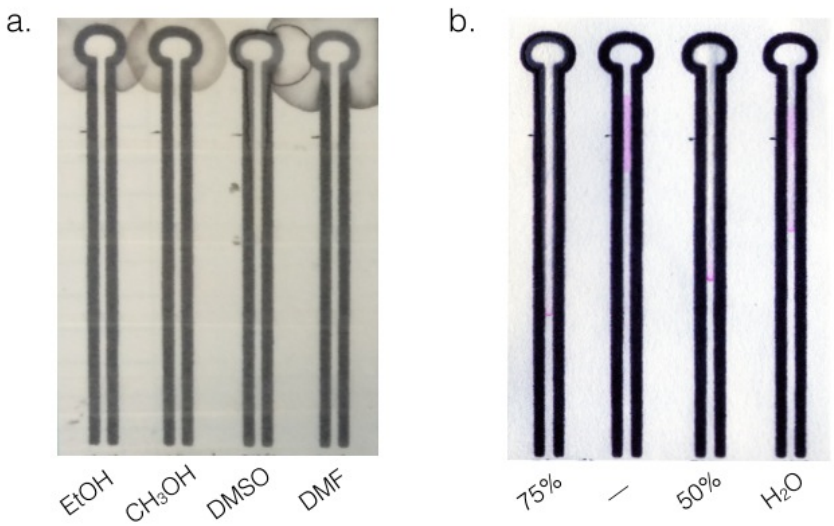

Figure 5.4. Solvent optimization. a. Hydrophobic wax channels are able to withstand DMSO better than ethanol, methanol, or DMF; DMSO traveled down the channel from the top, whereas other solvents formed rings where they were added to the paper. b. In a race down wax-printed lanes, 75% DMSO transports AZD2281-Tz (pink) the farthest down the channel. AZD2281 was initially spotted where shown in the control (—).

the wax channels (Figure 5.4b).

One application of TCO-Paper is as a capture site for a tetrazine-conjugated dye or drug molecule. To test it in a lateral flow assay format, the TCO-Paper was first “grafted" onto a wax-printed channel by using a biopsy punch to punch a hole out of the channel and replace it with a circle of TCO-Paper (Figure 5.5a; photographs in Appendix C). A paper-based, lateral-flow click chemistry reaction was then performed and imaged on a fluorescence macroscope. Texas Red-Tz was spotted onto a paper device and 75% DMSO was introduced upstream to flow down the device, carrying the Texas Red-Tz

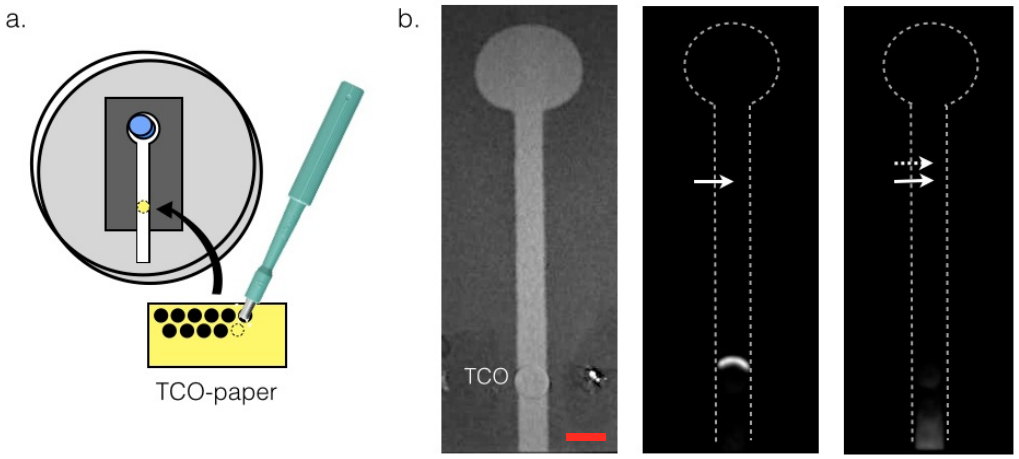

Figure 5.5. Lateral flow test. a. Schematic of paper device shows wax-printed channel in a 10-cm petri dish; blue is a cigarette filter for solvent-loading and yellow represents the TCO-paper that was cut and replaced part of the channel as the capture site. b. Brightfield (left) and fluorescent images of a lateral flow test. At the solid white arrows, 1 µL of Texas Red-Tz dye was spotted prior to lateral flow; at the dotted arrow, ^{19}F-TCO was co-spotted to block binding of the dye to the TCO-paper. Scale bar: 0.5 cm.

over the TCO-Paper capture site. Upon contact with the TCO-paper, Texas Red-Tz was clearly visible bound to the capture site (Figure 5.5b). The Texas Red-Tz reaction with TCO-Paper can be blocked by co-spotting ^{19}F-TCO (**2.15**), demonstrating the specificity of the reaction (Figure 5.5b, far left).

5.3. Materials and Methods

Unless otherwise noted, all reagents were purchased from Sigma-Aldrich (St. Louis, MO, USA) and used without further purification.

5.3.1. Synthesis and Characterization of Acetylated Paper

Acetylation of paper was adapted from previously published procedures[196]. Six 1.5x2" cutouts of Whatman 1 Chr cellulose chromatography paper (1; GE Healthcare, Piscataway, NJ, USA) and a magnetic stirrer were dried in a 150°C oven for two hours, giving a final dry paper mass of 1.12 g (~7.4 mmol cellulose units). 10% pyridine in acetic anhydride were added to submerge the paper and the resulting mixture was heated to 60°C under reflux for 24 hours, giving acetyl-cellulose, a white paper. The paper was then washed on a Büchner funnel sequentially with 250 mL each of water, EtOH, methanol, diethyl ether, water, and acetone, and then dried *in vacuo* overnight. The hydrophobicity of acetylated paper was tested against control unmodified 1 Chr paper by introducing water droplets onto paper strips. Results were photographed using an iPhone camera (Apple Inc., Cupertino, CA, USA).

5.3.2. Synthesis of TCO-Paper

Tosylation of paper, followed by amination, was adapted from previously published procedures[197-201]. All modified papers were stored in vials at -80°C.

Tosyl-Paper

~200 mg (~1.2 mmol) Whatman #4 cellulose filter paper (GE Healthcare) was dried in a 150°C oven for two hours (resulting in ~9% loss of mass due to water evaporation) prior to submerging it in 3 mL triethylamine. 9% (by weight) LiCl in dimethylacetamide (DMAc) was made by adding 1.68 g LiCl into 20 mL DMAc (18.74 g), and 10 mL of this was added to paper while stirring. To the other 10 mL of LiCl/DMAc, 4-Toluenesulfonyl chloride (TsCl, 1.7 g, 8.9 mmol) was added, and this solution was added to the paper mixture dropwise while stirring. The mixture was then allowed to stir at room temperature, covered, for 24-36 hours (mixture became brown and turbid), to give Tosyl-paper, which was yellowish. The paper was then washed on a Büchner funnel sequentially with water, ethanol, and acetone, and dried *in vacuo* overnight.

Amine-Paper

Tosyl-Paper was submerged in 50 mL DMSO and 0.875 mL 1,2-diaminoethane (0.79 g, 13 mmol) and refluxed at 100°C for 24 hours, yielding Amine-Paper, which was white. The paper was then washed on a Büchner funnel sequentially with tetrahydrofuran and EtOH, and dried *in vacuo* overnight. A second wash was conducted by shaking the paper in DMSO for 10 minutes on a vortexer, rinsing with acetone on a Büchner funnel, followed by drying.

TCO-Paper and TCO-PEG-Paper

TCO-succinimidyl ester (TCO-NHS; Chapter 2, compound 5; synthesized as described previously [5]) and TCO-PEG4-NHS (Click Chemistry Tools, Scottsdale, AZ, USA) solutions were prepared for reaction with Amine-Paper. 2 mg (0.0039 mmol) of TCO-PEG4-NHS in 389 μL of DMSO and 2.28 mg (.00853 mmol) of TCO-NHS in 853 μL of DMSO yielded 10 mM stock solutions. Amine-paper was submerged in 5% (by volume) triethylamine in DMSO (TEA), then TCO-NHS or TCO-PEG4-NHS (TCO) stock solutions were added for a final ratio of 1:2 TCO:TEA. The resulting mixtures were gently tumbled at room temperature for 30 minutes to yield TCO-Paper and TCO-PEG-Paper. The papers were then washed with DMSO, EtOH and acetone, and dried *in vacuo*.

5.3.3. Characterization of Amine-Paper

For ninhydrin test, 1.5 μL of 2% ninhydrin solution was spotted onto a 4 mm-diameter circle of washed Amine-Paper or control unmodified Whatman #4 paper, followed by drying in a 150°C oven for 10 minutes. For N-hydroxysuccinimide coupling test, Bodipy 650/665-X, SE (Thermo Fisher Scientific, Waltham, MA, USA) was prepared as a 10 mM stock in DMSO, and then combined 1:2 by volume with 5% (by volume) triethylamine in DMSO. 1.5 μL of dye solution was spotted onto a 4 mm-diameter circle of washed Amine-Paper or control unmodified Whatman #4 paper and allowed to sit for 15 minutes. The paper was then washed by shaking submerged in DMSO. Results were photographed with a DSLR camera under ambient light for visual readout or under a UV lamp at 365-nm irradiation for fluorescence images.

5.3.4. Testing and imaging of TCO-Paper using dyes

Bodipy FL-Tz, synthesized as described earlier[202], and Texas Red-Tz (**2.8**) were prepared as 5 mM stocks in DMSO, and then combined 3:1 with water for final 3.75 mM dye in 75% DMSO / 25% H_2O. 1.5 µL of dye solution was spotted onto a 4 mm-diameter circle of washed TCO-PEG-Paper, TCO-Paper or control unmodified Whatman #4 paper. The paper was immediately washed for 10-20 minutes by shaking submerged in 75% DMSO / 25% H_2O. Results were photographed with a DSLR camera under ambient light for visual readout or under a UV lamp at 365-nm irradiation for fluorescence images.

5.3.5. Printing and characterizing paper devices

Designs were made in Adobe Illustrator (Adobe, San Jose, CA, USA) and devices were printed using Yellow, Cyan, Magenta, and/or Black wax inks on a Xerox Phaser 8560 wax printer (both Xerox Corporation, Norwalk, CT, USA). The wax was then melted into the paper on a hot plate to create hydrophobic barriers as described previously[159]. Papers were cut with scissors or with biopsy punch (Miltex, York, PA, USA). Solvents were introduced to the paper devices either by direct pipetting or by using a soaked cigarette filter (Premier brand filter tips) as the source. The wax channels were testing on 1 Chr paper against several hydrophobic solvents: EtOH, CH_3OH, DMSO, and DMF, by adding 15 µL each to the end of wax-printed channels.

5.3.6. Lateral flow test

1 μL of 125 μM Texas Red-Tz or 1 μL of 125 μM Texas Red-Tz and 1 μL of 63 μM ^{19}F-TCO were spotted onto wax-printed paper devices on which a 4-mm hole had been punched out with a biopsy punch and replaced with a 4-mm circle of TCO-Paper*. The channel portion of the device was suspended over a petri dish by using pieces of plastic (cut Disposable Micro Slides; VWR International, Radnor, PA, USA) as raisers around the edge of the paper, glued with rubber cement. An additional piece of plastic was placed over the TCO-Paper circle to hold it in place and attached to the waxed portions of the device using rubber cement. (See Appendix C for front and back view of device.) 75% DMSO in water was introduced to the device by placing a soaked cigarette filter at the top, and it was allowed to flow through the channel until the solvent front reached the end of the device. The device was then imaged on an Olympus OV110 imaging system (Olympus America) using brightfield and RFP imaging channels.

*TCO-Paper for this experiment was acquired using a different synthetic approach than described above (somewhere deep in the lab notebooks of Thomas Reiner), and was adapted from previously published literature[203].

5.4. Discussion and Conclusions

Herein we show that we can perform cellulose chemistry on commercially available sheets of paper, including synthesizing clickable TCO-Paper. We then validated the chemistry using reactive dyes and performed click chemistry reactions in paper-based microfluidics lateral flow format. TCO-Paper has several potential applications, owing to

its bioorthogonal, highly specific, and extremely fast reaction speed with Tz-functionalized molecules. These include precise patterning of paper with biomolecules (including small molecules with Tz moieties) for detection or cell experiments (e.g. chemoattractants), as well as cheaper companion diagnostics tests.

One potential approach is to perform a competitive binding assay in which a clickable version of a drug (say, Ibrutinib-TCO) reacts with and blocks binding of a clickable dye (say, Texas Red-Tz) to a TCO spot in a lateral flow test. The amount of Texas Red in the binding spot would be inversely correlated with the amount of Ibrutinib-TCO. The amount of Ibrutinib-TCO available for the blocking would depend on the assay design, but could depend on either BTK target abundance or blocking of BTK target by unlabeled drug (e.g. occupancy test). Similar work was previously done using a nanoparticle-based approach[204]. The design of a dual-moiety clickable/fluorescent ligand would also be possible depending on the application. Visible or turn-on probes could cheapen this type of test so that a microscope is not needed for detection; alternatively, new technologies, such as portable fluorescence microscope could lower the cost of readout.

Overall, the ability to perform chemical assays on paper could lower the cost and increase the portability of drug sensitivity, compliance, and efficacy screening for resource-poor settings and home healthcare, bringing more complex diagnostics to the point-of-care.

Chapter 6.

Conclusion

BTK imaging with Ibrutinib-BFL and microfluidics-enabled CNS lymphoma profiling were technologies developed in parallel, as applications of effective, novel companion diagnostic approaches for B-cell lymphomas, but their potential intersection may be particularly beneficial for improving clinical trials and patient care. Since it is currently difficult in the clinic to determine which patients are at risk for CNS involvement, it is in standard practice to protect against it with prophylactic intrathecal injections of chemotherapy drugs, typically methotrexate[205]. While methotrexate has been used for decades, a recent clinical trial evaluated the efficacy of intrathecal Rituximab as a novel alternative[206]. To evaluate these therapeutics and still-newer drugs like BTK inhibitors, we can expand upon the use of the technologies developed herein.

We have already shown that the microfluidic chip can be potentially useful in drug imaging; it also has possible applications for on-chip drug screening and pharmacodynamic testing. This can include correlating dose and cell death, testing cell uptake of nanoparticle-carried drugs, screening for drug resistance (e.g. for resistance to covalent BTK inhibitor binding[207]), evaluating combinations of drugs, and plotting drug uptake and effects across populations of cells to look at cell-to-cell heterogeneity[83]. These studies are not limited to CNS lymphoma, and on chip drug imaging could be a useful tool for investigating biomarkers and target engagement for other suspension cell populations. The discrete cell capture sites provide a convenient platform for large-scale

image analysis and single cells can be imaged over time, thus providing better benchmarks for drug efficacy in lymphoma subtypes[13].

Additionally, drug-based imaging agents may be useful for targeted CNS lymphoma PET. Ibrutinib's consistently strong performance thus far in clinical trials for other B-cell malignancies [208], as well as previous cell studies of sensitivity to BTK inhibition, suggest that it is likely to be found to be effective for treating ABC-type DLBCLs[14]. Since the ABC molecular signature is a hallmark of primary CNS lymphomas, Ibrutinib may indeed emerge as a potential therapeutic for delivery by intrathecal injection or perhaps a nanoparticle formulation to bypass the blood-brain-barrier (BBB). Using new mouse models of CNS lymphoma[209], it may be possible to test targeted PET imaging across the BBB using an Ibrutinib probe. Although Ibrutinib-BFL is unlikely to be BBB-permeable, perhaps a two-step click chemistry approach would allow for imaging. Recently, it was shown that ^{18}F-TCO can be delivered to the brain[210]. It is therefore reasonable that following intrathecal administration of Ibrutinib-Tz to lymphoma cells in the CNS, uptake and drug levels could be measured at various time-points using ^{18}F-TCO delivered intravenously via PET imaging. This approach for tracking novel intrathecal treatments non-invasively could be expanded to additional CNS lymphoma therapeutics or other non-therapeutic targeted imaging agents.

In all, targeted companion diagnostics and B-cell lymphoma treatment profiling either *in vitro* or through imaging will improve our understanding of drug efficacy across therapeutic classes and specific patient subgroups, enabling effective drug development and personalized, precise treatment strategies for these diseases.

References

1. Hay, M., Thomas, D. W., Craighead, J. L., Economides, C. & Rosenthal, J. Clinical development success rates for investigational drugs. *Nat Biotechnol* **32**, 40-51 (2014).

2. Simon, G. M., Niphakis, M. J. & Cravatt, B. F. Determining target engagement in living systems. *Nat Chem Biol* **9**, 200-205 (2013).

3. Weissleder, R. & Pittet, M. J. Imaging in the era of molecular oncology. *Nature* **452**, 580-589 (2008).

4. Devaraj, N. K., Keliher, E. J., Thurber, G. M., Nahrendorf, M. & Weissleder, R. 18F labeled nanoparticles for in vivo PET-CT imaging. *Bioconjug Chem* **20**, 397-401 (2009).

5. Devaraj, N. K., Upadhyay, R., Haun, J. B., Hilderbrand, S. A. & Weissleder, R. Fast and sensitive pretargeted labeling of cancer cells through a tetrazine/trans-cyclooctene cycloaddition. *Angew Chem Int Ed Engl* **48**, 7013-7016 (2009).

6. Nahrendorf, M. et al. Hybrid PET-optical imaging using targeted probes. *Proc Natl Acad Sci U S A* **107**, 7910-7915 (2010).

7. Pittet, M. J. & Weissleder, R. Intravital imaging. *Cell* **147**, 983-991 (2011).

8. Nagrath, S. et al. Isolation of rare circulating tumour cells in cancer patients by microchip technology. *Nature* **450**, 1235-1239 (2007).

9. Chung, J. et al. Microfluidic cell sorter (muFCS) for on-chip capture and analysis of single cells. *Adv Healthc Mater* **1**, 432-436 (2012).

10. Peterson, V. M. et al. Ascites analysis by a microfluidic chip allows tumor-cell profiling. *Proc Natl Acad Sci U S A* **110**, E4978-E4986 (2013).

11. Chung, J. et al. Rare cell isolation and profiling on a hybrid magnetic/size-sorting chip. *Biomicrofluidics* **7**, 54107 (2013).

12. Alizadeh, A. A. et al. Distinct types of diffuse large B-cell lymphoma identified by gene expression profiling. *Nature* **403**, 503-511 (2000).

13. Younes, A. & Berry, D. A. From drug discovery to biomarker-driven clinical trials in lymphoma. *Nat Rev Clin Oncol* **9**, 643-653 (2012).

14. Young, R. M. & Staudt, L. M. Targeting pathological B cell receptor signalling in lymphoid malignancies. *Nat Rev Drug Discov* **12**, 229-243 (2013).

15. Lenz, G. et al. Molecular subtypes of diffuse large B-cell lymphoma arise by distinct genetic pathways. *Proc Natl Acad Sci U S A* **105**, 13520-13525 (2008).

16. Wright, G. et al. A gene expression-based method to diagnose clinically distinct subgroups of diffuse large B cell lymphoma. *Proc Natl Acad Sci U S A* **100**, 9991-9996 (2003).

17. Bogusz, A. M. et al. Quantitative immunofluorescence reveals the signature of active B-cell receptor signaling in diffuse large B-cell lymphoma. *Clin Cancer Res* **18**, 6122-6135 (2012).

18. Rickert, R. C. New insights into pre-BCR and BCR signalling with relevance to B cell malignancies. *Nat Rev Immunol* **13**, 578-591 (2013).

19. Advani, R. H. et al. Bruton tyrosine kinase inhibitor ibrutinib (PCI-32765) has significant activity in patients with relapsed/refractory B-cell malignancies. *J Clin Oncol* **31**, 88-94 (2013).

20. Rushworth, S. A., Murray, M. Y., Zaitseva, L., Bowles, K. M. & Macewan, D. J. Identification of Bruton's tyrosine kinase as a therapeutic target in acute myeloid leukemia. *Blood* **123,** 1229-1238 (2014).

21. Byrd, J. C. et al. Targeting BTK with ibrutinib in relapsed chronic lymphocytic leukemia. *N Engl J Med* **369**, 32-42 (2013).

22. Wang, M. L. et al. Targeting BTK with ibrutinib in relapsed or refractory mantle-cell lymphoma. *N Engl J Med* **369**, 507-516 (2013).

23. Honigberg, L. A. et al. The Bruton tyrosine kinase inhibitor PCI-32765 blocks B-cell activation and is efficacious in models of autoimmune disease and B-cell malignancy. *Proc Natl Acad Sci U S A* **107**, 13075-13080 (2010).

24. Martinez, A. W. et al. Simple telemedicine for developing regions: camera phones and paper-based microfluidic devices for real-time, off-site diagnosis. *Anal Chem* **80**, 3699-3707 (2008).

25. Pollock, N. R. et al. A paper-based multiplexed transaminase test for low-cost, point-of-care liver function testing. *Sci Transl Med* **4**, 152ra129 (2012).

26. Pollock, N. R. et al. Field evaluation of a prototype paper-based point-of-care fingerstick transaminase test. *PLoS One* **8**, e75616 (2013).

27. El-Khamisy, S. F., Masutani, M., Suzuki, H. & Caldecott, K. W. A requirement for PARP-1 for the assembly or stability of XRCC1 nuclear foci at sites of oxidative DNA damage. *Nucleic Acids Res* **31**, 5526-5533 (2003).

28. Rouleau, M., Patel, A., Hendzel, M. J., Kaufmann, S. H. & Poirier, G. G. PARP inhibition: PARP1 and beyond. *Nat Rev Cancer* **10**, 293-301 (2010).

29. Ratnam, K. & Low, J. A. Current development of clinical inhibitors of poly(ADP-ribose) polymerase in oncology. *Clin Cancer Res* **13**, 1383-1388 (2007).

30. Comen, E. A. & Robson, M. Inhibition of poly(ADP)-ribose polymerase as a therapeutic strategy for breast cancer. *Oncology (Williston Park)* **24**, 55-62 (2010).

31. Ferraris, D. V. Evolution of poly(ADP-ribose) polymerase-1 (PARP-1) inhibitors. From concept to clinic. *J Med Chem* **53**, 4561-4584 (2010).

32. Menear, K. A. et al. 4-[3-(4-cyclopropanecarbonylpiperazine-1-carbonyl)-4-fluorobenzyl]-2H-phthalazin- 1-one: a novel bioavailable inhibitor of poly(ADP-ribose) polymerase-1. *J Med Chem* **51**, 6581-6591 (2008).

33. Devaraj, N. K., Weissleder, R. & Hilderbrand, S. A. Tetrazine-based cycloadditions: application to pretargeted live cell imaging. *Bioconjug Chem* **19**, 2297-2299 (2008).

34. Devaraj, N. K., Hilderbrand, S., Upadhyay, R., Mazitschek, R. & Weissleder, R. Bioorthogonal turn-on probes for imaging small molecules inside living cells. *Angew Chem Int Ed Engl* **49**, 2869-2872 (2010).

35. Royzen, M., Yap, G. P. & Fox, J. M. A photochemical synthesis of functionalized trans-cyclooctenes driven by metal complexation. *J Am Chem Soc* **130**, 3760-3761 (2008).

36. Meder, V. S., Boeglin, M., de Murcia, G. & Schreiber, V. PARP-1 and PARP-2 interact with nucleophosmin/B23 and accumulate in transcriptionally active nucleoli. *J Cell Sci* **118**, 211-222 (2005).

37. Haince, J. F. et al. PARP1-dependent kinetics of recruitment of MRE11 and NBS1 proteins to multiple DNA damage sites. *J Biol Chem* **283**, 1197-1208 (2008).

38. Carpenter, A. E. et al. CellProfiler: image analysis software for identifying and quantifying cell phenotypes. *Genome Biol* **7**, R100 (2006).

39. Malpica, N. et al. Applying watershed algorithms to the segmentation of clustered nuclei. *Cytometry* **28**, 289-297 (1997).

40. Wu, A. M. et al. High-resolution microPET imaging of carcinoembryonic antigen-positive xenografts by using a copper-64-labeled engineered antibody fragment. *Proc Natl Acad Sci U S A* **97**, 8495-8500 (2000).

41. Avril, N. et al. Breast imaging with positron emission tomography and fluorine-18 fluorodeoxyglucose: use and limitations. *J Clin Oncol* **18**, 3495-3502 (2000).

42. Gambhir, S. S. Molecular imaging of cancer with positron emission tomography. *Nat Rev Cancer* **2**, 683-693 (2002).

43. Klimas, M. T. Positron emission tomography and drug discovery: contributions to the understanding of pharmacokinetics, mechanism of action and disease state characterization. *Mol Imaging Biol* **4**, 311-337 (2002).

44. Nahrendorf, M. et al. Nanoparticle PET-CT imaging of macrophages in inflammatory atherosclerosis. *Circulation* **117**, 379-387 (2008).

45. Burns, H. D. et al. [18F]MK-9470, a positron emission tomography (PET) tracer for in vivo human PET brain imaging of the cannabinoid-1 receptor. *Proc Natl Acad Sci U S A* **104**, 9800-9805 (2007).

46. Willmann, J. K., van Bruggen, N., Dinkelborg, L. M. & Gambhir, S. S. Molecular imaging in drug development. *Nat Rev Drug Discov* **7**, 591-607 (2008).

47. Lee, C. C. et al. Multistep synthesis of a radiolabeled imaging probe using integrated microfluidics. *Science* **310**, 1793-1796 (2005).

48. Kolb, H. C., Finn, M. G. & Sharpless, K. B. Click Chemistry: Diverse Chemical Function from a Few Good Reactions. *Angew Chem Int Ed Engl* **40**, 2004-2021 (2001).

49. Demko, Z. P. & Sharpless, K. B. A click chemistry approach to tetrazoles by Huisgen 1,3-dipolar cycloaddition: synthesis of 5-sulfonyl tetrazoles from azides and sulfonyl cyanides. *Angew Chem Int Ed Engl* **41**, 2110-2113 (2002).

50. Agard, N. J., Prescher, J. A. & Bertozzi, C. R. A strain-promoted [3 + 2] azide-alkyne cycloaddition for covalent modification of biomolecules in living systems. *J Am Chem Soc* **126**, 15046-15047 (2004).

51. Baskin, J. M. et al. Copper-free click chemistry for dynamic in vivo imaging. *Proc Natl Acad Sci U S A* **104**, 16793-16797 (2007).

52. Chang, P. V. et al. Copper-free click chemistry in living animals. *Proc Natl Acad Sci U S A* **107**, 1821-1826 (2010).

53. Sun, E. Y., Josephson, L. & Weissleder, R. “Clickable” nanoparticles for targeted imaging. *Mol Imaging* **5**, 122-128 (2006).

54. Nahrendorf, M. et al. 18F-4V for PET-CT imaging of VCAM-1 expression in atherosclerosis. *JACC Cardiovasc Imaging* **2**, 1213-1222 (2009).

55. Li, Z. B., Wu, Z., Chen, K., Chin, F. T. & Chen, X. Click chemistry for (18)F-labeling of RGD peptides and microPET imaging of tumor integrin alphavbeta3 expression. *Bioconjug Chem* **18**, 1987-1994 (2007).

56. Reiner, T., Earley, S., Turetsky, A. & Weissleder, R. Bioorthogonal small-molecule ligands for PARP1 imaging in living cells. *Chembiochem* **11**, 2374-2377 (2010).

57. Fong, P. C. et al. Inhibition of poly(ADP-ribose) polymerase in tumors from BRCA mutation carriers. *N Engl J Med* **361**, 123-134 (2009).

58. Closson, W. D. & Kwiatkowski, G. T. Solvolysis of exo and endo-cis-bicyclo [3.3. 0] oct-2-yl and cis-4-cycloocten-1-yl toluenesulfonates. *Tetrahedron Letters* **7**, 6435–6440 (1966).

59. Reiner, T., Keliher, E. J., Earley, S., Marinelli, B. & Weissleder, R. Synthesis and in vivo imaging of a 18F-labeled PARP1 inhibitor using a chemically orthogonal scavenger-assisted high-performance method. *Angew Chem Int Ed Engl* **50**, 1922-1925 (2011).

60. Reiner, T. et al. Imaging therapeutic PARP inhibition in vivo through bioorthogonally developed companion imaging agents. *Neoplasia* **14**, 169-177 (2012).

61. Thurber, G. M. et al. Single-cell and subcellular pharmacokinetic imaging allows insight into drug action in vivo. *Nat Commun* **4**, 1504 (2013).

62. Hendricks, J. A. et al. Synthesis of [18F]BODIPY: bifunctional reporter for hybrid optical/positron emission tomography imaging. *Angew Chem Int Ed Engl* **51**, 4603-4606 (2012).

63. Keliher, E. J., Klubnick, J. A., Reiner, T., Mazitschek, R. & Weissleder, R. Efficient Acid-Catalyzed F/ F Fluoride Exchange of BODIPY Dyes. *ChemMedChem* (2014). doi: 10.1002/cmdc.201300506

64. Vetrie, D. et al. The gene involved in X-linked agammaglobulinaemia is a member of the src family of protein-tyrosine kinases. *Nature* **361**, 226-233 (1993).

65. Tsukada, S. et al. Deficient expression of a B cell cytoplasmic tyrosine kinase in human X-linked agammaglobulinemia. *Cell* **72**, 279-290 (1993).

66. Mangla, A. et al. Pleiotropic consequences of Bruton tyrosine kinase deficiency in myeloid lineages lead to poor inflammatory responses. *Blood* **104**, 1191-1197 (2004).

67. Eifert, C. et al. A novel isoform of the B cell tyrosine kinase BTK protects breast cancer cells from apoptosis. *Genes Chromosomes Cancer* **52**, 961-975 (2013).

68. Rawlings, D. J. et al. Mutation of unique region of Bruton's tyrosine kinase in immunodeficient XID mice. *Science* **261**, 358-361 (1993).

69. de Weers, M. et al. B-cell antigen receptor stimulation activates the human Bruton's tyrosine kinase, which is deficient in X-linked agammaglobulinemia. *J Biol Chem* **269**, 23857-23860 (1994).

70. Fruman, D. A. et al. Phosphoinositide 3-kinase and Bruton's tyrosine kinase regulate overlapping sets of genes in B lymphocytes. *Proc Natl Acad Sci U S A* **99**, 359-364 (2002).

71. Mahajan, S. et al. Transcription factor STAT5A is a substrate of Bruton's tyrosine kinase in B cells. *J Biol Chem* **276**, 31216-31228 (2001).

72. Petro, J. B., Rahman, S. M., Ballard, D. W. & Khan, W. N. Bruton's tyrosine kinase is required for activation of IkappaB kinase and nuclear factor kappaB in response to B cell receptor engagement. *J Exp Med* **191**, 1745-1754 (2000).

73. Bajpai, U. D., Zhang, K., Teutsch, M., Sen, R. & Wortis, H. H. Bruton's tyrosine kinase links the B cell receptor to nuclear factor kappaB activation. *J Exp Med* **191**, 1735-1744 (2000).

74. Tai, Y. T. et al. Bruton tyrosine kinase inhibition is a novel therapeutic strategy targeting tumor in the bone marrow microenvironment in multiple myeloma. *Blood* **120**, 1877-1887 (2012).

75. Woyach, J. A. et al. Bruton's tyrosine kinase (BTK) function is important to the development and expansion of chronic lymphocytic leukemia (CLL). *Blood* **123**, 1207-1213 (2013).

76. Cinar, M. et al. Bruton tyrosine kinase is commonly overexpressed in mantle cell lymphoma and its attenuation by Ibrutinib induces apoptosis. *Leuk Res* **37**, 1271-1277 (2013).

77. O'Brien, S. et al. Ibrutinib as initial therapy for elderly patients with chronic lymphocytic leukaemia or small lymphocytic lymphoma: an open-label, multicentre, phase 1b/2 trial. *Lancet Oncol* **15**, 48-58 (2014).

78. Evans, E. K. et al. Inhibition of Btk with CC-292 provides early pharmacodynamic assessment of activity in mice and humans. *J Pharmacol Exp Ther* **346**, 219-228 (2013).

79. Liu, Q. et al. Developing irreversible inhibitors of the protein kinase cysteinome. *Chem Biol* **20**, 146-159 (2013).

80. Lou, Y., Owens, T. D., Kuglstatter, A., Kondru, R. K. & Goldstein, D. M. Bruton's tyrosine kinase inhibitors: approaches to potent and selective inhibition, preclinical and clinical

evaluation for inflammatory diseases and B cell malignancies. *J Med Chem* **55**, 4539-4550 (2012).

81. Pan, Z. et al. Discovery of selective irreversible inhibitors for Bruton's tyrosine kinase. *ChemMedChem* **2**, 58-61 (2007).

82. Akinleye, A., Chen, Y., Mukhi, N., Song, Y. & Liu, D. Ibrutinib and novel BTK inhibitors in clinical development. *J Hematol Oncol* **6**, 59 (2013).

83. Fallahi-Sichani, M., Honarnejad, S., Heiser, L. M., Gray, J. W. & Sorger, P. K. Metrics other than potency reveal systematic variation in responses to cancer drugs. *Nat Chem Biol* **9**, 708-714 (2013).

84. Orth, J. D. et al. Analysis of mitosis and antimitotic drug responses in tumors by in vivo microscopy and single-cell pharmacodynamics. *Cancer Res* **71**, 4608-4616 (2011).

85. Strijbis, K. et al. Bruton's Tyrosine Kinase (BTK) and Vav1 contribute to Dectin1-dependent phagocytosis of Candida albicans in macrophages. *PLoS Pathog* **9**, e1003446 (2013).

86. Davis, R. E. et al. Chronic active B-cell-receptor signalling in diffuse large B-cell lymphoma. *Nature* **463**, 88-92 (2010).

87. Mohamed, A. J. et al. Nucleocytoplasmic shuttling of Bruton's tyrosine kinase. *J Biol Chem* **275**, 40614-40619 (2000).

88. Lowry, W. E. & Huang, X. Y. G Protein beta gamma subunits act on the catalytic domain to stimulate Bruton's agammaglobulinemia tyrosine kinase. *J Biol Chem* **277**, 1488-1492 (2002).

89. Gustafsson, M. O. et al. Regulation of nucleocytoplasmic shuttling of Bruton's tyrosine kinase (Btk) through a novel SH3-dependent interaction with ankyrin repeat domain 54 (ANKRD54). *Mol Cell Biol* **32**, 2440-2453 (2012).

90. Su, Q., Zhou, Y. & Johns, R. A. Bruton's tyrosine kinase (BTK) is a binding partner for hypoxia induced mitogenic factor (HIMF/FIZZ1) and mediates myeloid cell chemotaxis. *FASEB J* **21**, 1376-1382 (2007).

91. Dragoi, A. M., Talman, A. M. & Agaisse, H. Bruton's tyrosine kinase regulates Shigella flexneri dissemination in HT-29 intestinal cells. *Infect Immun* **81**, 598-607 (2013).

92. Keliher, E. J., Reiner, T., Turetsky, A., Hilderbrand, S. A. & Weissleder, R. High-yielding, two-step 18F labeling strategy for 18F-PARP1 inhibitors. *ChemMedChem* **6**, 424-427 (2011).

93. Reiner, T., Keliher, E. J., Earley, S., Marinelli, B. & Weissleder, R. Synthesis and in vivo imaging of a 18F-labeled PARP1 inhibitor using a chemically orthogonal scavenger-assisted high-performance method. *Angew Chem Int Ed Engl* **50**, 1922-1925 (2011).

94. Zeglis, B. M. et al. A pretargeted PET imaging strategy based on bioorthogonal Diels-Alder click chemistry. *J Nucl Med* **54**, 1389-1396 (2013).

95. Borjesson, P. K. et al. Radiation dosimetry of 89Zr-labeled chimeric monoclonal antibody U36 as used for immuno-PET in head and neck cancer patients. *J Nucl Med* **50**, 1828-1836 (2009).

96. Holland, J. P. et al. 89Zr-DFO-J591 for immunoPET of prostate-specific membrane antigen expression in vivo. *J Nucl Med* **51**, 1293-1300 (2010).

97. Keliher, E. J. et al. 89Zr-labeled dextran nanoparticles allow in vivo macrophage imaging. *Bioconjug Chem* **22**, 2383-2389 (2011).

98. Natarajan, A., Habte, F. & Gambhir, S. S. Development of a Novel Long-Lived ImmunoPET Tracer for Monitoring Lymphoma Therapy in a Humanized Transgenic Mouse Model. *Bioconjug Chem* **23**, 1221-1229 (2012).

99. Fischer, G., Seibold, U., Schirrmacher, R., Wangler, B. & Wangler, C. (89)Zr, a radiometal nuclide with high potential for molecular imaging with PET: chemistry, applications and remaining challenges. *Molecules* **18**, 6469-6490 (2013).

100. Kerns, H. M. et al. B cell-specific lentiviral gene therapy leads to sustained B-cell functional recovery in a murine model of X-linked agammaglobulinemia. *Blood* **115**, 2146-2155 (2010).

101. Dubach, J. M. et al. In vivo imaging of specific drug-target binding at subcellular resolution. *Nat Commun* **5**, 3946 (2014).

102. Aalipour, A. & Advani, R. H. Bruton tyrosine kinase inhibitors: a promising novel targeted treatment for B cell lymphomas. *Br J Haematol* **163**, 436-443 (2013).

103. Walter, A. O. et al. Discovery of a mutant-selective covalent inhibitor of EGFR that overcomes T790M-mediated resistance in NSCLC. *Cancer Discov* **3**, 1404-1415 (2013).

104. Schabet, M. Epidemiology of primary CNS lymphoma. *J Neurooncol* **43**, 199-201 (1999).

105. Villano, J. L., Koshy, M., Shaikh, H., Dolecek, T. A. & McCarthy, B. J. Age, gender, and racial differences in incidence and survival in primary CNS lymphoma. *Br J Cancer* **105**, 1414-1418 (2011).

106. Ziegler, J. L., Bluming, A. Z., Morrow, R. H., Fass, L. & Carbone, P. P. Central nervous system involvement in Burkitt's lymphoma. *Blood* **36**, 718-728 (1970).

107. Liang, R., Chiu, E. & Loke, S. L. Secondary central nervous system involvement by non-Hodgkin's lymphoma: the risk factors. *Hematol Oncol* **8**, 141-145 (1990).

108. Quijano, S. et al. Identification of leptomeningeal disease in aggressive B-cell non-Hodgkin's lymphoma: improved sensitivity of flow cytometry. *J Clin Oncol* **27**, 1462-1469 (2009).

109. Gill, S. et al. Mantle cell lymphoma with central nervous system involvement: frequency and clinical features. *Br J Haematol* **147**, 83-88 (2009).

110. van Besien, K. et al. Risk factors, treatment, and outcome of central nervous system recurrence in adults with intermediate-grade and immunoblastic lymphoma. *Blood* **91**, 1178-1184 (1998).

111. Rubenstein, J. L. et al. Gene expression and angiotropism in primary CNS lymphoma. *Blood* **107**, 3716-3723 (2006).

112. Dave, S. S. et al. Molecular diagnosis of Burkitt's lymphoma. *N Engl J Med* **354**, 2431-2442 (2006).

113. Lossos, I. S. & Morgensztern, D. Prognostic biomarkers in diffuse large B-cell lymphoma. *J Clin Oncol* **24**, 995-1007 (2006).

114. Bloomfield, I. G., Johnston, I. H. & Bilston, L. E. Effects of proteins, blood cells and glucose on the viscosity of cerebrospinal fluid. *Pediatr Neurosurg* **28**, 246-251 (1998).

115. de Graaf, M. T. et al. Central memory CD4+ T cells dominate the normal cerebrospinal fluid. *Cytometry B Clin Cytom* **80**, 43-50 (2011).

116. Weston, C. L., Glantz, M. J. & Connor, J. R. Detection of cancer cells in the cerebrospinal fluid: current methods and future directions. *Fluids Barriers CNS* **8**, 14 (2011).

117. Hegde, U. et al. High incidence of occult leptomeningeal disease detected by flow cytometry in newly diagnosed aggressive B-cell lymphomas at risk for central nervous system involvement: the role of flow cytometry versus cytology. *Blood* **105**, 496-502 (2005).

118. Schroers, R. et al. Diagnosis of leptomeningeal disease in diffuse large B-cell lymphomas of the central nervous system by flow cytometry and cytopathology. *Eur J Haematol* **85**, 520-528 (2010).

119. Ulrickson, M., Press, O. W. & Casper, C. Epidemiology, Diagnosis, and Treatment of HIV-Associated Non-Hodgkin Lymphoma in Resource-Limited Settings. *Adv Hematol* **2012**, 932658 (2012).

120. Peterson, V. M. et al. Ascites analysis by a microfluidic chip allows tumor-cell profiling. *Proc Natl Acad Sci U S A* **110**, E4978-E4986 (2013).

121. Dux, R. et al. A standardized protocol for flow cytometric analysis of cells isolated from cerebrospinal fluid. *J Neurol Sci* **121**, 74-78 (1994).

122. Kleine, T. O., Albrecht, J. & Zofel, P. Flow cytometry of cerebrospinal fluid (CSF) lymphocytes: alterations of blood/CSF ratios of lymphocyte subsets in inflammation disorders of human central nervous system (CNS). *Clin Chem Lab Med* **37**, 231-241 (1999).

123. Johnson, N. A. et al. Diffuse large B-cell lymphoma: reduced CD20 expression is associated with an inferior survival. *Blood* **113**, 3773-3780 (2009).

124. Hiraga, J. et al. Down-regulation of CD20 expression in B-cell lymphoma cells after treatment with rituximab-containing combination chemotherapies: its prevalence and clinical significance. *Blood* **113**, 4885-4893 (2009).

125. Miyoshi, H. et al. Comparison of CD20 expression in B-cell lymphoma between newly diagnosed, untreated cases and those after rituximab treatment. *Cancer Sci* **103**, 1567-1573 (2012).

126. Camilleri-Broet, S. et al. A uniform activated B-cell-like immunophenotype might explain the poor prognosis of primary central nervous system lymphomas: analysis of 83 cases. *Blood* **107**, 190-196 (2006).

127. Broyde, A. et al. Role and prognostic significance of the Ki-67 index in non-Hodgkin's lymphoma. *Am J Hematol* **84**, 338-343 (2009).

128. Turetsky, A., Kim, E., Kohler, R. H., Miller, M. A. & Weissleder, R. Single cell imaging of Bruton's tyrosine kinase using an irreversible inhibitor. *Sci Rep* **4**, 4782 (2014).

129. Rahal, R. et al. Pharmacological and genomic profiling identifies NF-kappaB-targeted treatment strategies for mantle cell lymphoma. *Nat Med* **20**, 87-92 (2014).

130. Ponader, S. & Burger, J. A. Bruton's Tyrosine Kinase: From X-Linked Agammaglobulinemia Toward Targeted Therapy for B-Cell Malignancies. *J Clin Oncol* **32**, 1830-1839 (2014).

131. Hans, C. P. et al. Confirmation of the molecular classification of diffuse large B-cell lymphoma by immunohistochemistry using a tissue microarray. *Blood* **103**, 275-282 (2004).

132. Abrey, L. E. et al. Report of an international workshop to standardize baseline evaluation and response criteria for primary CNS lymphoma. *J Clin Oncol* **23**, 5034-5043 (2005).

133. Korfel, A. et al. Prognostic impact of meningeal dissemination in primary CNS lymphoma (PCNSL): experience from the G-PCNSL-SG1 trial. *Ann Oncol* **23**, 2374-2380 (2012).

134. Korfel, A. & Schlegel, U. Diagnosis and treatment of primary CNS lymphoma. *Nat Rev Neurol* **9**, 317-327 (2013).

135. Lossos, I. S. et al. Prediction of survival in diffuse large-B-cell lymphoma based on the expression of six genes. *N Engl J Med* **350**, 1828-1837 (2004).

136. Gurel, B. et al. Nuclear MYC protein overexpression is an early alteration in human prostate carcinogenesis. *Mod Pathol* **21**, 1156-1167 (2008).

137. Antonini, G. et al. Intrathecal anti-CD20 antibody: an effective and safe treatment for leptomeningeal lymphoma. *J Neurooncol* **81**, 197-199 (2007).

138. Younes, A. & Berry, D. A. From drug discovery to biomarker-driven clinical trials in lymphoma. *Nat Rev Clin Oncol* **9**, 643-653 (2012).

139. Wilson, W. H. et al. Detection and outcome of occult leptomeningeal disease in diffuse large B-cell lymphoma and Burkitt lymphoma. *Haematologica* (2014). doi: 10.3324/haematol.2013.101741

140. Fleuren, E. D. et al. Theranostic applications of antibodies in oncology. *Mol Oncol* **8**, 799-812 (2014).

141. Zong, C., Lu, S., Chapman, A. R. & Xie, X. S. Genome-wide detection of single-nucleotide and copy-number variations of a single human cell. *Science* **338**, 1622-1626 (2012).

142. Martinez, A. W., Phillips, S. T. & Whitesides, G. M. Three-dimensional microfluidic devices fabricated in layered paper and tape. *Proc Natl Acad Sci U S A* **105**, 19606-19611 (2008).

143. Li, X., Ballerini, D. R. & Shen, W. A perspective on paper-based microfluidics: Current status and future trends. *Biomicrofluidics* **6**, 11301-1130113 (2012).

144. Ellerbee, A. K. et al. Quantifying colorimetric assays in paper-based microfluidic devices by measuring the transmission of light through paper. *Anal Chem* **81**, 8447-8452 (2009).

145. Martinez, A. W., Phillips, S. T., Whitesides, G. M. & Carrilho, E. Diagnostics for the developing world: microfluidic paper-based analytical devices. *Anal Chem* **82**, 3-10 (2010).

146. Schilling, K. M., Lepore, A. L., Kurian, J. A. & Martinez, A. W. Fully enclosed microfluidic paper-based analytical devices. *Anal Chem* **84**, 1579-1585 (2012).

147. Mao, X. & Huang, T. J. Microfluidic diagnostics for the developing world. *Lab Chip* **12**, 1412-1416 (2012).

148. Zhao, W., Ali, M. M., Aguirre, S. D., Brook, M. A. & Li, Y. Paper-based bioassays using gold nanoparticle colorimetric probes. *Anal Chem* **80**, 8431-8437 (2008).

149. Fu, E. et al. Enhanced sensitivity of lateral flow tests using a two-dimensional paper network format. *Anal Chem* **83**, 7941-7946 (2011).

150. Whitesides, G. M. The origins and the future of microfluidics. *Nature* **442**, 368-373 (2006).

151. Fu, E., Lutz, B., Kauffman, P. & Yager, P. Controlled reagent transport in disposable 2D paper networks. *Lab Chip* **10**, 918-920 (2010).

152. Osborn, J. L. et al. Microfluidics without pumps: reinventing the T-sensor and H-filter in paper networks. *Lab Chip* **10**, 2659-2665 (2010).

153. Kauffman, P., Fu, E., Lutz, B. & Yager, P. Visualization and measurement of flow in two-dimensional paper networks. *Lab Chip* **10**, 2614-2617 (2010).

154. Chitnis, G., Ding, Z., Chang, C. L., Savran, C. A. & Ziaie, B. Laser-treated hydrophobic paper: an inexpensive microfluidic platform. *Lab Chip* **11**, 1161-1165 (2011).

155. Lutz, B. R., Trinh, P., Ball, C., Fu, E. & Yager, P. Two-dimensional paper networks: programmable fluidic disconnects for multi-step processes in shaped paper. *Lab Chip* **11**, 4274-4278 (2011).

156. Fridley, G. E., Le, H. Q., Fu, E. & Yager, P. Controlled release of dry reagents in porous media for tunable temporal and spatial distribution upon rehydration. *Lab Chip* **12**, 4321-4327 (2012).

157. Lutz, B. et al. Dissolvable fluidic time delays for programming multi-step assays in instrument-free paper diagnostics. *Lab Chip* **13**, 2840-2847 (2013).

158. Toley, B. J. et al. Tunable-delay shunts for paper microfluidic devices. *Anal Chem* **85**, 11545-11552 (2013).

159. Carrilho, E., Martinez, A. W. & Whitesides, G. M. Understanding wax printing: a simple micropatterning process for paper-based microfluidics. *Anal Chem* **81**, 7091-7095 (2009).

160. Li, X., Tian, J. & Shen, W. Progress in patterned paper sizing for fabrication of paper-based microfluidic sensors. *Cellulose* **17**, 649-659 (2010).

161. Ge, L., Wang, S., Song, X., Ge, S. & Yu, J. 3D origami-based multifunction-integrated immunodevice: low-cost and multiplexed sandwich chemiluminescence immunoassay on microfluidic paper-based analytical device. *Lab Chip* **12**, 3150-3158 (2012).

162. Scida, K., Li, B., Ellington, A. D. & Crooks, R. M. DNA detection using origami paper analytical devices. *Anal Chem* **85**, 9713-9720 (2013).

163. Liu, W., Cassano, C. L., Xu, X. & Fan, Z. H. Laminated paper-based analytical devices (LPAD) with origami-enabled chemiluminescence immunoassay for cotinine detection in mouse serum. *Anal Chem* **85**, 10270-10276 (2013).

164. Chumo, B., Muluneh, M. & Issadore, D. Laser micromachined hybrid open/paper microfluidic chips. *Biomicrofluidics* **7**, 64109 (2013).

165. He, Q., Ma, C., Hu, X. & Chen, H. Method for fabrication of paper-based microfluidic devices by alkylsilane self-assembling and UV/O3-patterning. *Anal Chem* **85**, 1327-1331 (2013).

166. Zhang, Y. et al. Equipment-free quantitative measurement for microfluidic paper-based analytical devices fabricated using the principles of movable-type printing. *Anal Chem* **86**, 2005-2012 (2014).

167. Fang, X., Wei, S. & Kong, J. Paper-based microfluidics with high resolution, cut on a glass fiber membrane for bioassays. *Lab Chip* **14**, 911-915 (2014).

168. Delaney, J. L., Hogan, C. F., Tian, J. & Shen, W. Electrogenerated chemiluminescence detection in paper-based microfluidic sensors. *Anal Chem* **83**, 1300-1306 (2011).

169. Hu, C. et al. Inkjet printing of nanoporous gold electrode arrays on cellulose membranes for high-sensitive paper-like electrochemical oxygen sensors using ionic liquid electrolytes. *Anal Chem* **84**, 3745-3750 (2012).

170. Martinez, A. W. et al. Programmable diagnostic devices made from paper and tape. *Lab Chip* **10**, 2499-2504 (2010).

171. Fu, E. et al. Two-dimensional paper network format that enables simple multistep assays for use in low-resource settings in the context of malaria antigen detection. *Anal Chem* **84**, 4574-4579 (2012).

172. Jokerst, J. C. et al. Development of a paper-based analytical device for colorimetric detection of select foodborne pathogens. *Anal Chem* **84**, 2900-2907 (2012).

173. Vella, S. J. et al. Measuring markers of liver function using a micropatterned paper device designed for blood from a fingerstick. *Anal Chem* **84**, 2883-2891 (2012).

174. Taudte, R. V. et al. A portable explosive detector based on fluorescence quenching of pyrene deposited on coloured wax-printed muPADs. *Lab Chip* **13**, 4164-4172 (2013).

175. Weaver, A. A. et al. Paper analytical devices for fast field screening of beta lactam antibiotics and antituberculosis pharmaceuticals. *Anal Chem* **85**, 6453-6460 (2013).

176. Mani, V., Kadimisetty, K., Malla, S., Joshi, A. A. & Rusling, J. F. Paper-based electrochemiluminescent screening for genotoxic activity in the environment. *Environ Sci Technol* **47**, 1937-1944 (2013).

177. Park, T. S., Li, W., McCracken, K. E. & Yoon, J. Y. Smartphone quantifies Salmonella from paper microfluidics. *Lab Chip* **13**, 4832-4840 (2013).

178. Sechi, D., Greer, B., Johnson, J. & Hashemi, N. Three-dimensional paper-based microfluidic device for assays of protein and glucose in urine. *Anal Chem* **85**, 10733-10737 (2013).

179. Nie, Z. et al. Electrochemical sensing in paper-based microfluidic devices. *Lab Chip* **10**, 477-483 (2010).

180. Nie, Z., Deiss, F., Liu, X., Akbulut, O. & Whitesides, G. M. Integration of paper-based microfluidic devices with commercial electrochemical readers. *Lab Chip* **10**, 3163-3169 (2010).

181. Khan, M. S., Thouas, G., Shen, W., Whyte, G. & Garnier, G. Paper diagnostic for instantaneous blood typing. *Anal Chem* **82**, 4158-4164 (2010).

182. Cheng, C. M. et al. Paper-based ELISA. *Angew Chem Int Ed Engl* **49**, 4771-4774 (2010).

183. Klasner, S. A. et al. Paper-based microfluidic devices for analysis of clinically relevant analytes present in urine and saliva. *Anal Bioanal Chem* **397**, 1821-1829 (2010).

184. Dungchai, W., Chailapakul, O. & Henry, C. S. Use of multiple colorimetric indicators for paper-based microfluidic devices. *Anal Chim Acta* **674**, 227-233 (2010).

185. Thom, N. K., Yeung, K., Pillion, M. B. & Phillips, S. T. "Fluidic batteries" as low-cost sources of power in paper-based microfluidic devices. *Lab Chip* **12**, 1768-1770 (2012).

186. Araujo, A. C., Song, Y., Lundeberg, J., Stahl, P. L. & Brumer, H. Activated paper surfaces for the rapid hybridization of DNA through capillary transport. *Anal Chem* **84**, 3311-3317 (2012).

187. Zang, D., Ge, L., Yan, M., Song, X. & Yu, J. Electrochemical immunoassay on a 3D microfluidic paper-based device. *Chem Commun (Camb)* **48**, 4683-4685 (2012).

188. Lankelma, J., Nie, Z., Carrilho, E. & Whitesides, G. M. Paper-based analytical device for electrochemical flow-injection analysis of glucose in urine. *Anal Chem* **84**, 4147-4152 (2012).

189. Noor, M. O. & Krull, U. J. Paper-based solid-phase multiplexed nucleic acid hybridization assay with tunable dynamic range using immobilized quantum dots as donors in fluorescence resonance energy transfer. *Anal Chem* **85**, 7502-7511 (2013).

190. Noor, M. O., Shahmuradyan, A. & Krull, U. J. Paper-based solid-phase nucleic acid hybridization assay using immobilized quantum dots as donors in fluorescence resonance energy transfer. *Anal Chem* **85**, 1860-1867 (2013).

191. Mu, X., Zhang, L., Chang, S., Cui, W. & Zheng, Z. Multiplex Microfluidic Paper-based Immunoassay for the Diagnosis of Hepatitis C Virus Infection. *Anal Chem* **86**, 5338-5344 (2014).

192. Goldmann, A. S., Tischer, T., Barner, L., Bruns, M. & Barner-Kowollik, C. Mild and modular surface modification of cellulose via hetero Diels-Alder (HDA) cycloaddition. *Biomacromolecules* **12**, 1137-1145 (2011).

193. Tingaut, P., Hauert, R. & Zimmermann, T. Highly efficient and straightforward functionalization of cellulose films with thiol-ene click chemistry. *Journal of Materials Chemistry* **21**, 16066-16076 (2011).

194. Yu, A. et al. Biofunctional paper via the covalent modification of cellulose. *Langmuir* **28**, 11265-11273 (2012).

195. Evans, E., Gabriel, E. F., Coltro, W. K. & Garcia, C. D. Rational selection of substrates to improve color intensity and uniformity on microfluidic paper-based analytical devices. *Analyst* **139**, 2127-2132 (2014).

196. Fügedi, P., Nánási, P. & Szejtli, J. Synthesis of 6-*O*-α-D-glucopyranosylcyclomaltoheptaose. *Carbohydrate research* **175**, 173-181 (1988).

197. McCormick, C. L., Dawsey, T. R. & Newman, J. K. Competitive formation of cellulose *p*-toluenesulfonate and chlorodeoxycellulose during homogeneous reaction of *p*-toluenesulfonyl chloride with cellulose in *N*,*N*-dimethylacetamide-lithium chloride *Carbohydrate research* **208**, 183-191 (1990).

198. Tiller, J., Berlin, P. & Klemm, D. Soluble and film-forming cellulose derivatives with redox-chromogenic and enzyme immobilizing 1, 4-phenylenediamine groups. *Macromol Chem Phys* **200**, 1-9 (1999).

199. Heinze, T. & Liebert, T. Unconventional methods in cellulose functionalization. *Progress in Polymer Science* 2**6**, 1689-1762 (2001).

200. Liu, C. & Baumann, H. Exclusive and complete introduction of amino groups and their *N*-sulfo and *N*-carboxymethyl groups into the 6-position of cellulose without the use of protecting groups. *Carbohydrate research* **337**, 1297-1307 (2002).

201. Jung, A. & Berlin, P. New water-soluble and film-forming aminocellulose tosylates as enzyme support matrices with Cu2+-chelating properties. *Cellulose* **12**, 67-84 (2005).

202. Devaraj, N. K., Hilderbrand, S., Upadhyay, R., Mazitschek, R. & Weissleder, R. Bioorthogonal turn-on probes for imaging small molecules inside living cells. *Angew Chem Int Ed Engl* **49**, 2869-2872 (2010).

203. Ikeuchi, Y. et al. Amino acid-functionalized ethyl cellulose: Synthesis, characterization, and gas permeation properties. *J. Polym. Sci. A Polym. Chem.* **48**, 3986-3993 (2010).

204. Ullal, A. V. et al. Nanoparticle-mediated measurement of target-drug binding in cancer cells. *ACS Nano* **5**, 9216-9224 (2011).

205. Abramson, J. S. et al. Intravenous methotrexate as central nervous system (CNS) prophylaxis is associated with a low risk of CNS recurrence in high-risk patients with diffuse large B-cell lymphoma. *Cancer* **116**, 4283-4290 (2010).

206. Rubenstein, J. L. et al. Phase I study of intraventricular administration of rituximab in patients with recurrent CNS and intraocular lymphoma. *J Clin Oncol* **25**, 1350-1356 (2007).

207. Woyach, J. A. et al. Resistance Mechanisms for the Bruton's Tyrosine Kinase Inhibitor Ibrutinib. *N Engl J Med* **370**, 2286-2294 (2014).

208. Byrd, J. C. et al. Ibrutinib versus Ofatumumab in Previously Treated Chronic Lymphoid Leukemia. *N Engl J Med* (2014). doi: 10.1056/NEJMoa1400376

209. Gao, H.-X. et al. Novel Intracranial Xenografts Of CNS Lymphoma Implicate a Role For Cereblon As a Mediator Of Lenalidomide Efficacy. *Blood ASH* **122**, 374-374 (2013).

210. Wyffels, L. et al. In vivo evaluation of (18)F-labeled TCO for pre-targeted PET imaging in the brain. *Nucl Med Biol* **41**, 513-523 (2014).

Appendix A

Additional methods for Section 2.6

Compound name in Chapter 2	Compound name in Appendix A
2.10	**1**
2.11	**2**
2.12	**3**
2.13	**4**
2.14	**5**
2.15	**6**
2.3	**7**
2.16	**8**
2.17	**9**
2.18	**10**
2.19	**11**
2.20	**12**
2.21	**13**
2.22	**14**
2.23	**15**
2.24	**16**
2.25	**17**

Materials and Methods

Unless otherwise noted, all reagents were purchased from Sigma-Aldrich (St. Louis, MO) and used without further purification. Cyclohexylcarbodiimide polystyrene resin was purchased from EMD biosciences (Gibbstown, NJ). 4-[[4-Fluoro-3-(4-(5-oxopentanamide)piperazine-1-carbonyl) phenyl]methyl]-2H-phthalazin-1-one **7**[1], tetrazine amine **8** [2], and 4-[[4-fluoro-3-(piperazine-1-carbonyl)phenyl]methyl]-2H-phthalazin-1-one **11**[3]. were synthesized as described earlier. ^{18}F-Fluoride (n.c.a.) in ^{18}O-enriched water was purchased from PETNET (Woburn, MA). Automated synthesis of ^{18}F-labeled *trans*-cyclooctene was carried out using a Synthra RN Plus automated synthesizer (Synthra GmbH, Hamburg, Germany) operated by *SynthraView* software. For non-radioactive compounds, LC-ESI-MS analysis and HPLC-purifications were performed on a Waters (Milford, MA) LC-MS system. For LC-ESI-MS analyses, a Waters XTerra® C18 5 µm column was used. Preparative high performance liquid chromatography (HPLC) runs for synthetic intermediates utilized an Atlantis® Prep T3 OBD™ 5 µM column (eluents 0.1% TFA (v/v) in water and MeCN; gradient: 0-1.5 min, 5-100% B; 1.5-2.0 min 100% B). For radiolabeled compounds, preparative scale HPLC purification was achieved using a Machery-Nagel Nucleodur C18 Pyramid 250 × 10 mm Vario-Prep column (60:40 0.1% trifluoroacetic acid (v/v) in water-acetonitrile (MeCN) at 5.5 mL.min-1) with a 254 nm UV detector and radiodetector connected in series. Analytical HPLC of radiolabeled compounds was performed employing a Grace VYDAC (218TP510) C18 reversed-phase column (eluents 0.1% TFA (v/v) in water and MeCN; gradient: 0-17 min, 5-60% B; 17-21 min, 60-95% B; 21-24 min, 95% B;24-25 min, 95-5% B; 25-30 min, 5% B; 2 mL.min-1) with a dual-wavelength UV-vis detector and a flow-through gamma detector connected in series. HyperSep C18 cartridges were purchased from Thermo Electron (Bellefonte, PA) and Sep-pak VAC Alumina-N cartridges from Waters (Milford, MA). High-resolution electrospray ionization (ESI) mass spectra were obtained on a Bruker Daltonics APEXIV 4.7 Tesla Fourier Transform mass spectrometer (FT-ICR-MS) in the Department of Chemistry Instrumentation Facility at the Massachusetts Institute of Technology. IC_{50} assays were analyzed using a Tecan (Männedorf, Switzerland) Safire^2 microplate system. All kinetic data were analyzed using Prism 4 (GraphPad, La Jolla, CA) for Mac.

Synthesis.

(*Z*)-Cyclooct-4-enol (1). 9-Oxabicyclo[6.1.0]non-4-ene (4.2 g, 33.8 mmol) was added slowly to $LiAlH_4$ (1.2 g, 30.4 mmol) suspended in diethyl ether (100 mL). After stirring at room temperature for 4 h, the reaction was worked up by the sequential addition of 4 mL H_2O, 4 mL 25% $NaOH_{(aq)}$, and 4 mL of H_2O. The resulting mixture was filtered and the filtrate dried (Na_2SO_4) and filtered again. The clear ether solution was concentrated to give 4.1 g of (*Z*)-cyclooct-4-enol in 96.1% yield. ^{1}H NMR (400 MHz, $CDCl_3$) δ=5.75 – 5.64 (m, 1H), 5.59 (dt, *J* = 10.5, 7.9 Hz, 1H), 3.85 – 3.77 (m, 1H), 2.35 – 2.24 (m, 1H), 2.18 – 2.05 (m, 3H), 1.97 – 1.81 (m, 2H), 1.75 – 1.59 (m, 2H), 1.59 – 1.49 (m, 2H), 1.44 (bs, 1H) ppm.

(*Z*)-2-(Cyclooct-4-enyloxy)acetic acid (2). (*Z*)-Cyclooct-4-enol (2.0 g, 15.8 mmol) was added slowly to a suspension of sodium hydride (1.3 g of 60% dispersion in mineral oil, 31.7 mmol) in 50 mL THF. This was stirred at reflux for 1 h, then a solution of iodoacetic acid (2.9 g, 15.8 mmol) in 10 mL THF was added and reflux was continued for 4 h, then the reaction was cooled to room temperature and concentrated under reduced pressure. The residue was dissolved in 10% $NaOH_{(aq)}$ (50 mL) and extracted with Et_2O (2 x 25 mL). The pH of the aqueous solution was lowered to 4 by the addition of 6N HCl and extracted again with DCM (2 x 25 mL). Separately, the organic solutions were dried ($MgSO_4$), filtered, and concentrated by rotary evaporator. The ether extraction resulted in 1.0 g of starting (*Z*)-cyclooct-4-enol and the DCM extraction resulted in 1.9 g of (*Z*)-2-cyclooct-4-enyloxy)acetic acid **2** (65.5% yield). ^{1}H NMR (400 MHz, $CDCl_3$) δ=5.71 – 5.54 (m, 2H), 4.14 – 4.00 (m, 2H), 3.49 (dt, *J* = 9.2, 4.3 Hz, 1H), 2.42 – 2.29 (m, 1H), 2.21 – 1.92 (m, 4H), 1.82 (dt, *J* = 6.2, 4.0 Hz, 2H), 1.71 (tt, *J* = 12.4, 4.5 Hz, 1H), 1.62 – 1.51 (m, 1H), 1.47 – 1.34 (m, 1H) ppm; ^{13}C NMR (100 MHz, $CDCl_3$) δ=22.2, 25.6, 33.2, 65.3, 82.0, 129.6, 128.7, 175.5 ppm.

(*Z*)-2-(Cyclooct-4-enyloxy)ethanol (3). (*Z*)-2-Cyclooct-4-enyloxy)acetic acid (1.9 g, 10.3 mmol) was added to a suspension of $LiAlH_4$ (0.4 g, 9.5 mmol) in Et_2O (10 mL) at 0°C, warmed to room temperature, and was stirred for 24 h. Unreacted $LiAlH_4$ was quenched with 10% $HCl_{(aq)}$ and the reaction diluted with 30 mL H_2O. The Et_2O layer was separated and the aqueous solution was extracted with Et_2O (2 x10 mL). The combined Et_2O solutions were dried ($MgSO_4$), filtered, and concentrated. The crude mixture was subjected to column chromatography (2:3 hexanes:ethyl acetate) to give 1.4 g of (*Z*)-2-(cyclooct-4-enyloxy)ethanol **3** (Rf = 0.58), a 78.3% yield. ^{1}H NMR (400 MHz, $CDCl_3$) δ=5.61 (dtd, *J* = 15.6, 10.5, 7.3 Hz, 2H), 3.66 (s, 2H), 3.51 (ddd, *J* = 9.4, 5.5, 3.8 Hz, 1H), 3.47 – 3.41 (m, 1H), 3.40 – 3.31 (m, 1H), 2.39 (s, 1H), 2.38 – 2.26 (m, 1H), 2.06 (m, 3H), 1.98 – 1.88 (m, 1H), 1.85 – 1.62 (m, 3H), 1.53 – 1.43 (m, 1H), 1.43 – 1.32 (m, 1H) ppm; ^{13}C NMR (100 MHz, $CDCl_3$) δ=22.5, 25.5, 25.7, 33.3, 34.0, 61.9, 69.3, 80.9, 129.4, 129.9 ppm.

(*E*)-2-(Cyclooct-4-enyloxy)ethanol (4). (*Z*)-2-(Cyclooct-4-enyloxy)ethanol (1.0 g, 5.9 mmol) was converted to the (*E*)-isomers following a previously described cycle/trap method[4] with the exception of using methyl 4-(trifluoromethyl)benzoate (1.1 g, 7.9 mmol) as the photochemical sensitizer. The (*E*)-isomers were released from the 10% $AgNO_3$ silica gel with 50 mL of 30% ammonium $hydroxide_{(aq)}$ and 50 mL DCM by stirring for 10 min. The suspension was filtered, the organics separated, dried ($MgSO_4$) and concentrated to give 500 mg of a pale yellow oil. This crude mixture was subjected to column chromatography (2:1 pentane:Et_2O; starting material Rf = 0.23) securing 106 mg of the minor isomer (Rf = 0.31)and 262 mg of the major isomer (Rf = 0.14).
Spectroscopic properties of the major diastereomer: ^{1}H NMR (400 MHz, $CDCl_3$) δ=5.62 – 5.53 (m, 1H), 5.43 – 5.33 (m, 1H), 3.68 (dd, *J* = 10.3, 5.3 Hz, 2H), 3.52 – 3.45 (m, 1H), 3.39 (dt, *J* = 9.6, 4.7 Hz, 1H), 3.03 (dd, *J* = 10.7, 4.2 Hz, 1H), 2.37 (m, 2H), 2.24 (ddd, *J* = 23.6, 11.7, 5.1 Hz, 1H), 2.15 – 2.05 (m, 1H), 2.03 – 1.91 (m, 3H), 1.88 – 1.77 (m, 2H), 1.51 (dd, *J* = 16.5, 6.4 Hz, 2H) ppm;
Spectroscopic properties of the minor diastereomer: ^{1}H NMR (400 MHz, $CDCl_3$) δ=5.62 – 5.43 (m, 2H), 3.74 (dd, *J* = 10.1, 5.4 Hz, 2H), 3.62 (dd, *J* = 10.1, 4.7 Hz, 1H), 3.55 (dt, *J* = 9.3, 4.6 Hz, 1H), 3.47 – 3.40 (m, 1H), 2.36 – 2.12 (m, 4H), 2.04 (dd, *J* = 12.9, 6.8 Hz, 2H), 1.80 (ddd, *J* = 17.5, 11.1, 3.4 Hz, 3H), 1.50 (td, *J* = 14.1, 4.7 Hz, 1H), 1.19 (dd, *J* = 18.1, 10.9 Hz, 1H) ppm; ^{13}C NMR (100 MHz, $CDCl_3$) δ=27.6, 29.8, 32.9, 34.4, 40.1, 62.1, 69.6, 74.9, 131.3, 135.8 ppm.

(*E*)-2-(Cyclooct-4-enyloxy)ethyl 4-methylbenzenesulfonate (5). The major isomer of **(***E*)-2-(cyclooct-4-enyloxy)ethanol (180 mg, 1.1 mmol), tosyl chloride (262 mg, 1.4 mmol), and triethylamine (214 mg, 2.1 mmol) were combined in acetonitrile (6 mL). Reaction progress was monitored by TLC (1:1 hexanes:EA; starting material Rf = 0.50 and desired product Rf = 0.84). After 2 h stirring at room temperature, the reaction mixture was filtered and concentrated by rotary evaporatoation. The crude mixture was subjected to column chromatography (1:1 hexanes:ethyl acetate) to give 298 mg of (*E*)-2-(cyclooct-4-enyloxy)ethyl 4-methylbenzenesulfonate **5**, a 84% yield. ^{1}H NMR (400 MHz, $CDCl_3$) δ=7.79 (d, *J* = 8.3 Hz, 2H), 7.33 (d, *J* = 8.1 Hz, 2H), 5.59 – 5.48 (m, 1H), 5.39 – 5.26 (m, 1H), 4.11 (t, *J* = 5.0 Hz, 2H), 3.58 – 3.42 (m, 2H), 2.95 (dd, *J* = 10.5, 3.5 Hz, 1H), 2.45 (s, 3H), 2.35 (dd, *J* = 8.0, 4.9 Hz, 2H), 2.24 – 2.11 (m, 1H), 2.01 – 1.88 (m, 3H), 1.82 – 1.65 (m, 2H), 1.50 – 1.38 (m, 2H) ppm; ^{13}C NMR (100 MHz, $CDCl_3$) δ=21.6, 31.7, 32.9, 34.5, 37.6, 40.6, 65.6, 69.5, 86.3, 128.0, 129.7, 132.2, 133.3, 135.3, 144.7 ppm.

(*E*)-5-(2-Fluoroethoxy)cyclooct-1-ene (6^{19F}). (*E*)-2-(Cyclooct-4-enyloxy)ethyl 4-methylbenzenesulfonate (19 mg, 58.6 µmol) diluted in THF (1 mL) was treated with a tetrabutylammonium fluoride in THF (123 µL of 1 M solution). Reaction progress was monitored by TLC (2:1 pentane:Et_2O; starting material Rf = 0.62 and desired product Rf = 0.92) After stirring for 2 h, the mixture was concentrated and the resulting amber oil subjected to column chromatography (silica gel, pentane) isolating 9.2 mg of (*E*)-5-(2-fluoroethoxy)cyclooct-1-ene $\mathbf{6^{19F}}$ (91.1%) ^{1}H NMR (400 MHz, $CDCl_3$) δ=5.58 (ddd, *J* = 15.0, 11.2, 3.6 Hz, 1H), 5.38 (ddd, *J* =

15.7, 11.4, 3.5 Hz, 1H), 4.50 (dt, $J_{H\text{-}F}$ = 47.7 Hz, $J_{H\text{-}H}$ = 4.3 Hz, 1H), 3.68 – 3.46 (m, 2H), 3.05 (dd, *J* = 10.5, 4.7 Hz, 1H), 2.37 (t, *J* = 11.1 Hz, 2H), 2.24 (ddd, *J* = 23.5, 11.8, 5.2 Hz, 1H), 2.10 (dd, *J* = 13.0, 4.7 Hz, 1H), 2.03 – 1.78 (m, 4H), 1.58 – 1.46 (m, 2H) ppm; ^{13}C NMR (100 MHz, $CDCl_3$) δ=31.7, 33.0, 34.5, 37.7, 40.7, 67.2 (d, $J_{C\text{-}F}$ = 20 Hz), 83.3 (d, $J_{C\text{-}F}$ = 169 Hz), 86.2, 132.2, 135.4 ppm; ^{19}F NMR (376 MHz, $CDCl_3$) δ=-223.6 (m) ppm.

AZD2281-Tz (9). Cyclohexylcarbodiimide polystyrene resin (127 mg, 2.3 mmol/g) was added to a solution of 4-[[4-Fluoro-3-(4-(5-oxopentanamide) piperazine-1-carbonyl)phenyl]methyl]-2H-phthalazin-1-one **7** (70 mg, 0.15 mmol) in dichloromethane (10 mL) and the resulting mixture was stirred gently for 7 h at room temperature. Subsequently, tetrazine amine **8** (55 mg, 0.29 mmol) and triethylamine (81 µL, 0.58 mmol) was added and the mixture stirred for another 60 min, before the reaction mixture was filtered and volatiles removed in vacuo. The crude material was purified via HPLC, yielding the title compound as a pink solid (24 mg, 37 µmol, 25%). ^{1}H NMR (400 MHz, CD_3OD, * indicates rotamer peak) δ = 10.32 (s, 1H, C*H*), 10.30 (s, 1H, C*H**), 8.56-8.40 (m, 3H, $C_{arom}H$, N*H*), 8.37-8.34 (m, 1H, $C_{arom}H$), 7.96-7.94 (m, 1H, $C_{arom}H$), 7.89-7.82 (m, 2H, $C_{arom}H$), 7.59-7.53 (m, 2H, $C_{arom}H$), 7.50-7.47 (m, 1H, $C_{arom}H$), 7.39-7.35 (m, 1H, $C_{arom}H$), 7.15 (t, 1H, $^3J_{HH}$ = 9.0, $C_{arom}H$), 4.50-4.48 (m, 2H, CH_2), 4.39 (s, 2H, CH_2), 3.70-3.25 (m, 8H, CH_2), 2.46 (t, 2H, $^3J_{HH}$ = 7.5, CH_2), 2.41 (t, 2H, $^3J_{HH}$ = 7.5, *CH_2), 2.39-2.33 (m, 2H, $^3J_{HH}$ = 7.0, CH_2, *CH_2), 1.99-1.89 (m, 2H, CH_2, *CH_2) ppm; ^{19}F NMR (376 MHz, CD_3OD) δ = -121.22 ppm; LC-ESI-MS(-) *m*/*z* = 648.3 $[M\text{-}H^+]^-$; LC-ESI-MS(+) *m*/*z* = 650.4 $[M+H^+]^+$. HRMS-ESI $[M+H]^+$ m/z calcd. for $[C_{34}H_{32}FN_9O_4]^+$ 650.2634, found 650.2648.

1-AZD2281-^{19}F (10^{19F}). A solution of AZD2281-Tz **9** in DMSO (10 µL, 1 mM, 0.01 µmol) was added to **6**^{19F} (10 uL, 1 mM in DMSO, 0.01 µmol) and agitated for 30 min, before the crude reaction mixture was purified via HPLC-chromatography. HRMS-ESI $[M+H]^+$ m/z calcd. for $[C_{44}H_{47}F_2N_7O_5]^+$ 792.368, found 792.3690.

1-AZD2281-^{16}O (10^{16O}). A solution of AZD2281-Tz **9** in DMSO (10 µL, 1 mM, 0.01 µmol) was added to **4** (10 uL, 1 mM in DMSO, 0.01 µmol) and agitated for 30 min, before the crude reaction mixture was purified via HPLC-chromatography. HRMS-ESI $[M+H]^+$ m/z calcd. for $[C_{44}H_{48}FN_7O_6]^+$ 790.3723, found 790.3707.

1-AZD2281-^{18}O (10^{18O}). A solution of HPLC purified 1-AZD2281-^{18}F (**10**^{18F}) was allowed to stand at room temperature for 48 h to allow all radioactive ^{18}F to decay. HRMS-ESI $[M+H]^+$ m/z calcd. for $[C44H48FN7O5^{18}O]^+$ 792.3765, found 792.3753.

4-[[4-Fluoro-3-((6-hydroxyhexanoyl)piperazine-1-carbonyl)phenyl]methyl]-2H-phthalazin-1-one (12). 4-[[4-Fluoro-3-(piperazine-1-carbonyl)phenyl]methyl]-2H-phthalazin-1-one 11 (250 mg, 0.68 mmol), HBTU (337 mg, 0.89 mmol) and triethylamine (285 µL, 1.18 mmol) were added to a solution of 6-hydroxyhexanoic acid (180 mg, 1.36 mmol) in DMF (3.0 mL) and the reaction mixture was stirred at room temperature for 60 min, before dichloromethane (8 mL) and water (8mL) were added, the organic phase separated and washed with water (3x 8 mL). The organic phase was dried over $MgSO_4$, volatiles removed in vacuo and the resulting crude material purified via HPLC, yielding the title compound as a clear solid (55.6 mg, 0.12 mmol, 17%). NMR (400 MHz, CD_3OD, * indicates rotamer peak) δ = 8.39-8.35 (m, 2H, $C_{arom}H$, N*H*), 7.96-7.81 (m, 3H, $C_{arom}H$), 7.50-7.47 (m, 1H, $C_{arom}H$), 7.39-7.36 (m, 1H, $C_{arom}H$), 7.16 (t, 1H, $^3J_{HH}$ = 9.0, $C_{arom}H$), 4.38 (s, 2H, CH_2), 3.80-3.30 (m, 10H, CH_2), 2.47-2.36 (m, 2H, CH_2, CH_2*), 1.67-1.51 (m, 4H, CH_2, CH_2*), 1.45-1.35 (m, 2H, CH_2, CH_2*) ppm; ^{19}F NMR (376 MHz, CD_3OD) δ = -121.18 (m) ppm; LC-ESI-MS(-) *m*/*z* = 479.2. $[M\text{-}H^+]^-$; LC-ESI-MS(+) *m*/*z* = 481.5 $[M+H^+]^+$.

4-[[4-Fluoro-3-((6-tosylhexanoyl)piperazine-1-carbonyl)phenyl]methyl]-2H-phthalazin-1-one (13). Triethylamine (29 µL, 0.21 mmol) was added to a solution of *p*-toluenesulfonyl chloride (20 mg, 0.10 mmol) and 4-[[4-Fluoro-3-((6-hydroxyhexanoyl)piperazine-1-carbonyl) phenyl]methyl]-2H-phthalazin-1-one **12** (25 mg, 0.052 mmol) in dichloromethane (5 mL), the

reaction mixture was stirred at room temperature over night and purified via HPLC, yielding the title compound as a clear solid (7.8 mg, 0.01 mmol. 24 %). NMR (400 MHz, CD_3OD, * indicates rotamer peak) δ = 8.35 (d, 1H, $^3J_{HH}$ = 7.5, $C_{arom}H$), 7.95-7.93 (m, 1H, $C_{arom}H$), 7.88-7.74 (m, 4H, $C_{arom}H$), 7.50-7.36 (m, 4H, $C_{arom}H$), 7.16 (t, 1H, $^3J_{HH}$ = 9.0, $C_{arom}H$), 4.38 (s, 2H, CH_2), 4.03 (t, 2H, $^3J_{HH}$ = 6.0, CH_2), 4.01 (t, 2H, $^3J_{HH}$ = 6.0, CH_2*), 3.78-3.28 (m, 8H, CH_2), 2.44-2.31 (m, 5H, CH_3, CH_3*, CH_2, CH_2*), 1.69-1.49 (m, 4H, CH_2, CH_2*), 1.40-1.31 (m, 2H, CH_2, CH_2*) ppm; ^{19}F NMR (376 MHz, CD_3OD) δ = -121.14 (m) ppm; LC-ESI-MS(-) *m*/*z* = 633.3 $[M\text{-}H^+]^-$; LC-ESI-MS (+) *m*/*z* = 635.4 $[M+H^+]^+$.

4-[[4-Fluoro-3-((2-hydroxyacetyl)piperazine-1-carbonyl)phenyl]methyl]-2H-phthalazin-1-one (15). 4-[[4-Fluoro-3-(piperazine-1-carbonyl)phenyl]methyl]-2H-phthalazin-1-one **11** (86 mg, 0.24 mmol), HBTU (116 mg, 0.30 mmol) and triethylamine (164 µL, 1.18 mmol) were added to a solution of 2-hydroxyacetic acid (36 mg, 0.48 mmol) in DMF (1.5 mL) and the reaction mixture was stirred at room temperature for 40 min, before dichloromethane (4 mL) and water (4 mL) were added, the organic phase separated and washed with NaOH (0.2 M, 3x 4 mL) and water (3x 4 mL). The organic phase was dried over $MgSO_4$, volatiles were removed in vacuo and the resulting crude material was purified via HPLC, yielding the title compound as a clear solid (24.3 mg, 0.06 µmol, 50%). NMR (400 MHz, CD_3OD, * indicates rotamer peak) δ = 8.37 (d, 1H, $^3J_{HH}$ = 7.8, $C_{arom}H$), 8.16 (s, 1H, N*H*), 7.91-7.78 (m, 2H, $C_{arom}H$), 7.54-7.44 (m, 1H, $C_{arom}H$), 7.39-7.37 (m, 1H, $C_{arom}H$), 7.16 (t, 1H, $^3J_{HH}$ = 9.0, $C_{arom}H$), 4.38 (s, 2H, CH_2), 4.28 (s, 2H, CH_2), 4.21 (s, 2H, CH_2*), 3.78-3.30 (m, 8H, CH_2); ^{19}F NMR (376 MHz, CD_3OD) δ = -121.21 (m); LC-ESI-MS(-) *m*/*z* = 423.2 $[M\text{-}H^+]^-$; LC-ESI-MS(+) *m*/*z* = 425.3 $[M+H^+]^+$.

4-[[4-Fluoro-3-((2-tosyl-acetyl)piperazine-1-carbonyl)phenyl]methyl]-2H-phthalazin-1-one (16). Triethylamine (53 µL, 0.38 mmol) was added to a solution of *p*-toluenesulfonyl chloride (36 mg, 0.19 mmol) and 4-[[4-Fluoro-3-((2-hydroxyacetic acid)piperazine-1-carbonyl)phenyl] methyl]-2H-phthalazin-1-one **15** (40 mg, 0.094 mmol) in dichloromethane (5 mL), the reaction mixture was stirred at room temperature over night and purified via HPLC, yielding the title compound as a clear solid (34 mg, 0.06 mmol. 32 %). NMR (400 MHz, CD_3OD, * indicates rotamer peak) δ = 8.37 (d, 1H, $^3J_{HH}$ = 7.5, $C_{arom}H$), 7.96-7.82 (m, 5H, $C_{arom}H$), 7.49-7.43 (m, 3H, $C_{arom}H$), 7.38-7.36 (m, 1H, $C_{arom}H$), 7.16 (t, 1H, $^3J_{HH}$ = 9.0, $C_{arom}H$), 4.85 (s, 2H, CH_2), 4.78 (s, 2H, CH_2*), 4.38 (s, 2H, CH_2), 3.75-3.25 (m, 8H, CH_2), 2.45 (s, 3H, CH_3); ^{19}F NMR (376 MHz, CD_3OD) δ = -121.16 (m); LC-ESI-MS(-) *m*/*z* = 577.1 $[M\text{-}H^+]^-$; LC-ESI-MS(+) *m*/*z* = 579.3 $[M+H^+]^+$.

2-AZD2281-19F (17^{19F}). Freshly dried NaF (8.4 mg, 0.2 mmol) was added to a solution of 4-[[4-fluoro-3-((2-tosyl-acetyl)piperazine-1-carbonyl)phenyl]methyl]-2H-phthalazin-1-one **16** (10 mg, 0.02 mmol) in dry acetonitrile (2 mL) and was stirred for 6 h at 40°C before the reaction mixture was purified via HPLC, yielding the title compound as a clear solid (1.2 mg, 2.8 µmol, 16%). NMR (400 MHz, CD_3OD, * indicates rotamer peak) δ = 8.38-8.31 (m, 2H, $C_{arom}H$, N*H*), 7.97-7.82 (m, 3H, $C_{arom}H$), 7.51-7.47 (m, 1H, $C_{arom}H$), 7.39-7.37 (m, 1H, $C_{arom}H$), 7.17 (t, 1H, $^3J_{HH}$ = 9.0, $C_{arom}H$), 5.16 (d, 2H, $^3J_{HH}$ = 46.7, CH_2), 5.09 (s, 2H, $^3J_{HH}$ = 46.7, CH_2*), 4.39 (s, 2H, CH_2), 3.79-3.30 (m, 8H, CH_2); ^{19}F NMR (376 MHz, CD_3OD, * indicates rotamer peak) δ = -121.20 (m), -231.06 (t, $^3J_{HF}$ = 46.6 Hz, CH_2F*), -231.24 (t, $^3J_{HF}$ = 46.6 Hz, CH_2F*); LC-ESI-MS (-) *m*/*z* = 425.2 $[M\text{-}H^+]^-$; LC-ESI-MS(+) *m*/*z* = 427.3 $[M+H^+]^+$.

Radiochemistry.

4-(4-fluoro-3-(4-(2-18F-fluoroacetyl)piperazine-1-carbonyl)benzyl)phthalazin-1(2*H*)-one (17^{18F}) $[^{18}F]$-F^-, n.c.a., (~77 MBq, 2.4 ± 0.9 mCi) in $H_2{}^{18}O$ (~150 µL), 250 µL of a 75 mM tetrabutylammonium bicarbonate ($^nBu_4NHCO_3$) solution in water, and 750 µL of MeCN were combined in a 10-mL test tube and heated (microwave) to 98 °C under a stream of argon. At 4, 8 and 12 min 1 mL of MeCN was added and evaporated off. To the dried $[^{18}F]$-F^- (n.c.a.)/ $^nBu_4NHCO_3$ was added 100 µL of of a 35 mM solution of tosylate **16** in dimethylformamide and

heated to 40 °C for 10 min. To remove unreacted [^{18}F]-fluoride, this mixture was filtered through an Alumina-N cartridge (100 mg, 1 mL, Waters) to give 16 µCi in the filtrate. HPLC coinjection of a sample of **17^{19F}** with an aliquot of this filtrate demonstrated formation of the desired product **17^{18F}** in 30 min and 0.8% dcRCY.

2-18F-(*E*)-5-(2-Fluoroethoxy)cyclooct-1-ene (6^{18F}). 2-18F-(*E*)-5-(2-Fluoroethoxy)cyclooct-1-ene (^{18}F-TCO) was prepared using Synthra RN Plus automated synthesizer (Synthra GmbH, Hamburg, Germany) operated by SynthraView software in an average time of 40 min. The target well was charged with [^{18}F]-F^-, n.c.a., (~1110 MBq, 30 ± 10 mCi) in $H_2{}^{18}O$ (150 µL), 250 µL of a 75 mM tetrabutylammonium bicarbonate (TBAB) solution in water, and 200 µL of MeCN. The synthesizer reagent vials were filled as follows: A2 with MeCN (350 µL), A3 with tosylate **5** (4.0 mg, 12.3 µmol) in DMSO (400 µL), A5 with DMSO (50 µL), and B2 with H_2O (800 µL). The [^{18}F]-F^-/TBAB solution was transferred to Reaction Vessel #1 and dried by azeotropic distillation of the acetonitrile/water solution by heating to 60 °C under reduced pressure and a flow of argon to achieve ~310 mbar for 2 min followed by 98 °C and 270 mbar for 4 min. Reaction Vessel #1 was cooled to 50 °C, tosylate **5** in DMSO (400 µL) added, the reaction vessel pressurized to 2000 mbar, and heated to 90 °C for 10 min. Cooled to 30 °C, the mixture was filtered through an Alumina-N cartridge (100 mg, 1 mL, Waters) into Reaction Vessel #2. The Alumina-N cartridge was washed with DMSO (50 µL) and the combined filtrates were diluted with water (800 µL). This solution was subjected to preparative HPLC purification . **6^{18F}** was collected (t_R = 10.1 min) in 4-5 mL of solvent, isolated by C18 solid phase extraction and eluted with DCM (600 µL) to give 7.7 ± 3.4 mCi of **6^{18F}** in 44.7 ± 7.8% (n = 16) decay-corrected radiochemical yield (dcRCY) in an average time of 41 min from the end of drying of [^{18}F]-F^- (n.c.a.). Analytical HPLC demonstrated >93% radiochemical purity of **6^{18F}**.

1-AZD2281-^{18}F (10^{18F}). To the above described **6^{18F}**/DCM solution was added AZD2281-Tz **9** (7 µL of 18.5 mM DMSO solution, 0.13 µmol) and stirred at rt for 3 min. The mixture was concentrated with a gentle stream of argon, reconstituted in 1:1 MeCN/H_2O (to a volume of 1.3 mL), subjected to preparative HPLC purification (t_R = 6.0 min) and isolated by C18 solid phase extraction. Elution with MeOH (600 uL) followed by evaporation of solvent provided 2.3 ± 0.8 mCi (n = 3) of **10^{18F}**.

1-AZD2281-^{18}O (10^{18O}). A solution of HPLC purified 1-AZD2281-^{18}F (**10^{18F}**) was allowed to stand at room temperature for 48 h to allow all radioactivity to decay. HRMS-ESI $[M+H]^+$ m/z calcd. for $[C44H48FN7O5{}^{18}O]^+$ 792.3765, found 792.3753.

Appendix B

NMR spectra of compounds in Chapter 3

Spectra ^{1}H and ^{13}C of compound **3.2**

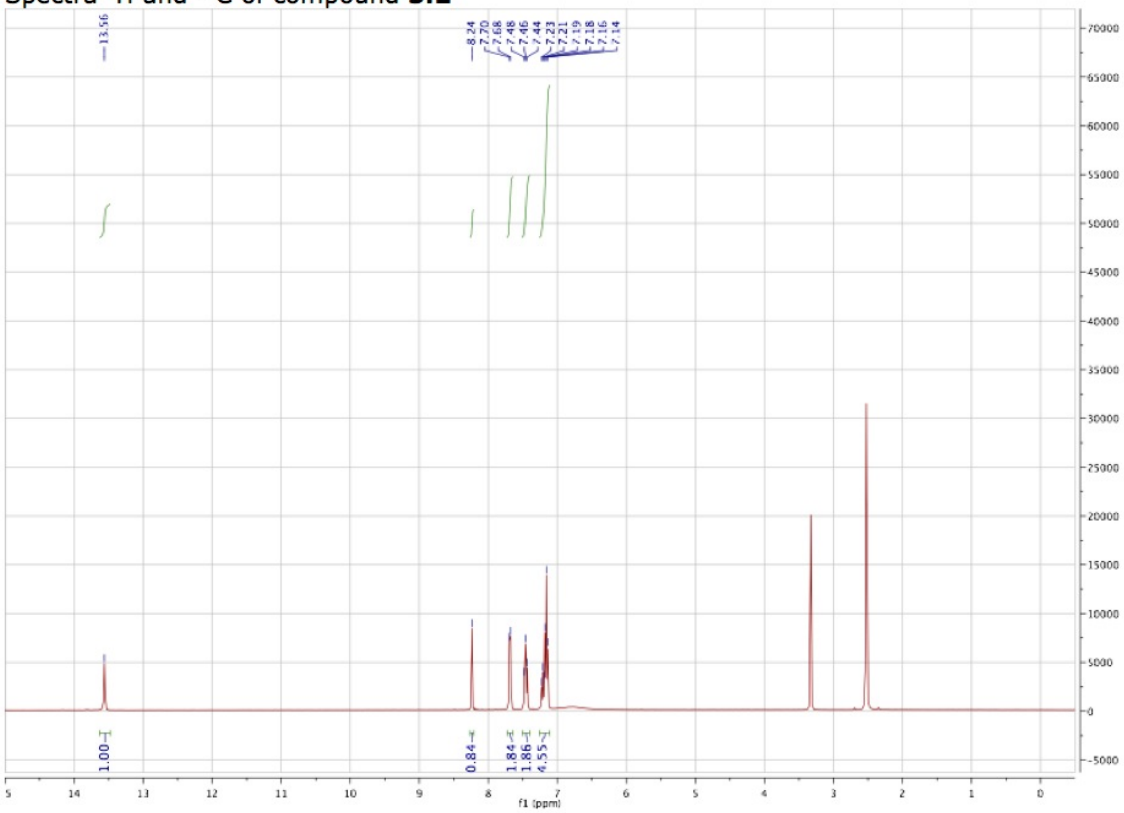

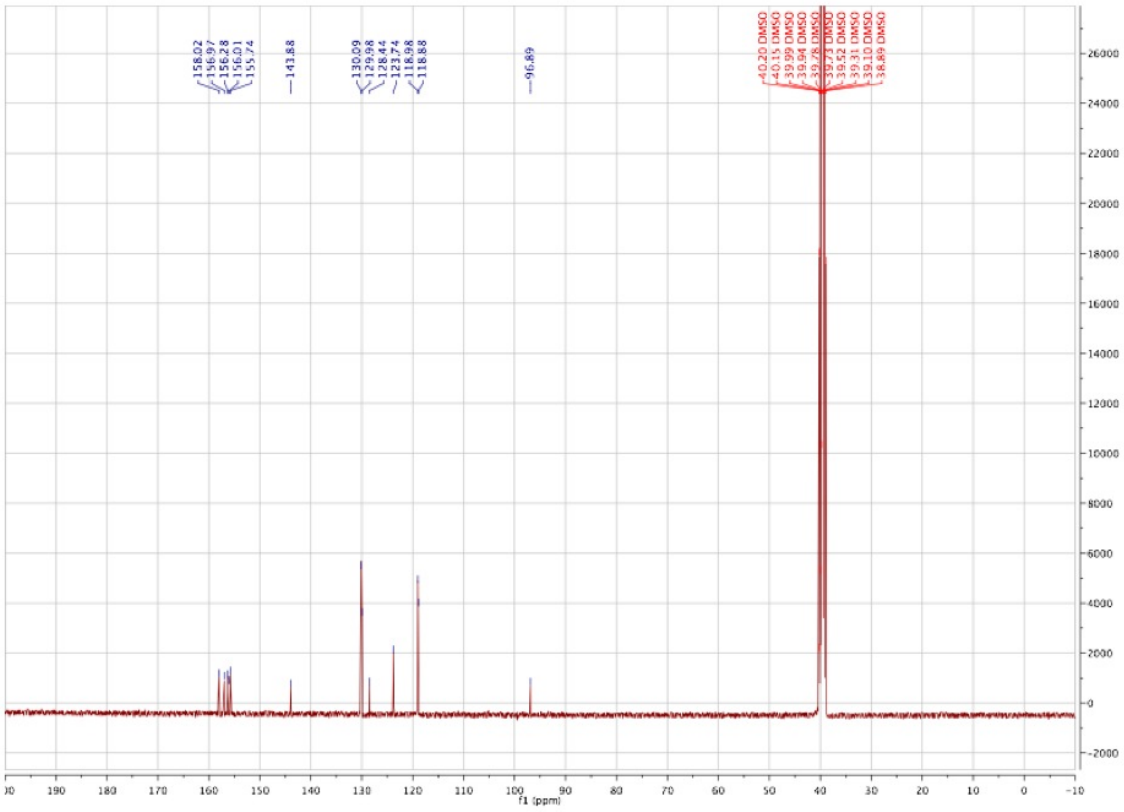

Spectra ^{1}H and ^{13}C of compound **3.3**

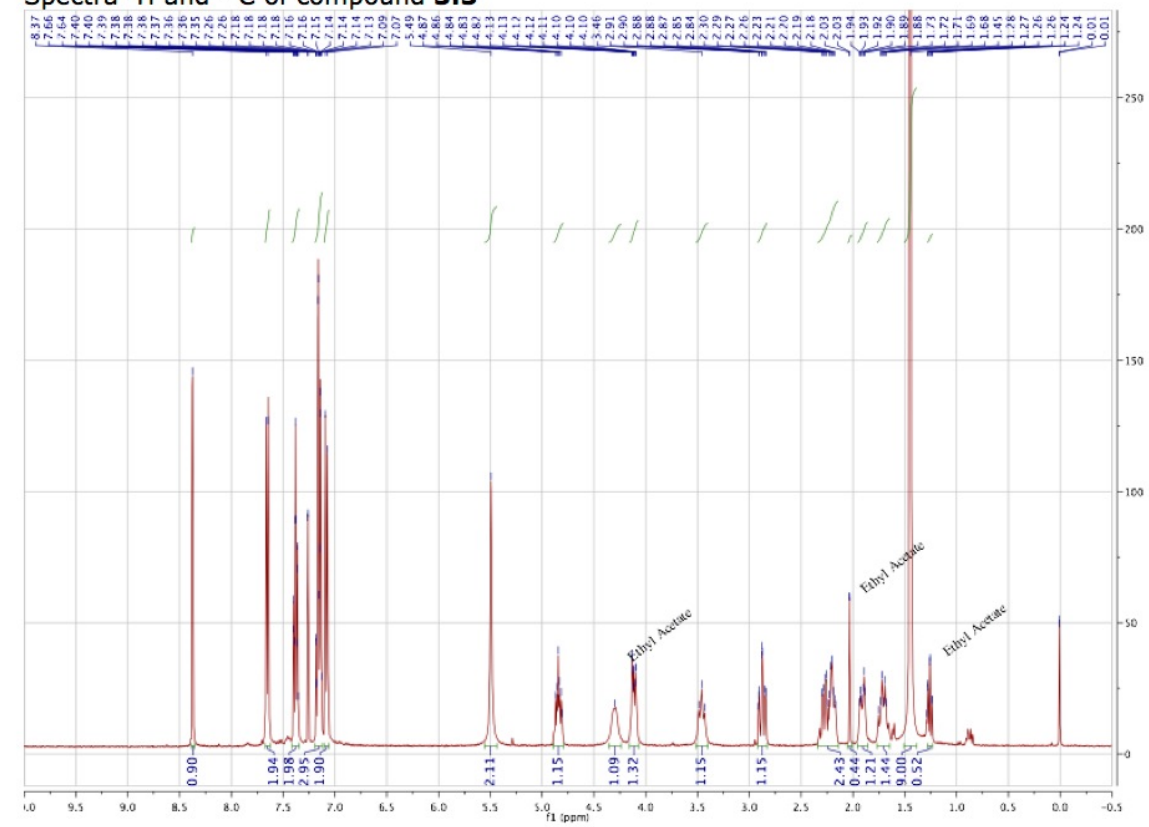

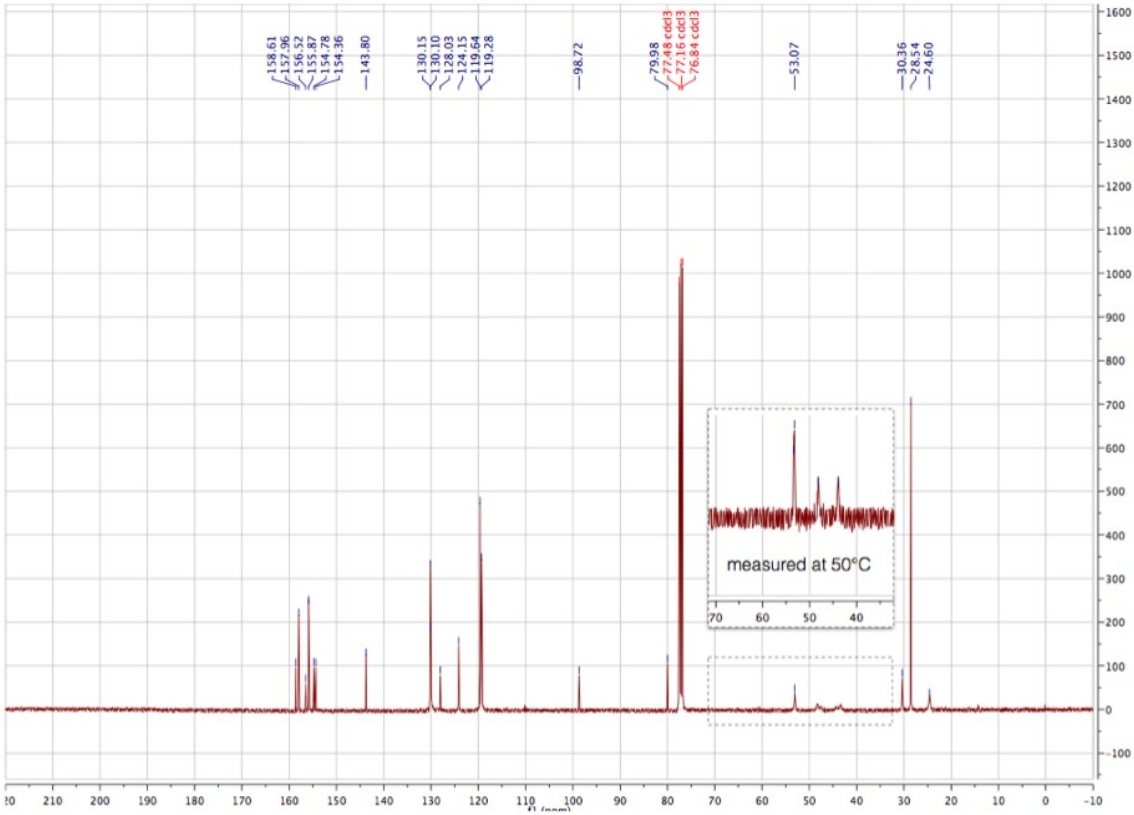

Spectra ^{1}H and ^{13}C of compound **3.4**

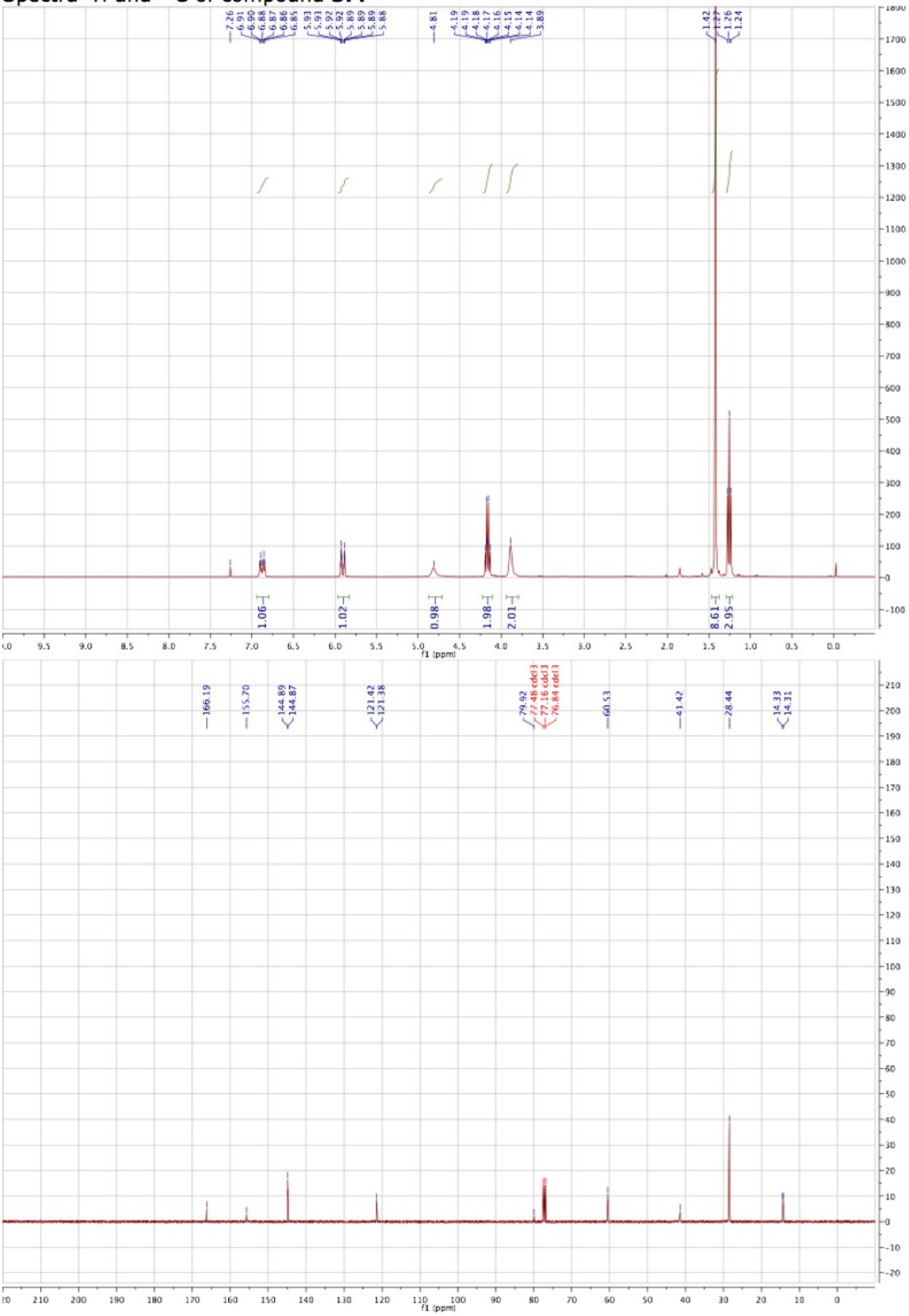

Spectra ^{1}H and ^{13}C of compound **3.5**

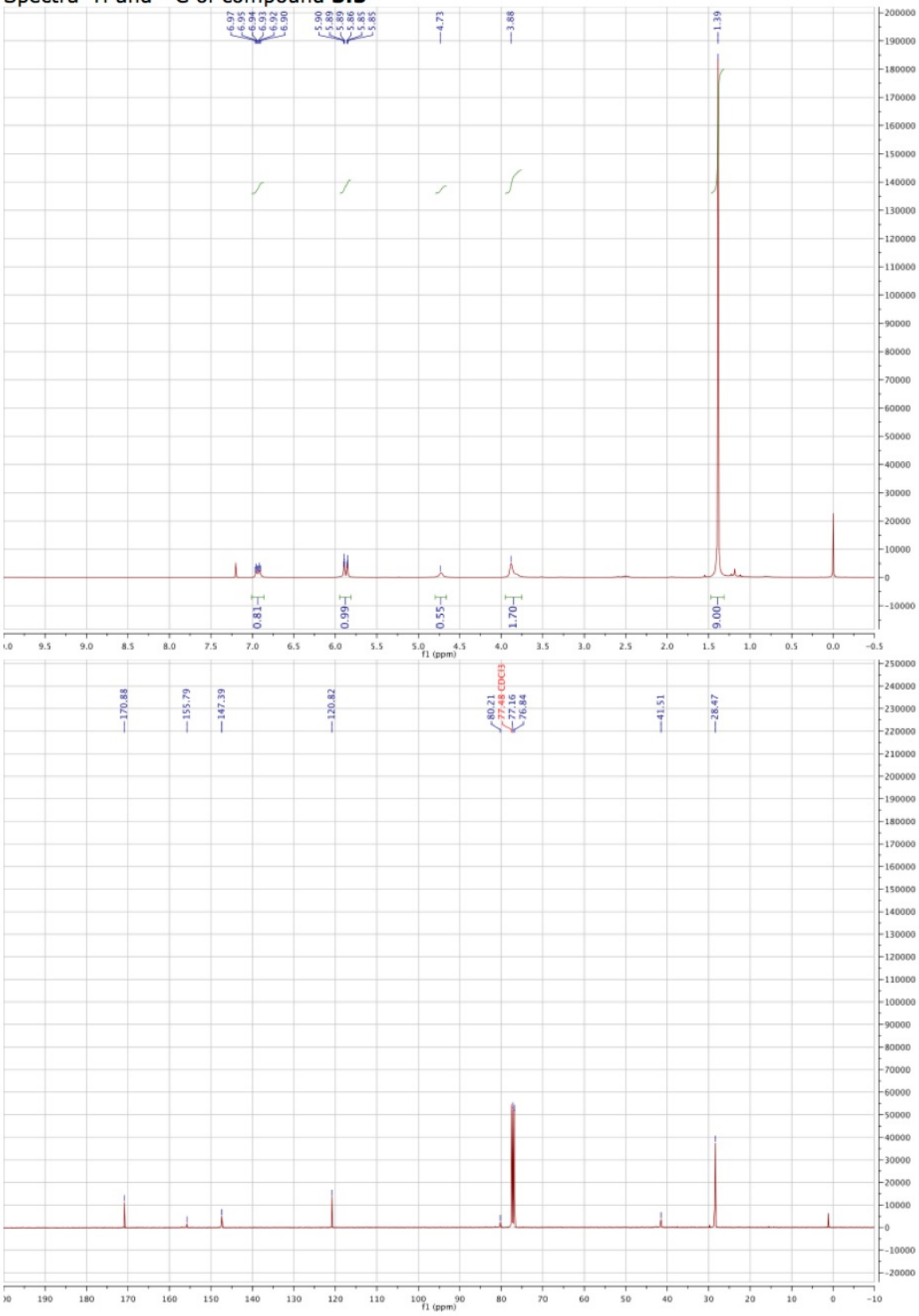

Spectra ^{1}H of compound **3.6**

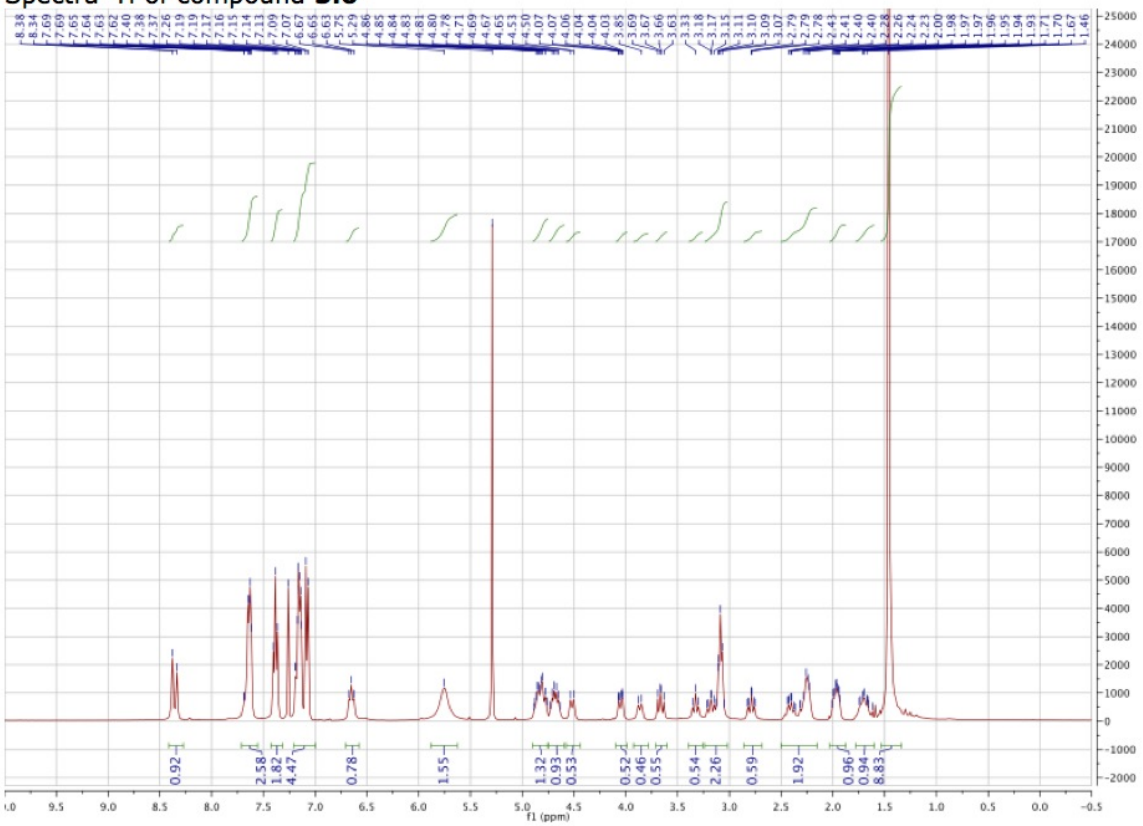

Spectra ^{1}H of compound **3.7**

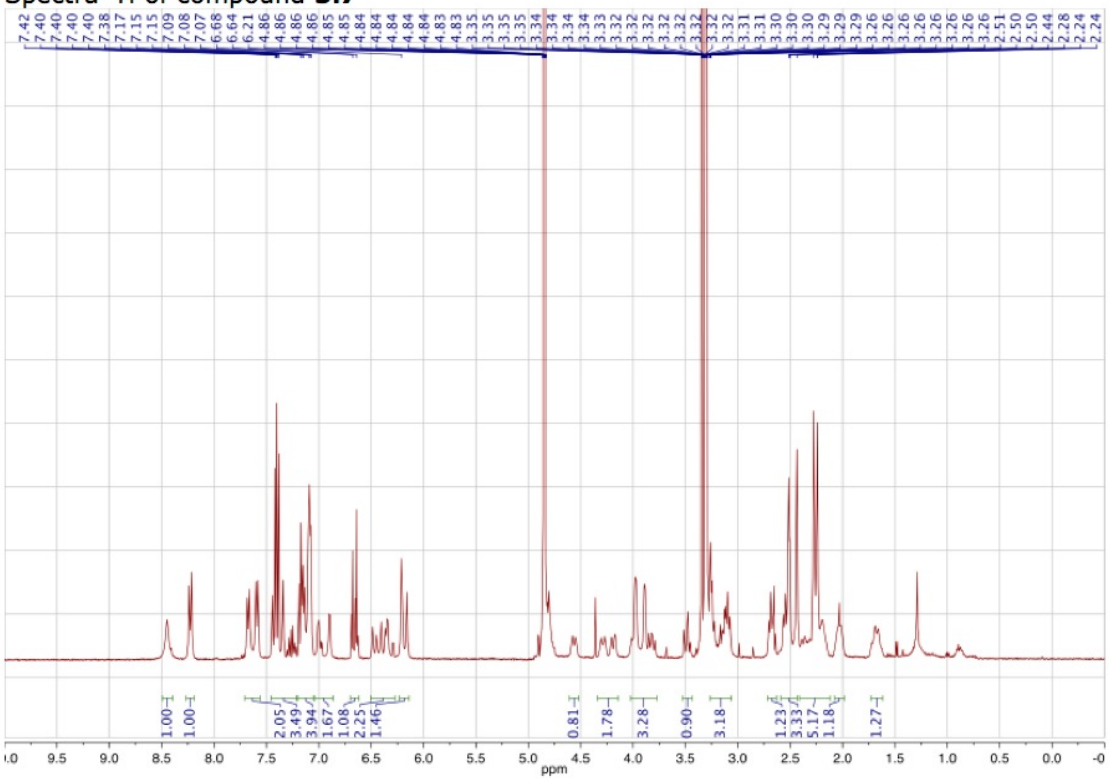

Appendix C

Images of paper-based device in Chapter 5

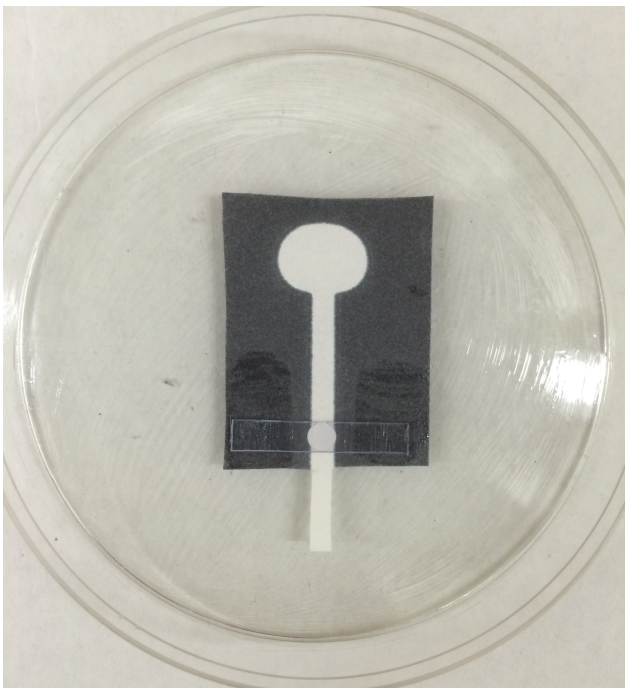

Front

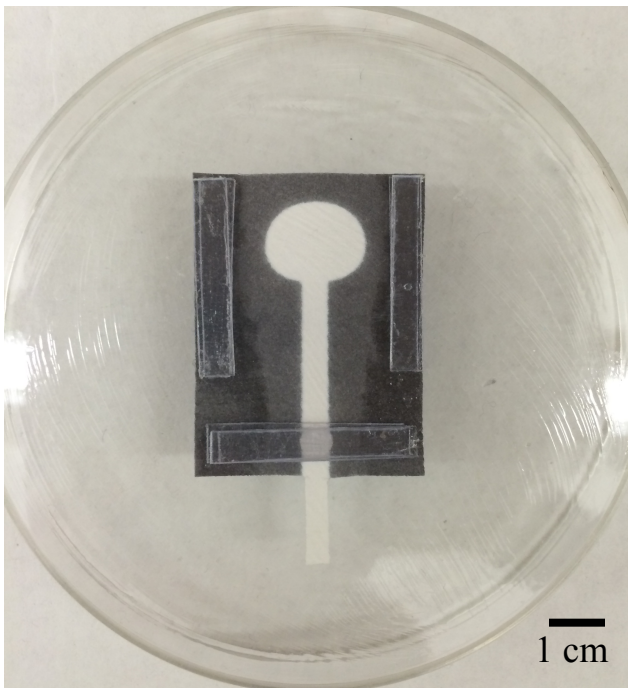

Back